Robust Human Motion Tracking using Low-Cost Inertial Sensors

by

Yatiraj K Shetty

A Thesis Presented in Partial Fulfillment
of the Requirements for the Degree
Master of Science

Approved November 2016 by the
Graduate Supervisory Committee:

Sangram Redkar, Chair
Thomas Sugar
Spring Berman
Hyunglae Lee

ARIZONA STATE UNIVERSITY

December 2016

ABSTRACT

The advancements in the technology of MEMS fabrication has been phenomenal in recent years. In no mean measure this has been the result of continued demand from the consumer electronics market to make devices smaller and better. MEMS inertial measuring units (IMUs) have found revolutionary applications in a wide array of fields like medical instrumentation, navigation, attitude stabilization and virtual reality. It has to be noted though that for advanced applications of motion tracking, navigation and guidance the cost of the IMUs is still pretty high. This is mainly because the process of calibration and signal processing used to get highly stable results from MEMS IMU is an expensive and time-consuming process. Also to be noted is the inevitability of using external sensors like GPS or camera for aiding the IMU data due to the error propagation in IMU measurements adds to the complexity of the system.

First an efficient technique is proposed to acquire clean and stable data from unaided IMU measurements and then proceed to use that system for tracking human motion. First part of this report details the design and development of the low-cost inertial measuring system 'yIMU'. This thesis intends to bring together seemingly independent techniques that were highly application specific into one monolithic algorithm that is computationally efficient for generating reliable orientation estimates. Second part, systematically deals with development of a tracking routine for human limb movements. The validity of the system has then been verified.

The central idea is that in most cases the use of expensive MEMS IMUs is not warranted if robust smart algorithms can be deployed to gather data at a fraction of the cost. A low-

cost prototype has been developed comparable to tactical grade performance for under $15 hardware. In order to further the practicability of this device we have applied it to human motion tracking with excellent results. The commerciality of device has hence been thoroughly established.

To my mother: Geeta

And

father: Krishnaraj Shetty

ACKNOWLEDGMENTS

All this would have been inconceivable without the support of my parents and my brother, I thank them for being with me always and financially supporting me throughout my studies.

I appreciate the help I got from Osama and Eddy for hardware design, and Yuchong for his rate table. I also thank Prof. Kannan for giving me access to his thermal chamber and Pavan for helping me set up the experiment.

I thank Prof. Redkar for giving me this opportunity to work on such a wonderful project. Working with him gave me inspiration and insight to look at engineering problems critically, and confidence to work on any subject. I also thank him for the futon :)

TABLE OF CONTENTS

		Page
LIST OF TABLES ……..		vii
LIST OF FIGURES ……		viii
CHAPTER		
1 INTRODUCTION …….		1
1.1	Inertial Measurement Unit …….	2
1.1.1	Operational Principle……...	3
1.1.2	Grades of IMUs……...	5
1.1.3	Inertial Navigation System……..	7
1.1.4	System Applications ……...	9
1.2	Human Motion Tracking using Inertial Sensors …….	10
1.2.1	Rehabilitation Studies …….	10
1.2.2	Gait Augmentation……..	11
1.2.3	Motion Capture……	13
1.2.4	Summary…….	14
1.3	Previous Work…….……	16
1.3.1	Addressing the Limitations…….	19
1.4	Objectives and Methodology……..	20
1.5	Outline…….	20
2 DEVELOPMENT OF LOW-COST INERTIAL MEASUREMENT UNIT: yIMU……..		22

CHAPTER Page

2.1 Error Modelling and Calibration……. 24

2.1.1 Types of Errors……... 24

2.1.2 Temperature Compensation ……... 29

2.1.3 Static Bias Compensation…….. 32

2.1.4 Allan Variance Analysis…… 34

2.1.5 Power Spectral Density Analysis…… 36

2.1.6 Probability Density Function…….. 37

2.1.7 Drifting Bias Analysis…… 38

2.1.8 Simplified Error Model…….. 42

2.2 Dual IMU System…… 43

2.2.1 Dual IMUs…….. 43

2.2.2 Common Mode Effect……. 45

2.3 Sensor Fusion ……. 32

2.3.1 Representing Angles…… 48

2.3.2 Complementary Filter…….. 53

2.3.3 Sensor Fusion Scheme……. 54

2.4 Hardware Design……. 58

2.4.1 System Design……. 59

2.4.2 Enclosure Design……. 61

2.5 Performance Evaluation…….. 63

2.5.1 Testing Validity of Common Mode Effect…….. 63

2.5.2 AV Results…….. 72

CHAPTER Page

2.5.3 PSD Results……. 76

2.5.4 PDF Results……. 78

2.5.5 Drifting Bias Analysis Results…… 81

2.5.6 Orientation Tracking Performance…….. 84

3 JOINT ANGLE TRACKING USING INERTIAL SENSORS……. 89

3.1 Joint Angle Tracking …….. 89

3.1.1 Kinematic Modelling of Upper Limb…….. 89

3.1.2 Sensor-Segment Calibration…… 98

3.1.3 System Design……. 99

3.2 Performance Evaluation…….. 100

3.2.1 Experiment…….. 100

3.2.2 Results and Discussion…… 103

4 CONCLUSION…….. 104

4.1 Contributions…….. 104

4.2 Future Work…… 106

REFERENCES…… 109

APPENDIX

A MATHEMATICAL RESULTS…….. 114

B STATIC TEST PLOTS……... 122

LIST OF TABLES

Table		Page
2.1	Hardware Specification Of yIMU v1.4……	59
2.2	The Results of Linear Best Fit Between Sensor Output and Temperature for Mpu6050 in Opposing Configuration……...	66
2.3	Accelerometer Bias Error…….	71
2.4	Gyro Bias Error…….....	72
2.5	Comparing the Results of Av Analysis Between IMU-1 and yIMU Accelerometers…….	74
2.6	Comparing The Results Of AV Analysis Between IMU-1 And yIMU Accelerometers…….	75
2.7	PSD Slope Values For IMU-1…….	77
2.8	PSD Slope Values For yIMU. …….	78
2.9	IMU-1 Measurement Noise Variances……	80
2.10	yIMU Measurement Noise Variances…….	81
2.11	Markov Parameters For Single IMU-1……	82
2.12	Markov Parameters For yIMU And Comparison To yIMU……	83
3.1	DH Parameters For Upper Limb……..	94

LIST OF FIGURES

Figure		Page
1.1	A Circuit Board Of An IMU Containing MEMS Component……	3
1.2	Schematic Of An Inertial Measurement Unit……..	3
1.3	Principle of Operation of MEMS Inertial Sensors……..	4
1.4	Inertial Sensor Grades…….	7
1.5	MPU6050 Breakout Board……..	8
1.6	(A) Gimbaled Inertial Measuring Unit (B) Strapdown Inertial Measuring Unit ……	9
1.7	Strapdown Inertial Navigation Computing Tasks ……...	11
1.8	Devices Designed to Augment Human Running Developed at Human Machine Integration Lab, ASU …….....	12
1.9	eLegs Developed At Berkeley Robotics And Human Engineering Lab……	13
1.10	Rendering For An Inertial Mocap By Perception Neuron……..	25
2.1	Static Bias Error……..	26
2.2	(Left) Scale Factor Error; (Right) Misalignment Error……	31
2.3	Temperature Compensation…….	32
2.4	The Bias Compensated Angular Yaw Rate for the IMUs (Z Axis)…….	33
2.5	The Bias Compensated Angular Roll Rate for the Imus (X Axis)……..	34
2.6	The Bias Compensated Accelerometer Readings for the IMUs (X Axis)…….	35

Figure		Page
2.7	Sample Allan Deviation Plot For An Accelerometer……..	36
2.8	PSD For A Sample Accelerometer……..	37
2.9	Visual Representation Of Gaussian Distribution…….	38
2.10	Random Walk For A Sample MPU6050 Gyroscope……..	39
2.11	A Virtual IMU Observation Fusion Architecture……	44
2.12	Dual Axes Configuration…….	45
2.13	Gyroscope Output Comparison for Two IMUs with Opposed Sense Axes…….	46
2.14	Gyroscope Drift for Two Imus with Opposed Sense Axes…….	47
2.15	Euler Angle Representation…….	49
2.16	Measuring Tilt Using Accelerometers…….	50
2.17	Measuring Angles Using Gyroscopes……..	51
2.18	Euler To Quaternion Conversion…….....	52
2.19	Complementary Filter Structure…….....	54
2.20	The Stacked Boards In yIMU v1.4…….....	60
2.21	The Sense Axes Of The Dual IMU System…….	61
2.22	Enclosure For yIMU v1.4 With Straps……	62
2.23	Heraeus UT12p Thermal Chamber…….....	64
2.24	Temperature Profile Of The Experiment…….	65
2.25	Sample Scatter Plot Of Acc Axis X For IMU1……	65
2.26	Sample Scatter Plot Of Gyro Axis X For IMU2……..	66

Figure Page

2.27 Comparison of Temperature Effect Trends For Gyro X of IMU1, IMU2 And Combined Output …… 67

2.28 The FMC Shaker Used For Vibration Testing……. 68

2.29 Effect Of Vibration On IMU1 Accelerometers…… 69

2.30 Effect Of Vibration On IMU1 Gyroscopes…….. 69

2.31 Effect Of Vibration On Vibration Axis (Z axis)…….. 70

2.32 Effect of Vibration On Cross Axis (X axis)……. 71

2.34 Allan Deviation Plot For IMU-1 Accelerometer X……. 73

2.35 Allan Deviation Plot For yIMU Accelerometer X…….. 74

2.36 Allan Deviation Plot For IMU-1 Gyroscope X…… 74

2.37 Allan Deviation Plot For yIMU Gyroscope X……. 75

2.38 PSDs for IMU-1: (above) accelerometer (below) gyroscope for X axis. 77

2.39 PSDs for yIMU: (Above) Accelerometer (below) Gyroscope For X Axis……. 78

2.40 IMU-1 Measurement Noise Histogram with Gaussian Pdf Plotted over It (above) Accelerometer X (below) Gyroscope……. 79

2.41 yIMU Measurement Noise Histogram With Gaussian PDF Plotted Over It (Above) Accelerometer X (Below) Gyroscope X…….. 80

2.42 Random Walk In IMU-1 GyroX……..... 82

2.43 Random Wwalk In yIMU GyroX…… 83

2.44 Tracking Testing Apparatus……..... 84

2.45 Angle Vs Time……..... 85

Figure		Page
2.46	Rate Table Experiment about Yaw Axis- Constant Speed……..	86
2.47	Rate Table Experiment about Yaw Axis- Varying Speed ……..	86
2.48	Static Stability of yIMU- Gyroscopes Tested for 1 Hour ……...	87
2.49	Static Stability of Mpu6050 with Dmp Algorithm Tested for 20 Minutes……	87
2.50	Raw Gyro Output From MPU6050 For 20 Minutes……	88
3.1	Movements In Human Joints…….....	89
3.2	Categories Of Joint Movements…….....	91
3.3	Visualizing Human Body As Series Of Kinematic Segments…….	92
3.4	Kinematic Modelling Of Human Upper Limb…….	94
3.5	Forward Kinematics- Frames Of Reference……	95
3.6	Sensor-Segment Calibration…….	99
3.7	Tracking System Design…….	99
3.8	yIMU Placement On Subject Body…….	101
3.9	Graph Comparing the Elbow Flexion Angle Calculated Using the Noraxon IMUs with YIMU …….	101
3.10	Graph comparing the shoulder rotation calculated using the Noraxon IMUs with yIMU……..	102
3.11	Graph comparing the elbow flexion angle calculated using the Noraxon IMUs with yIMU……...	102
3.12	Graph comparing the knee flexion angle calculated using the Noraxon IMUs with yIMU……...	102

Chapter 1

INTRODUCTION

The main driver for increase in research activity in the field of inertial sensors applied to human motion analysis in recent years is due to the increase in the quality of micro-electro-mechanical systems (MEMS) technology. Being portable and cheap, MEMS based sensors are finding extensive usage in tracking the position and orientation of human limbs. But these inertial sensors have the nagging problem of accumulating errors over a period of time. The low-cost IMUs currently available in the market are lacking the accuracy needed for precision tracking applications. Hence the focus in this thesis is to develop a low-cost IMU that could be used in motion tracking systems. The resulting device is named yIMU.

This chapter is divided into five sections:

1. In this section, we introduce the Inertial Measurement Unit and their applications. We also delve into the background theory to further understand the working principle of navigation systems based on inertial sensors.
2. In this section, we look into the application of inertial sensors for tracking human motion. Bunch of concerned applications have been mentioned pointing to the commerciality of the technology.
3. Here we survey the relevant body of literature to develop our system. The focus was to look at the efficient techniques that could be implemented and refined to develop a cheap, compact and accurate inertial tracking solution in a limited budget

and development cycle. Furthermore, the limitations in previous research are highlighted and the suggested steps to be taken is discussed.

4. Here we state the objectives that need to be accomplished in this thesis and the broad methodology followed is mentioned.
5. Finally, the outline of the remainder of the thesis is presented.

1.1 Inertial Measurement Unit

Given the initial position and orientation of a body, inertial sensors can be used to track the motion of the body in time. The technique/process used is known as inertial tracking. An Inertial Measuring Unit is a device with accelerometers and gyroscopes that are used to measure linear accelerations and angular velocities respectively. Most IMUs even have magnetometer to assist in aiding the orientation. These physical quantities can be integrated over time to obtain an estimate of the positions and orientations of the body. But this requires development of appropriate sensor fusion algorithms, to take into account the propagation of integration errors of the sensors. But the cost and size of MEMS IMUs render them suitable for various consumer electronics, automobiles and are especially popular amongst hobbyists.

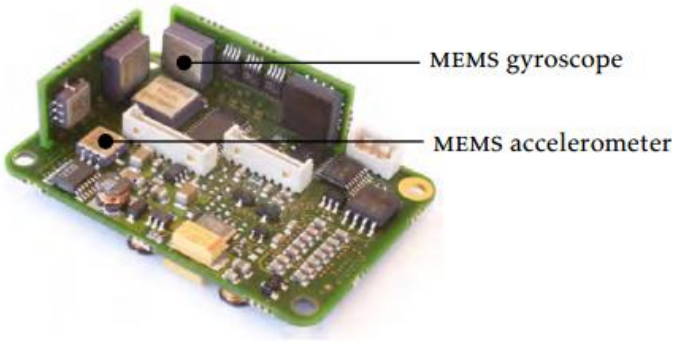

Figure 1.1: A circuit board of an IMU containing MEMS component

1.1.1 Operational Principle

Though the IMU system appears to be complicated the physics is surprisingly simple. Angular velocity can be measured by exploiting the Coriolis Effect of a vibrating structure; when a vibrating structure is rotated, a secondary vibration is induced from which the angular velocity can be calculated. Acceleration can be measured with a spring suspended mass; when subjected to acceleration the mass will be displaced. The mems technology is used to implement these mechanical structures on silicon chips in combination with capacitive displacement pickups and electronic circuitry.

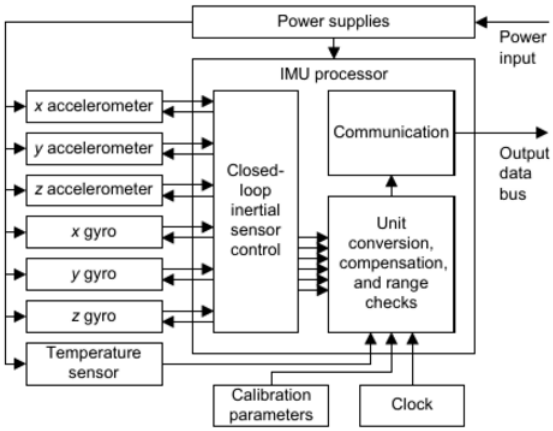

Figure 1.2 : Schematic of an Inertial Measurement Unit (Groves 2013)

Accelerometers- Accelerometers theoretically measure 'specific force' the sum of linear acceleration and gravity. In quasi-static situations, linear acceleration can be neglected with respect to the gravity and sensor measurements can be used to estimate the orientation relative to the horizontal plane. However, in a dynamic situation (free motion) the accelerometer measures both the linear acceleration and gravity. In this case, it is not easy to dissociate these two physical quantities, and thus, it becomes difficult to calculate the attitude accurately.

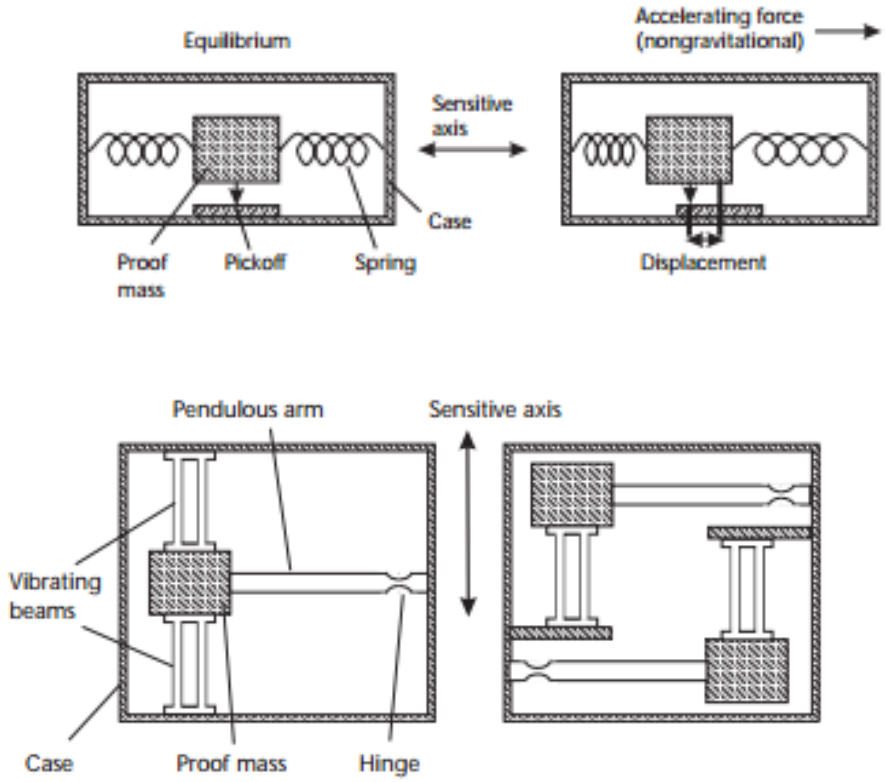

Figure 1.3: Principle of operation of MEMS inertial sensors: (above) accelerometers (below) gyroscopes (Groves 2013)

Gyroscopes- Gyroscopes measure angular velocities which can be integrated over time to compute the sensor's orientation. Nonetheless, the integration of gyroscope measurement errors and biases leads to an accumulating error in the calculated orientation.

Magnetometers- Magnetometers, on the other hand are used to measure the local magnetic field vector in sensor coordinates and allow the determination of orientation relative to the vertical axis, which provides additional information regarding orientation. The main problem with magnetometers is the influence of magnetic interferences fixed to the sensor frame or ferromagnetic materials around the sensor that corrupt the measurements.

1.1.2 Grades of IMUs

Based on the price and performances characteristics inertial sensors are categorized into many grades:

1. STRATEGIC GRADE

   The best among these belong to the category of strategic grade which includes marine and navigation grade sensors. These sensors are so accurate that the system will only drift by less than 1.8 km per day (VectorNav). But they are very expensive with aviation grade costing around $100000 per unit with marine grade costing in the neighborhood of a million dollars for a full system. The technology used to create these gyroscopes are usually Ring Laser (RLGs) and Fiber Optics (FOGs).

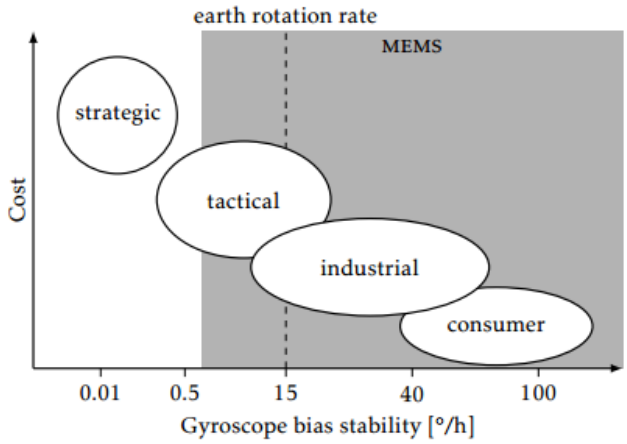

Figure 1.4: Inertial sensor grades (Hol 2011)

2. TACTICAL GRADE

   Tactical grade sensors are widely used in military munitions and navigation systems for UAVs. These sensors can be used unaided for a few minutes, but with accurate external aiding like GPS these systems can be very accurate. They usually cost tens of thousands of dollars.

3. INDUSTRIAL GRADE

   Industrial sensors are used in automobiles, medical devices and industrial automation applications. They usually cost few hundred dollars to thousands of dollars depending on performance.

4. CONSUMER GRADE

   The lowest grade is consumer grade sensors which are usually made based on MEMS technology making them cheap. Usually industrial grade sensors are just better calibrated consumer grade sensors, the difference in this range is due to sophistication of the calibration process. Consumer grade IMUs are very cheap and could be found for less than $5.

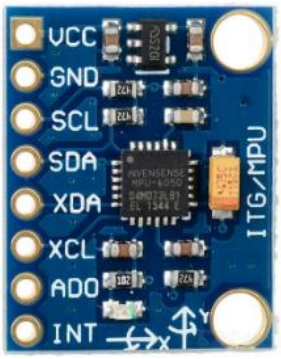

Figure 1.5: MPU6050 breakout board: a consumer grade sensor used for this project

The range of inertial sensors from automotive to marine grade spans six orders of magnitude in gyroscope performance. These divisions in performance is usually based in the bias stability specifications. Bias stability is the measure of the variation of gyroscopic bias with respect to time. The more stable it is, the better the IMU. Tracking estimates are heavily dependent on the gyro performance, hence better the gyro less the errors in the estimates.

1.1.3 Inertial Navigation System

An inertial navigation system (INS) is a navigation aid that uses a computer, motion sensors (accelerometers) and rotation sensors (gyroscopes) to continuously calculate via dead reckoning the position, orientation, and velocity of a moving object.

Dead reckoning- is the process of calculating the current position of a vehicle by using a previously determined position, updating that position based upon known or estimated speeds over elapsed time and course. Due to integration errors the calculations are prone to being erroneous over time.

Basically an INS consists of the following:

- An *IMU* or an *inertial reference frame* (IRF) consisting of sensors which are rigidly mounted. This is used to measure the pose of the body.
- *Navigation computers* to make the estimation calculations.

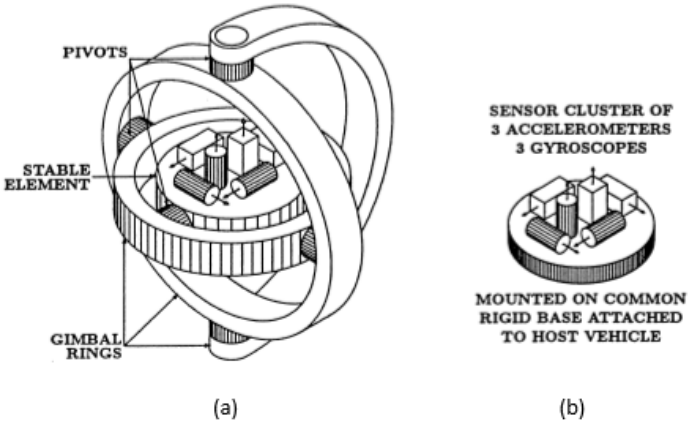

Figure 1.6: (a) Gimbaled inertial measuring unit (b) Strapdown inertial measuring unit (Grewal, Weill et al. 2001)

The system design can be broadly divided into two categories:

- *Gimbaled systems*- use a multiple gimbal framework with rotation bearings for independent rotation of attached frames from the host vehicle. At least three gimbals are required to isolate the system from host vehicle rotations about three axes (roll, pitch and yaw). These systems are expensive but have very high accuracy. This is especially useful for applications where GPS aiding is not available e.g. in submarine navigation.
- *Strapdown systems*- have the inertial sensor cluster rigidly mounted onto the host vehicle. The wearable sensor systems under discussion can be categorized as strapdown systems. These systems have much higher rotation rates than gimbaled

systems which requires compensation mechanisms to give accurate output. The following flowchart shows the simplification of computing tasks involved in calculation of pose using a strapdown inertial navigation system.

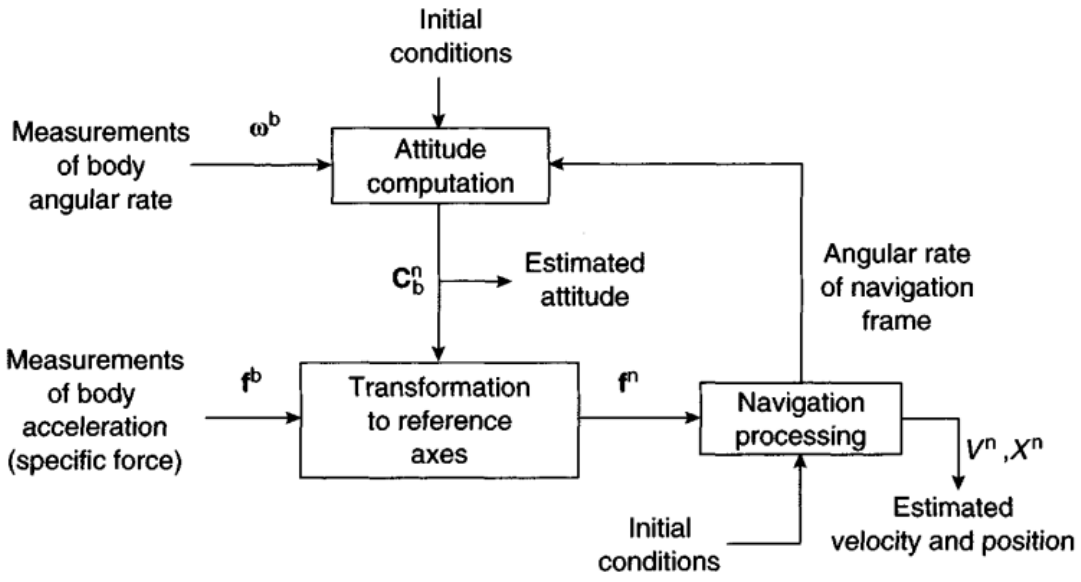

Figure 1.7: Strapdown inertial navigation computing tasks (Titterton and Weston 2004)

1.1.4 System Applications

Wide array of applications in aircraft and spacecraft navigation and attitude control systems; missiles and other munition applications; marine navigation. Recent advances in MEMS technology have drastically reduced the price and size of inertial sensors thereby ushering in extensive applications in consumer electronics and automotive industry.

IMUs have a great utility advantage over other navigation sensors like GPS and magnetic compasses in that they can be used in varying environments where those sensors cannot be

used. For navigation purposes IMUs are used in combination with a secondary navigation sensor to check the growth of errors in measurements. Kalman filter is extensively used to update the readings to generate a more accurate dead-reckoning result.

1.2 Human Motion Tracking using Inertial Sensors

Human motion tracking is a vast field with many areas under its purview. In this section, we present a brief description of areas of research currently undergoing lot of improvements. At the end we summarize the advantages and disadvantages of using inertial sensors for human motion tracking.

1.2.1 Rehabilitation Studies

Human gait analysis has been a field of interest for research since a long time. This is motivated by the wide range of applications in the field of medicine, sports, animation and defense. The research has focused on demystifying the complex nature of human gait, supporting the human body for medical applications, augmenting the human body to exceed its performance limitations, and motion capture for animation and to improve the performance in athletes.

Using inertial sensors to track human is one of the most economical and effective methods. In gait analysis using wearable sensors, motion sensors are worn or attached to various parts of the patient's body, such as the foot and waist. These sensors (like accelerometers, gyroscopes, force sensors, strain gauges, inclinometers, goniometers, etc.) can measure gait characteristics which may then be used specific applications. For an example, the wearable sensor data can be used in detection of gait phases based on measurement of ground

reaction forces (Kong and Tomizuk 2009) and monitoring of human gait based on the same principle (Zhang, Tomizuka et al. 2014).

1.2.2 Gait Augmentation

Human gait refers to the human mobility due to motion of legs. Over the course of evolution humans have developed to have bipedal locomotion. Before the invention of agriculture, humans have been known to be migratory species. Being bipedal allows humans to travel large swathes of territory in an efficient manner. In fact, even in modern era walking is more efficient than using automobile to traverse rugged terrain and in many adverse environments.

Soldiers often need to carry heavy loads in trying physical and psychological conditions. Over an extended period of time, a drastic reduction in degradation in efficiency and decision making ability has been documented which could prove ominous to the mission as well as hazardous to the soldier.

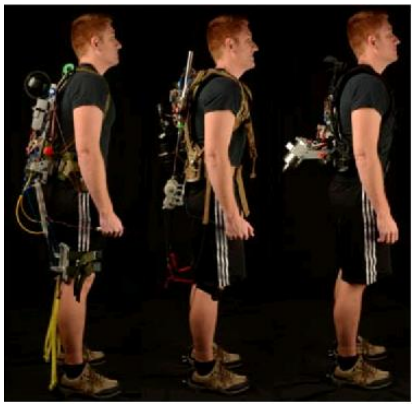

Figure 1.8: Devices designed to augment human running developed at Human Machine Integration Lab, ASU: (from left to right) AirLegs V1, AirLegs V2 and Jet Pack **(Kerestes 2014)**

There is a cost-effective solution to this problem- gait augmentation. The goal of gait augmentation devices is to supply additional amounts of torque at appropriate time during locomotion to decrease the metabolic energy consumption. This in turn would increase the efficiency and performance of the individual i.e. increase in range, endurance and speed of locomotion.

It is to be noted that leveraging the power available to soldiers for movement is not the only application of gait augmentation. Disabled patients and elderly population who are in need of walking assistance could also benefit from these devices. Proper use of these devices may result is drastic reduction in assistance required from physical therapist thereby reducing the cost of treatment considerably.

The HESA (Hip Exoskeleton for Support and Augmentation) is one of the exoskeleton devices designed by Human Machine Integration Lab at *ASU that could accomplish the above set goal. The idea is that of a device that could provide support and torque to the hip during normal gait to reduce the metabolic cost on human body.

Figure 1.9: eLegs developed at Berkeley Robotics and Human Engineering Lab (eLegs 2010)

Gait augmentation could be successfully implemented only if accurate orientation of hip with respect to torso, i.e. angle about the pelvic joint, is known. For HESA we use two IMUs: one mounted onto the hip and the other to the torso.

1.2.3 Motion capture

Every human gait research deals with motion capture which can be achieved by various sensing methods: optical, mechanical, magnetic, acoustic, or inertial tracking. Although much less expensive and more portable than marker-based optical systems, marker less solutions are still lagging behind the more expensive systems in terms of the achieved accuracy. A comparatively new and quickly developing frontier on human motion capture system is based on the use of wearable sensor units comprised of magnetic and inertial sensors that are attached to the objects in order to track their position and orientations. Some of the most often used contemporary commercial motion tracking systems are the Xsens, Intersense, Perception Neuron, Synertial and Trivisio.

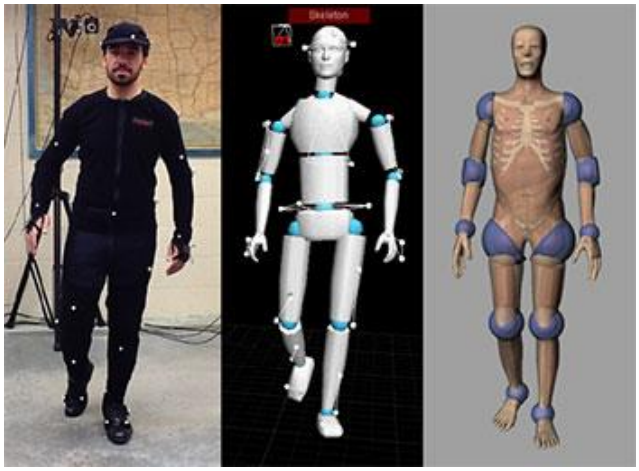

Figure 1.10: Rendering for an inertial mocap system (PerceptionNeuron)

1.2.4 Summary

The overarching goal of the research is taking first step to devise a portable wireless tracking system that is both robust and economical to be used by people to help them in their activities. Here MEMS based inertial tracking systems lead hands down due to their versatility and economic accessibility. But they have a bunch of limitations that needs to be addressed before they can be effectively used in human motion tracking.

Advantages of MEMS based IMUs-

1. Light weight and portable systems.
2. Economical as the MEMS based inertial sensors are order of magnitude cheaper than other varieties.
3. No inherent latency associated with this sensing technology and all delays are due to data transmission and processing (Fourati, Manamanni et al. 2013).
4. No requirement of an emission source- electromagnetic, acoustic, and optic devices require emissions from a source to track objects.
5. Enable unhindered movement of the human subject and no problem of occlusion.
6. Data collection is unrestricted by the requirement to stay in the laboratory environment.
7. Ease of use as not many accessories are needed for setting up the tracking system.
8. Huge amount of data collection is possible i.e. from many gait cycles.
9. Using accelerometers to avoid errors related to differentiation of raw displacement data (Kavanagh, Morrison et al. 2006).

10. Excellent sensitivity even for small displacements. This proves to be extremely useful in medical diagnostics and rehabilitation.
11. Cost effective and widely available sensors
12. High sampling rate
13. Can work in total darkness (unlike optical systems) and can work in unconstrained environments.

Notwithstanding the above advantages over other mainstream motion capture systems, the inescapable downside is the measurement accuracy of MEMS IMUs. Their outputs are corrupted by several high power error components. During the unaided mode of operation, these high power error components quickly accumulate in the navigation states leading to unacceptable navigation solutions in a very short period of time (Yuksel 2011). Also sensors are sensitive to locations on the body and require multiple sensors for capturing full body movements which can be annoying at times.

As we can see the errors are temporal in nature and highly dependent on the application for which it is used. As a result, an application specific aiding source is required to correct this propagation of measurement errors. The combination of GNSS/INS to improve the measurement accuracy for motion capture could be done (Kwakkel 2008). GPS is well known to give erroneous measurements over a short time span. On the other hand, INS is reliable over short time span but degrades over an extended period of time. Hence using the complementary characteristics of these both systems would result in a highly accurate tracking system.

But if the problem is modified to not include any assistance from external sources (like GPS), the solution will lead to an autonomous inertial tracking system. In this pursuit of autonomous tracking system to find the relative orientation of human limbs, the application of kinematic constraints to cap the measurement errors appears to be an apt solution.

1.3 Previous Work

Researcher working in this area have reported that due to propagation of integration errors in inertial sensors, it is impossible to get accurate angle and displacement estimates. But with smart signal processing techniques these errors can be reduced. Integration error components quickly accumulate in the navigation states leading to bad tracking results in a drift of 10^0- 25^0 after one minute and double integration of accelerometer data leads to positional error that varies cubically with time (Roetenberg, Luinge et al. 2005).

Slifka (Slifka 2004) had developed a double integration scheme for accelerometers that was able to measure displacement with an error of less than 10 percent. Part of the error is inherently due to the process of numerical integration which could be further minimized by increasing the sampling rate. But this was tested on a linearly constrained vehicle body. Benoussaad et al (Benoussaad, Sijobert et al. 2016) devised a more elaborate method for step height detection using double integration and drift cancellation assisted by gyroscopes. This algorithm had error under 15% when tested on subjects walking at various speeds. This approach did not work for extended periods of time. In addition, they did not use low cost sensors for their applications. Whereas Barret et al (Barrett, Gennert et al. 2012) have used consumer grade sensors to develop an improved IMU by implementing calibration

procedure to improve performance. Though the techniques are exhaustive and inexpensive, it is time consuming and the accuracy for tracking applications have not been determined.

In order to further increase the navigation accuracy of low cost MEMS redundant IMUs have been used. Skog et al (Skog, Nilsson et al. 2016) have created a multiple IMU array for pedestrian navigation tracking and other applications. These systems use a very large array requiring lot of processing power and battery life, in addition to use of magnetometers. The type of sensors used and the technique of data extraction determine the limitations of a particular application. Use of magnetometers lead to interference problem with background magnetic fields. Using accelerometers alone lead to unreliable data over a long time span. Even if accelerometer data is fused with gyroscope the resulting estimations are accurate for only a small time span. The use of aiding source is hence very important for a reliable system. Greenheck et al. (Greenheck, Bishop et al. 2014) have development a multi IMU platform for orientation tracking of small satellites. But the device is still in early prototyping stage and the precision still needs to be much better for the intended application, besides the fact that the form factor would still be much bigger than expected. The intended technique heavily depends on just averaging the IMU raw outputs without any processing hence not much improvement can be expected in dynamic situations. Use of multiple sensors or application-based modelling constraints is very important to increase the performance of low-cost IMUs. But using multiple sensors increases the state and observation model dimensions thereby leading to highly nonlinear dynamic equations which makes the filter algorithms complex and increases the chance of instability.

Hence, in order to maximize the performance of IMUs for tracking application addition constraints must be applied especially for human tracking applications. Taunyazov et al (Taunyazov, Omarali et al. 2016) have developed a system for tracking upper limb using an IMU in addition to a potentiometer. The tracker system is mechanically constrained hence is not a purely inertial tracking system. (Masters, Osborn et al. 2015) have developed a low cost inertial tracking system with low cost materials. The angular tracking accuracy is RMSE 2.9^0. The system is then applied to prosthetic evaluation testing, trajectory analysis and neural correlation studies. But the system is based on open source algorithms and uses magnetometer for increasing tracking accuracy. Hence though the viability of being able to develop a low cost system is proven, there is no original contribution for attaining greater accuracy of tracking. This is where kinematic constraints play a key role. Roetenberg et al. (Roetenberg, Luinge et al. 2013) used model based sensor fusion in addition to sensor fusion using Kalman filtering to track 6 DOF motion of human body. The system employs magnetometers and the commercial package is quite expensive. In comparison, El-Gohary (El-Gohary and McNames 2015) has developed a sensor fusion scheme for tracking joint angles using Unscented Kalman filter that uses two inertial sensors unaided by any external sensors. The technique used to prevent errors depending on applying kinematic constraints to limit the range of estimated in the Kalman filter. This is a good idea as the range of motion of human joint movement is limited and can be mapped. In addition, a joint update methodology was used to detect stationary periods and zero-in the angular rate estimates. This is an original idea which was previously used only in heel strike updates. The resulting algorithm has been tested for complex movements with good results. But the algorithm is complex and they do not use consumer grade

sensors. UKF maps the uncertainty of estimate by drawing a certain amount of sample points around the mean, propagating them through non-linear functions and recovering the resultant mean and covariance.

1.3.1 Addressing the Limitations

Based on work done by previous researchers it can be concluded that in order to create a very accurate low-cost IMU there should be improvements in the following areas;

1. A simple and fast calibration of the IMU to account for various errors
2. Signal processing of the raw sensor signals to remove noise
3. Efficient sensor fusion algorithm
4. Using redundant sensor arrays to improve the noise performance

To execute each of the above step is traditionally an expensive and time-consuming process. Hence for low cost IMUs such accurate calibrations are usually not done. This poor calibration leads to systematic errors. This performance further degrades when the operating conditions are not favorable e.g. vibrations, temperature variations, etc. In order to develop a low-cost product, we had to device a cost effective and accurate procedure to extract high quality data from the consumer grade IMUs used in the project. In order to solve the above stated problem multiple IMUs can be used to increase the stability and reduce the noise of the data collected thereby increasing the accuracy of the data to acceptable levels.

The problem of developing a highly accurate low-cost IMU was tackled in chapter 2 of the thesis. Most importantly a new system was developed to calculate the pose without using any external aiding (magnetometer). As this system uses no magnetometer, the person

wearing the tracking system need not be concerned with interference from ferromagnetic material present in his vicinity. Also the system is not afflicted by the problem of occlusion in camera tracking systems.

1.4 Objectives and Methodology

The aim is to build an improved low-cost MEMS IMU which could then be used to build a cost-effective human motion capture system. In accordance to this objective the following steps were taken to build yIMU:

1. Accurate error modelling of low-cost IMU and simple calibration to reduce the accumulative errors.
2. Apply appropriate signal processing techniques to further improve the precision.
3. Implementation of a simple sensor fusion algorithm for orientation tracking.
4. Design of compact hardware.
5. Assess the performance of yIMU.
6. Prepare a kinematic model of human limb for joint angle tracking
7. Assess the system performance

1.5 Outline

The organization and overview for the remainder of the thesis:

- Chapter 2 (Development of Low-Cost Inertial Measurement Unit: yIMU) discusses the design and building of a novel low-cost IMU. Firstly, the error model used to characterize the behavior of IMU is described followed by using a simplified model for building yIMU. Following this, the calibration techniques have been described. Next, we delve into the development of the attitude tracking algorithm to calculate

the orientation in 3D space. Details of the process of fabrication of the IMU hardware is then discussed. Finally, the performance evaluation of the IMU is done with special consideration to testing the validity of using an opposed configuration system. The tremendous improvement to yaw stability is then proved.

- Chapter 3 (Joint Angle Tracking using Inertial Sensors) is devoted to describing the process of developing a simple joint angle tracking algorithm. Kinematical modelling of human upper limb segment is discussed- this involves the assignment of sensor frames of reference, generation of DH parameters and computation of transformation matrix. Then we mention the process of sensor-segment orientation for aligning the body axis frame of the sensor to respective human segment frame. This is followed by an experiment to test the accuracy of the system.

- Chapter 4 (Conclusion) gives a succinct description of the results obtained and proposes the subsequent inferences pointing to the contribution of this thesis. It also discusses the future scope of the work and the suggestions for improvements.

Chapter 2

DEVELOPMENT OF LOW-COST INERTIAL MEASUREMENT UNIT: yIMU

In this chapter we discuss the development of a low-cost IMU built on Arduino platform. As a precursor to building an accurate motion tracking system, there was a need to have a highly precise low-cost IMU. This is the first step to bring such inexpensive inertial sensors closer to tactical grade performance which would lead wider applications.

In order to achieve better performance, a dual IMU system was chosen that would lead to better noise performance of the overall system. Experiments were done to validate this argument. An effective error model for the sensor was built along with an efficient compensation scheme to remove stochastic and deterministic errors from the sensor measurements. This was followed by a simple calibration scheme based on the proposed error model. We also performed a range of detailed tests to understand the nature of sensor signals. Once the drift and noise from the raw sensor readings were eliminated a quaternion based complementary filtering scheme was implemented. The choice of a complementary filter was done to reduce the computational burden on IMU and to increase the battery-life. Later, the hardware design of yIMU was finalized followed by experiments to evaluate the performance of yIMU.

Based on this it can be surmised that a novel IMU has built that can be effectively used for human motion tracking applications.

2.1 Error Modelling and Calibration

Low-cost mems IMUs are not precisely calibrated, hence are affected by various error sources. This leads to non-accurate scaling, sensor axis misalignments, cross-axis

sensitivities and non-zero biases. In order to increase the accuracy, they need to be calibrated. Identifying the sources of errors afflicting the system is known as error-modelling and is the first step in the direction of calibrating the IMU. Nevertheless, it has to be acknowledged that in order for the system to run on Arduino an elaborate error correction scheme cannot be realistically implemented. Hence a simplified error model has been built.

In order to minimize the measurement errors in inertial sensors, we need to mathematically model errors, according to the sources of these errors. Once this is done, we can compensate for the errors in the measurement equations. In general, these errors can be divided into two broad categories: deterministic and stochastic (Unsal and Demirbas 2012). Calibration is defined as the process of comparing instrument outputs with known reference information. Consequently, the coefficients are determined that force the output to agree with the reference information for any range of output values (Aggarwal, Syed et al. 2006). As mentioned before, calibration of the IMUs is of paramount importance to reduce the deleterious effects of sensor drifts and noises. Hence, a simple calibration scheme has been followed to meet this requirement. For more in depth treatment of inertial sensor principles refer (Woodman 2007).

It is important to have a rigorous understanding of the nature of signal to effectively model it. In section 2.1.4-2.1.7 we do this by performing a slew of tests. Allan variance analysis and Power Spectrum Density Analysis is done to confirm the “color” of the constituent signals of inertial sensor. This is important as the probabilistic model we chose to depict the stochastic error of the sensors depends on it. Next to confirm the Gaussian nature of

the signal we perform a Probability Density Function analysis. Usually when modelling sensor errors it is assumed that the noise predominantly White Gaussian of nature, but to be sure of whether this hold true and to what extent for MPU6050, these tests need to be done. This would provide rigor to the discussion in section 2.2.2. Finally, we also perform drifting bias analysis. This is seldom done as good sensors display this effect over an extended period of time, for short interval usage (like 10 minutes) this seems to be an overkill. But if we were to be able to apply yIMU for long-term navigation applications, this might prove to be useful. These tests provide the groundwork for development of future more complex sensor fusion algorithms based on the present system.

2.1.1 Types of Errors

Deterministic errors are the kind of errors that can be easily modelled as either they remain constant and their variations can be simplistically modelling. The quantification of these errors does not change with time regardless of the state of the system. These errors are highly temperature dependent hence for advanced calibration usually a lookup table is generated via laborious experimentation and accordingly compensated in the equations (Barrett, Gennert et al. 2012). Deterministic errors can be categorized as follows:

1. STATIC BIASES

   This is an offset bias that can be noticed at the beginning of collecting raw data from the IMUs. This is a constant error independent of measurements taken. A constant bias when integrated causes angular error to grow linearly with time. The same integration if done twice on accelerometer data to get distance leads to large

quadratic errors. These can be corrected by averaging the measurements and subtracting the offset from the initial measurements.

$$\theta(\boldsymbol{t}) = \boldsymbol{c}.\boldsymbol{t} \qquad \textbf{(2.1)}$$

where **Θ** is the integrated angle, **c** is the error that that grows linearly with time **t**.

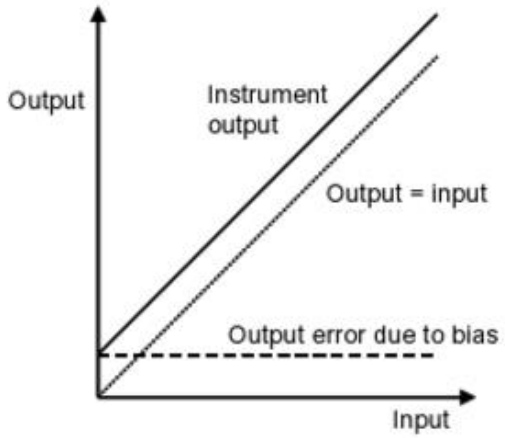

Figure 2.1: Static bias error (Groves 2013)

2. SCALE FACTOR AND MISALIGNMENT ERRORS

Scale factor errors are multiplicative errors that lead to changing the slope of the sensor measurements. It is to be noted that there is a non-linear term in the scale factor too but it is usually modelled into once parameter for simplicity.

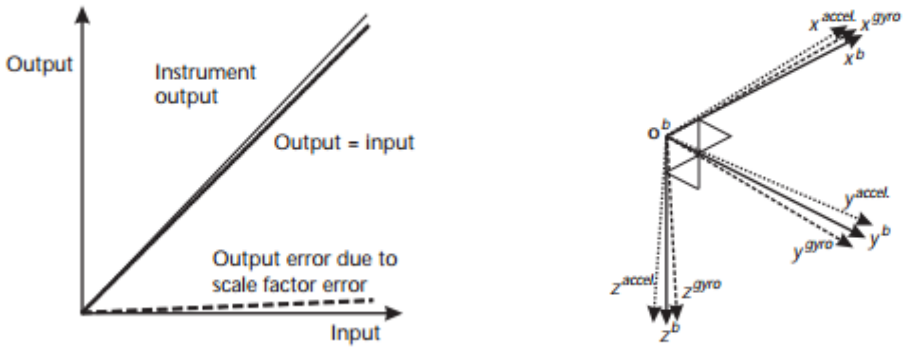

Figure 2.2: (left) Scale factor error; (right) misalignment error (Groves 2013)

Misalignment errors are due to non-orthogonality in the placement of the sense axes either in the die or the external packaging of the IMU. These are also known as cross-coupling errors and occur due to manufacturing limitations. Misalignment errors lead to contributions to scale factor errors but usually this is much less in magnitude.

The following simple equation is representative of these errors:

$$\boldsymbol{x_{measured}} = \boldsymbol{SF} \text{ x } \boldsymbol{x_{actual}} + \boldsymbol{B} \qquad \textbf{(2.2)}$$

where $\boldsymbol{x_{measured}}$ is the value of inertial quantity (specific force or angular rate) measured by the sensor, **SF** is the scale factor error, $\boldsymbol{x_{actual}}$ is the actual value of inertial quantity, B is the bias coefficient. It is to be noted that though bias is predominantly static, it also contains random bias component discussed as part of stochastic errors.

Stochastic errors have their source in random processes. This means that these errors cannot be modelled deterministically and we have to use a probabilistic model as these errors are non-repeatable and unpredictable meaning there may not be any direct relationship between input and output. White noise can be removed only by sacrificing the bandwidth of the sensor as it cannot be removed by calibration. The complexity of probabilistic model depends on the system on which it is to be implemented. The following are the different kinds of stochastic errors:

1. MEASUREMENT NOISE

   This a zero-mean random process that creeps into the measured sensor data. Usually modelled as the average error that is the result of high frequency white noise. The source of this errors cannot be pin pointed and are believed to be inherent to the nature of MEMS functioning and purported to be thermomechanical in origin.

   This can be calculated by using Allan variance analysis (see section 2.2.4). There we can find that the noise can be modelled as a white noise sequence with zero-mean uncorrelated variables identically distributed having a finite variance $\boldsymbol{\sigma^2}$. The following equation explains the effect of zero-mean random walk error into the integrated signal.

$$\boldsymbol{\sigma_\theta = \sigma\sqrt{\delta t . t}} \qquad \textbf{(2.3)}$$

   where $\boldsymbol{\sigma_\theta}$ is the standard deviation of the integrated signal that grows proportional to square root of time. Why is sensor measurement noise modelled as Gaussian

white noise? Because white noise has a power spectrum that is flat or equal valued at all noise frequencies, this can be seen in AV chart. Though we can assume for the sake of simplicity that measurement noise is white and model it anyway, for the sake of accuracy it is good to confirm how accurate our model will be by performing AV or PSD analysis (see sections 2.2.4 and 2.2.5). Similarly, in order to confirm the Gaussian nature of the sensor signal PDF analysis (see section 2.2.6) needs to done. This is important because then we can be sure of accuracy when we use White Gaussian Noise to depict sensor stochastic errors.

2. TURN-ON TO TURN-ON BIAS VARATION

   This is the variation in the static bias of the sensor due to transition in power cycle i.e. as the device is switch on/off the static bias values vary unpredictably. This is a dynamic bias component and usually measures 10% of static bias (Groves 2013). As the value if very small we have not given consideration in our simple model discussed in section 1.2.8.

3. DRIFTING BIAS

   This is also known as the random walk error. This is the random drift in the measured sensor values over time due to change is bias drift values. Usually a first-order Markov process is used to model the random component of the drift bias. This effect of this errors accrues over time and is not immediately felt for short durations. For highly dynamic movements though this has to be taken into consideration and modelled accordingly.

The nature of these errors have been discussed in more detail in sections 2.2.4-2.2.7, where we also discuss strategies to quantify or correct them in our sensor fusion design.

2.1.2 Temperature Compensation

The actual value of bias and scale factor obtained via calibration differ from operational value due to difference in temperatures. Hence an accurate thermal model is required. The importance of this cannot be understated as It is shown that the thermal variation of accelerometer bias may reach about 0.94 m/s^2 for ADI MEMS sensors and gyroscope drift can reach 5^0 /sec, over the temperature range from -25^0 C to 70^0 C (Aggarwal, Syed et al. 2006). Hence if these thermal variations are not corrected or compensated, it can lead to very large orientation errors.

For our case we used the ramp method (Shiau, Huang et al. 2012). First the IMUs are placed flat in the thermal chamber at room temperature. The chamber temperature is controlled to increase from room temperature to 65^0 C at approximately 1^0 C/min. At the same rate temperature is decreased to -10^0 C and then heated to room temperature. This cycle is repeated once more. The advantage of using this against the soak method usually used:

1. The total time of data collection is reduced as we do not wait for sensor temperatures to stabilize ate each point.
2. The amount of data points collected is increased for every point. 4 sets for each point as the same temperature is visited twice when heating and cooling.
3. The dynamic variation is mapped as there is continuous change in temperature.

The data is divided in temperature range sets: set1: 0^0 C to 20^0 C; set 2: 20^0 C to 40^0 C; 40^0 C to 60^0 C. Then the raw data is processed using MATLAB and a third degree polynomial fit drawn.

$$T = C_1 t^3 + C_2 t^2 + C_3 t + C_4 \quad \textbf{(2.4)}$$

Where **T** is the compensated parameter, **t** is the initial uncompensated parameter and $\mathbf{C_i}$ is the coefficient where **i= (1 to 4)**. The real-time data is collected using Megunolink Pro data acquisition software for Arduino. Figure 2.3 shows the effect of temperature compensation on gyroscope drift. The IMU is kept still for 2 minutes till the sensor temperature is stable. Then data is logged for 5 minutes. This is followed by heating the sensors till 55^0 C using a heat gun. For this experiment, the IMU was temperature compensated only for the range 20^0 C to 40^0 C and 40^0 C to 50^0 C. The gyro drift till room temperature of 23^0 C was close to zero. Between 23^0 C to 40^0 C the drift was around 3^0 for all the axes. Then the drift increases to 8^0 for Y axis and 4.5^0 for X and Z axes. by the end of 50^0 C. After that the drift increases uncontrollably for all axes with Y axes drifting as much as 20^0 at the end of the experiment.

It is important to note that in order to more accurately prepare a model for temperature effects on inertial sensors laborious tests need to be done cycled over weeks to confirm the repeatability of the compensation algorithm. Also in order to have highly precise model advanced algorithms need to be implemented that can involve Kalman filters, machine learning, neural network or even a combination of these. Implementation of these is beyond the scope of this thesis.

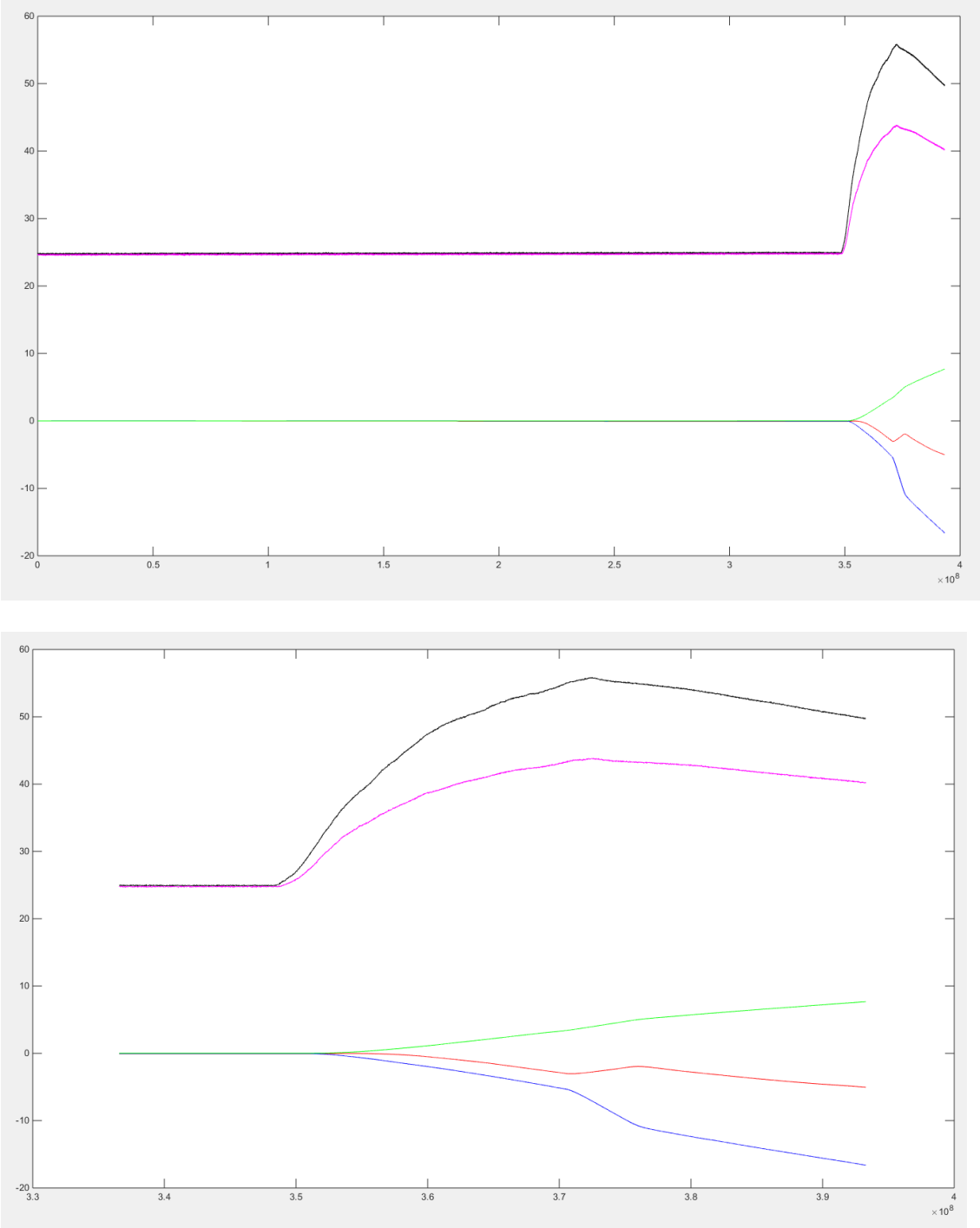

Figure 2.3: Temperature Compensation: Legend- gx (red), gy (blue), gz (green), temp1 (black), temp2 (magenta). (above) The plot for the whole duration; (below) The blown up version to show temperature compensation effect.

2.1.3 Static Bias Compensation

Static bias correction is much simpler than correcting other errors. A least squares technique (Hamdi, Mohammed I. Awad et al. 2014) was used to arrive at approximate values of offset bias for each of the axes of both gyroscope and accelerometer. The values are then stored internally in yIMU and subtracted from the raw reading to get stable readings. It is very important to remove bias from each axes individually before fusing them to ensure better correlation.

But we can notice that in the following figures there are improvements in the bias offset by virtue of combining opposed IMUs. Megunolink Pro was used to acquire data in real time for these experiments. See section 2.5.1 for evaluation of this effect.

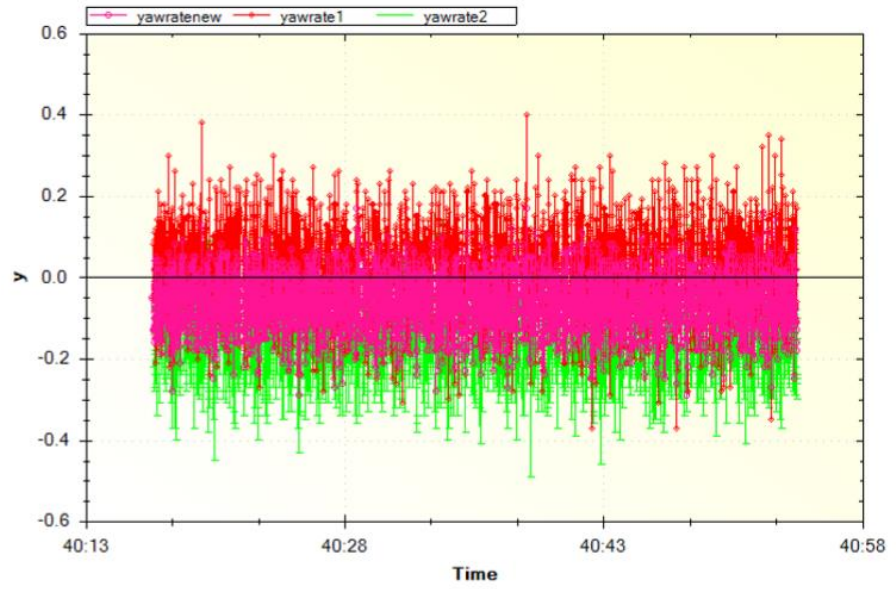

Series	Minimum	Maximum	Average	Last
yawratenew	-0.29	0.17	-0.065457	-0.13
yawrate1	-0.37	0.4	0.014581	0.17
yawrate2	-0.49	0.17	-0.14495	-0.1

Figure 2.4: The bias compensated angular yaw rate for the IMUs (Z axis): Pink is the combined yaw rate from IMU1 (red) and IMU2 (green)

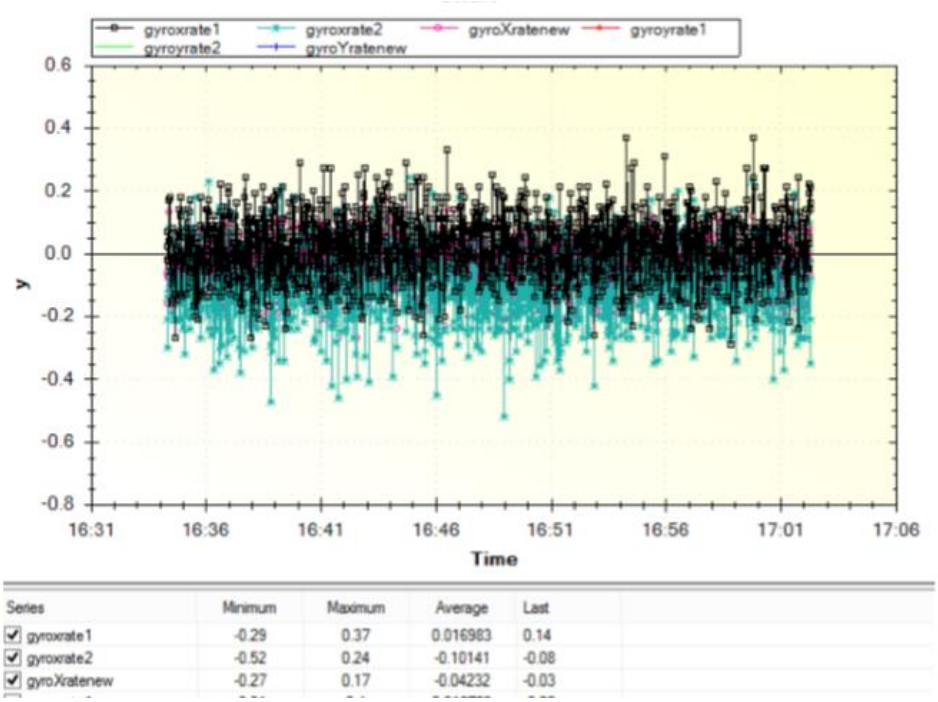

Figure 2.5: The bias compensated angular roll rate for the IMUs (X axis): Pink (not clearly visible) is the combined roll rate from IMU1 (black) and IMU2 (indigo)

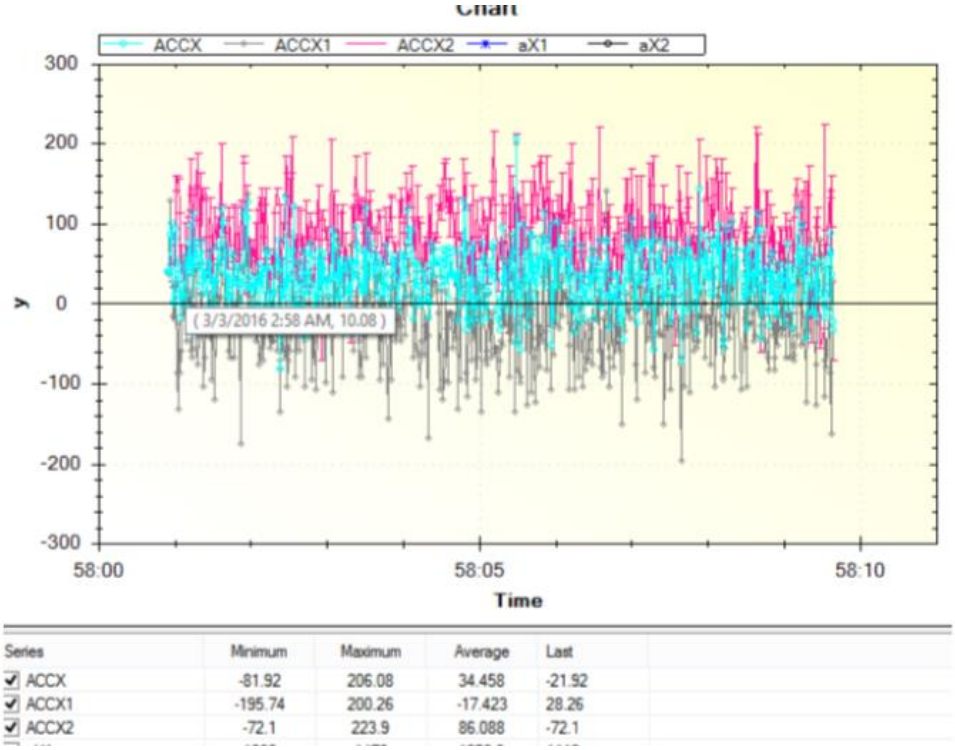

Figure 2.6: The bias compensated accelerometer readings for the IMUs (X axis): Indigo is the combined roll rate from IMU1 (grey) and IMU2 (pink)

2.1.4 Allan Variance Analysis

Allan Variance is technique to analyze dataset in time domain. Using this we can find out the noise in the system measurements as a function of time averaging i.e. it expresses the signal variance as a function of time window over which the signal is averaged. The results have been presented in section 2.5.2. In this section we describe the process.

For this we initially do a static test of the IMU for a long period of time. Usually up to 12 hours, but in our case due to equipment limitations, the test was done for 8 hours. It was deemed long enough for us to get a fair estimate of the required readings. For detailed analysis of drifting bias, longer duration of testing is necessary. The IMU is placed flat in

thermal chamber at 27^0 C. As the IMU is level and still, the only forces acting on it is due to earth rotation. And the only sources of errors are: drifting bias, measurement noise, static bias and misalignment errors. Before taking the readings though, it is necessary for the internal temperature of the IMU to stabilize, so the initial 10 minutes of the readings collected were ignored.

The static bias and misalignment errors can be removed by averaging the data and subtracting the offset. Hence we can see that the remainder of the errors in the readings have measurement noise and drifting bias as their source. Then Allan deviation plots for this data is calculated for further analysis, for more information of Allan variance method refer appendix A. What we are specifically looking for in this is the nature of measurement noise i.e. the color of measurement noise. Allan deviation function is unique to specific noise color i.e. the slope of the curve depends on the color of the noise: for white noise its $-\frac{1}{2}$; random walk noise is $+\frac{1}{2}$; and for pink noise its zero.

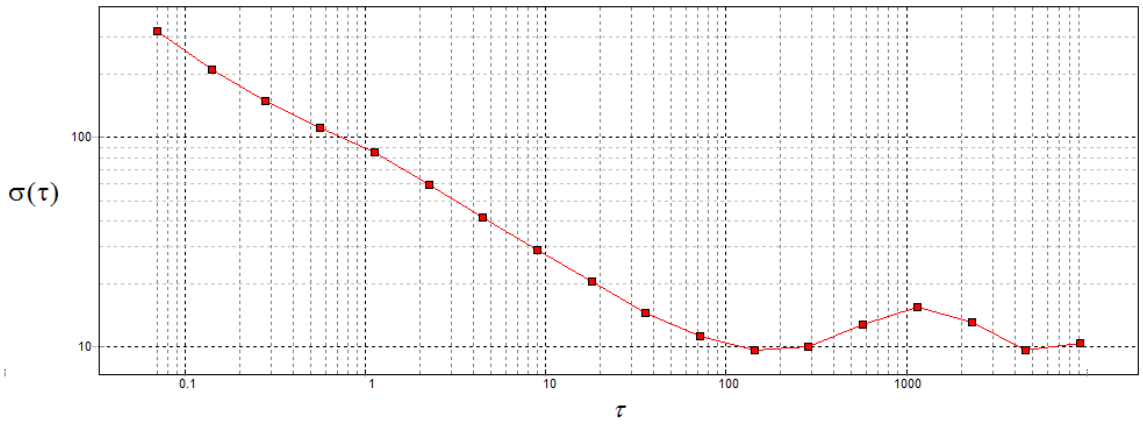

Figure 2.7: Sample Allan Deviation plot for an accelerometer

From the figure 2.7 we can note that the curves first decrease, flatten out then increase. In order to look for the effects of measurement noise we have to look at the first half of the

Allan deviation plot where the effect of measurement noise is predominant. This is because random walk noise accrues slowly hence initially the percentage of measurement noise in stochastic noise is much more than drifting bias. As the color of the noise and Allan deviation function are related we notice this effect on the slope of the curves. For results of this experiment see section 2.5.2. We can hence say that the measurement noise for yIMU can in fact be modelled as white noise.

2.1.5 Power Spectral Density Analysis

PSD analysis is used here to confirm the results from Allan variance analysis- we use it to identify the color of measurement noise in the sensor readings. We can determine the power of a signal at specific frequencies using this equation:

$$\boldsymbol{S(f) = F(R(\tau))} \qquad \textbf{(2.5)}$$

where **S(f)** is the PSD calculated by taking the Fourier transform of **R(τ)**, the autocorrelation function of the signal. We use AlaVar 5.2 to plot the PSD of inertial sensors.

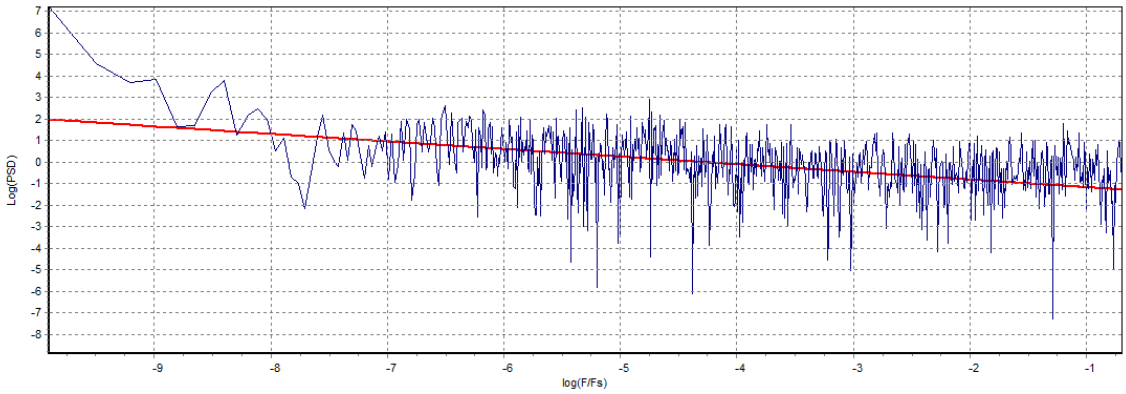

Figure 2.8: PSD for a sample accelerometer

We know that white noise has a power spectrum that is the same at all frequencies, hence this will show up as flat curve in the plot. Similarly, there are such correlations with other types of noise, but we will focus on the extent of noise that is white. This is discussed in detail in section 2.5.3. Based on this result we have confirmed the conclusion of Allan Variance analysis that the sensor noise is indeed white for yIMU.

2.1.6 Probability Density Function

Probability Density Function (PDF) is used to study the distribution of stochastic noise (predominantly measurement noise of inertial sensors) of a system. There are many different kinds of PDFs that might describe a distribution accurately, but the most useful of them all is Gaussian (normal) distribution represented by the following equation:

$$\boldsymbol{f(x) = \frac{1}{\sqrt{2\Pi\sigma^2}} e^{\frac{-(x-\mu)^2}{2\sigma^2}}} \qquad \textbf{(2.6)}$$

where μ is the mean and $\boldsymbol{\sigma^2}$ is variance of distribution **x**.

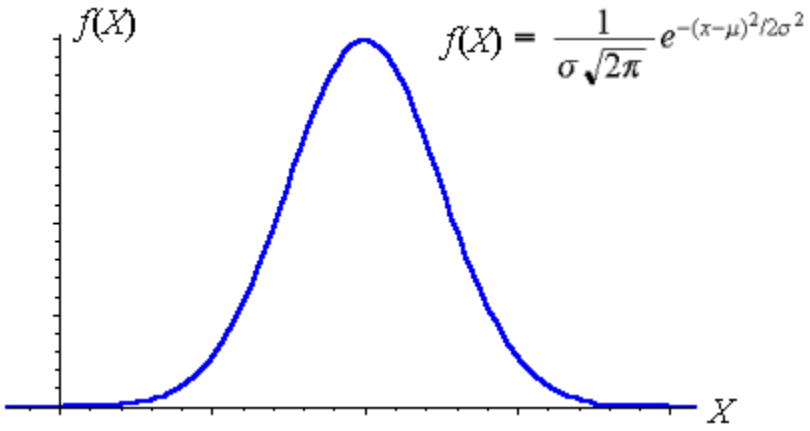

Figure 2.9: Visual representation of Gaussian distribution

The following are the reasons normal distribution is usually used:

1. Most of the systems can indeed be accurately represented by Gaussian PDFs. Hence in most of the cases IMU errors are also modelled using it.
2. Simple to implement as they have only two parameters:
    - μ is the sample mean
    - $\boldsymbol{\sigma^2}$ is sample variance
3. By nature of Gaussian distribution, simple manipulations (like adding, subtracting, etc) also result in a Gaussian distribution. Hence ease of calculations.

But it is important to note that not all low-cost sensors have characteristics consistent enough to be modelled using Gaussian PDFs. Hence, in the interest of curiosity this test was done to confirm the premise that the nature of measurement noise is not changed by using combining two sensors. In section 2.5.4 we will discuss the results in detail. Nevertheless, the conclusion is that we can use Gaussian distribution to model the probability distribution of the measurement noises of yIMU. Hence the use of White Gaussian Noise (WGN) for modelling measurement noise of yIMU has been validated.

2.1.7 Drifting Bias Analysis

As stated previously drifting bias is the bias component that is random in nature and cannot be precisely modelled deterministically. Due to this we notice the random variations in raw sensor readings hence the name- ‘random walk’. We approach this problem with a series of questions:

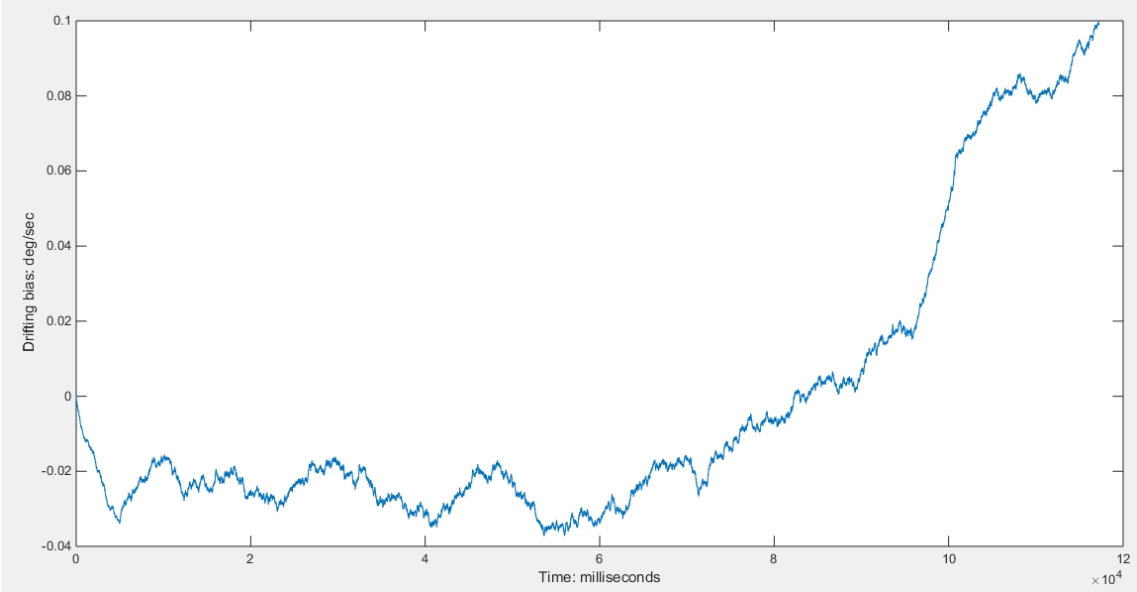

Figure 2.10: Random walk for a sample MPU6050 gyroscope

- *How to spot drifting bias in Allan variance plot?*

The purpose of Allan variance analysis is to visually map the behavior of stochastic errors. Drifting bias slowly accrues over time, hence larger the time span of raw data collect, larger will be the noticeable effect of drifting bias. We can see in the Allan deviation plots that later in the plot, the Allan deviation function curves up gradually (slope +1/2), this is due to increase in the error contribution due to drifting bias compared to measurement noise. This shows up towards the end due to the slow moving nature of drifting biases. In fact, this is the reason we are required to have the raw data collected over large span of time.

- *How is drifting bias modelled?*

In order to model the random walk behavior usually a first-order Markov process model is used (Barrett, Gennert et al. 2012) with the following equation:

$$\boldsymbol{b_d(i) = \varphi b_d(i-1) + \varepsilon(i)} \quad \textbf{(2.7)}$$

where $\boldsymbol{b_d}$ is the drifting bias at time **i**, **φ** is the scale factor, and $\boldsymbol{\varepsilon}$ is a zero-mean white Gaussian white noise process with unknown variance $\boldsymbol{\sigma^2_{bd}}$.

The reason for using Markov Model is:

- This model is simple with only two parameters- **φ** scale factor and $\boldsymbol{\sigma^2_{bd}}$ noise variance. Hence using these parameters in stochastic algorithms does not unnecessarily increase the complexity of the covariance matrix.
- Easy to implement into a state-space model and can satisfactorily represent highly dynamic systems.

The Markov process is a stationary process that has an exponential Autocorrelation Function (ACF). The ACF of a zero-mean first-order Markov process is defined by a decaying exponential form. As **φ** represents the amount of correlation that exists between any two data points in a drifting bias iteration, we can use ACF to obtain value of **φ.** Hence we calculate the ACG of the drifting bias data setting lag to 1 for a time step. The drifting bias data is obtained by removing the measurement noise component from the raw sensor data, this is done by implementing a moving average filter to the raw data.

Noise variance can be calculated by using the equation:

$$\boldsymbol{var(b_d) = \frac{\sigma^2_{bd}}{1-\varphi^2}} \quad \textbf{(2.8)}$$

- *Does using dual IMU system lead to any reduction in drifting bias?*

Yes, it does. See discussion in 2.7.7 for more information. But we notice that the overall effect of drifting bias is rather small to impact for small duration of usage, hence we need not include a special parameter for this in the simplified error model discussed in next section. In fact, the reduction due to using two IMUs in opposing configuration is small enough to deem this negligible for motion tracking purposes.

2.1.8 Simplified Error Model

Error modelling is the process of creating a mathematical model of the error sources of a sensor measurement in order to improve the measured physical quantity. The complexity of the error model depends on the application and the processing power available. Also analysis discussed in sections 2.2.4- 2.2.7 demonstrate the validity of using WGN model for stochastic errors and the drifting bias mitigation effect in yIMU. Keeping this in mind, following is the simplified error model that has been used in orientation estimation of yIMU:

$$\boldsymbol{a_m = a + b_a + n_a} \quad \textbf{(2.9)}$$

Where a_m is the measured value of acceleration (raw readings), **a** is the actual value of the measured inertial quantity (specific force), $\mathbf{b_a}$ is the static bias of the accelerometer, and $\mathbf{n_a}$ is the accelerometer noise. Similarly, we have,

$$\boldsymbol{g_m = g + b_g + n_g} \quad \textbf{(2.10)}$$

Where $\mathbf{a_m}$ is the measured value of gyroscope (raw readings), **g** is the actual value of inertial quantity (angular rate), $\mathbf{b_g}$ is the static bias of the accelerometer, and $\mathbf{n_g}$ is the gyroscope noise.

The static biases have been compensated as discussed in section 2.2.3. We have not compensated for scale factor/ misalignment errors in the equation as we did not have the equipment (precision rate table) to carry out the technique with enough accuracy to justify any real improvements in measurements. Temperature compensation was done as shown in section 2.2.2.

The noise part is interesting; we have relied on two techniques to compensate for it:

1. Common Mode Effect (CME)
2. Threshold filter

The details of using CME is discussed in section 2.2.2. According to our knowledge no other research group has used MPU6050 low-cost IMUs to successfully apply CME. This takes care of the stochastic errors (measurement noise, drifting bias and, environmental effects due to temperature and vibration) to a large extent as discussed in section 2.5. In addition, we have used a threshold filter to further remove the remaining noise components. The details of this have been discussed in section 2.3.

2.2 Dual IMU System

Using redundant sensor array is imperative to increase the performance of a low-cost IMU system if ever it has to rise to the level of tactical grade sensors. Inertial sensors arranged in pre-determined geometry to measure inertial quantities to exploit the design characteristic of the sensors such that the errors exhibited are smaller than those obtained by simple averaging (Yuksel 2011). For application to human motion tracking where the compactness and simplicity has to be taken into account, the use of a dual IMU system is justified instead of using large sensor arrays by exploiting the concept of common mode effect (Martin, Groves et al. 2013). The premise was that if the 3-axis sensors were arranged so their sensitive axes were facing in opposite directions when the output was combined the errors due to temperature and vibration (environmental effects) could be reduced.

2.2.1 Redundant IMUs

A single IMU is used to calculate inertial quantities. In order to seek better navigation solutions more than one IMU could be used to calculate the same inertial quantities but with greater performance- such system of sensor arrays are called as redundant IMUs. The information collected from these multiple sensors is processed to generate a virtual IMU. A detailed survey of the state of array techniques could be found in (Nilsson and Skog 2016). The exact technique used to generate this virtual IMU differs based on complexity of the system. An example of an INS + GPS fusion is given in figure 2.11.

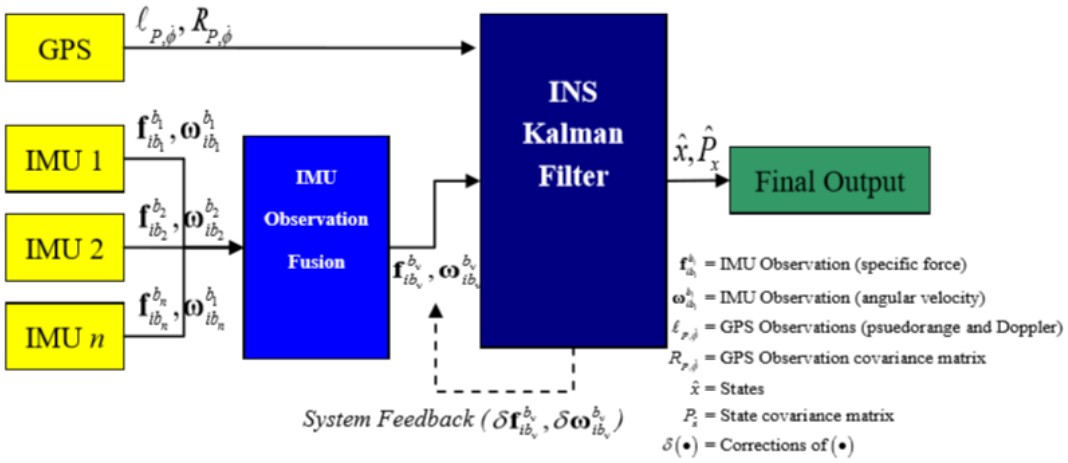

Figure 2.11: A virtual IMU observation fusion architecture (Bancroft and Lachapelle 2011)

Depending on the type of sensors, number of sensors, sensor fusion technique employed and application constraints redundant arrays have the following advantages:

1. The noise performance of the combined output is better due to averaging of stochastic errors. This leads to increase in the measurement accuracy of inertial quantities.
2. The dynamic measurement range could be extended beyond that of individual sensors by utilizing the spatial separation between the sensors (Skog, Nilsson et al. 2016).
3. Robust fault tolerance algorithms could be deployed for better redundancy in risky situations by including the redundant measurements in the covariance of the measurement errors so as to determine the reliability of the measurements. Not just faults in the system could be detected but also isolated to prevent propagation of those faults in the navigation equations (Groves 2013).

4. Geometrical constraints play a major role in assessing the quality of measurement with various skew-redundant techniques developed for advanced applications (Yuksel 2011).

2.2.2 Common Mode Effect

If the family of sensors is guaranteed to have similar external factor dependence characteristics, then these sensors can be formed into an array to be used to suppress those effects. A correlation between IMUs is shown by Yuksel et al (Yuksel, El-Sheimy et al. 2010) that reduce the temperature effect gyroscope bias which if applicable to MP6050 could be useful. This has been attested for MPU6050 as shown in section 2.6. This further reduces the computational complexity of the sensor fusion algorithm used in the low cost IMU.

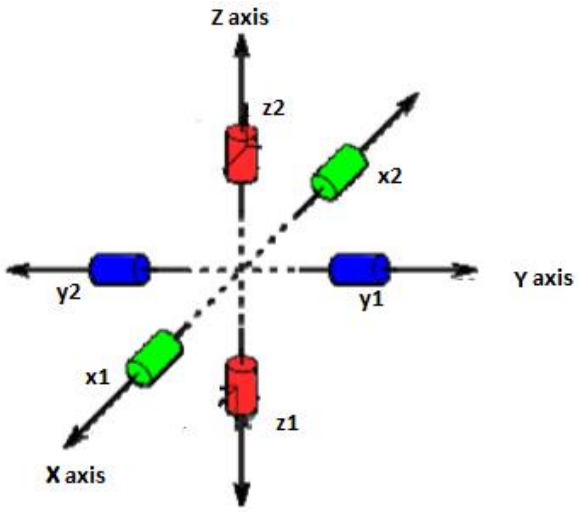

Figure 2.12: Dual axes configuration { based on (Yuksel, El-Sheimy et al. 2010) }

Theoretically this technique could work for correlated even order errors (Martin, Groves et al. 2013) e.g. If the static bias of a sensor is estimated to be positive always then

combining the data from two opposing axes could effectively reduce the error more so than just averaging them. Figure 2.12 shows the combined raw data for two IMUs in such a configuration. We can notice a huge improvement without using any extra computation complexity. This is the key to building an efficient orientation tracker. The important point here is that the sensor physical properties of in-plane and out-of- plane sensors should not vary. As no information about this could in the datasheet we contacted Invensense (the manufacturers) to check this. It was reported that there are no such variations due to manufacturing process.

From the results in section 2.5 we can see that we have in fact successfully applied this technique to MPU6050 IMUs. But how could we justify the cost of adding one extra sensor in the name of performance improvement? This is because calibration of MEMS IMUs is an expensive affair increasing the per unit cost of an IMU to hundreds of dollars (Martin, Groves et al. 2013).

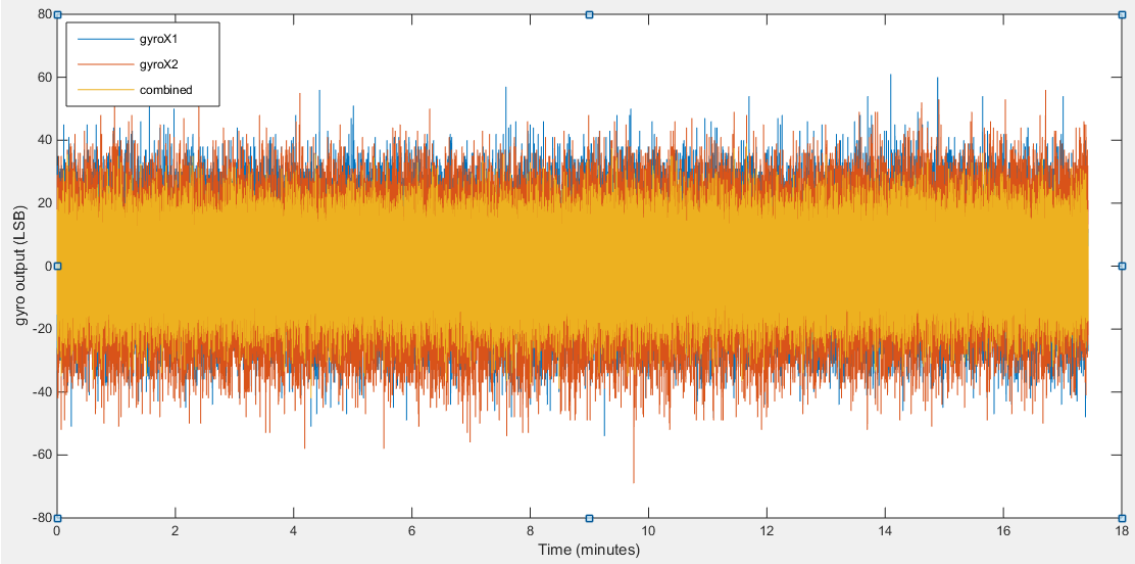

Figure 2.13: Gyroscope output (in LSB) comparison for two IMUs with opposed sense axes: std of gyroX1 is 12.9 LSB; gyroX2 is 13.84 LSB and combined is 9.417.

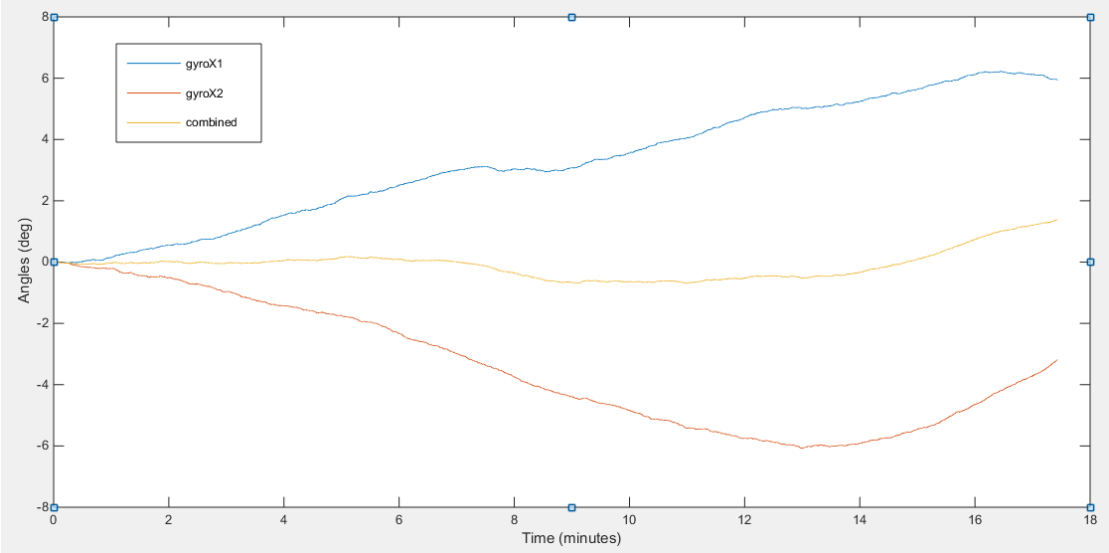

Figure 2.14: Gyroscope drift from two IMUs with opposed sense axes

2.3 Sensor Fusion

Sensor fusion is a process by which data from several different sensors are "fused" to compute something more than could be determined by any one sensor alone. For our application it means we need to fuse data from multiple inertial sensors to help us determine the orientation in 3D space. We use a quaternion based complementary filter scheme to achieve this end. The reason for using quaternions is to avoid the use of additional function in the code to deal with Euler angles and to avoid gimbal lock. Also complementary filter is not computationally expensive compared to stochastic algorithms like Kalman Filter. Though it must be admitted that with a more intricately crafted sensor fusion scheme the attitude estimation performance of the system could be greatly improved (Paina, Gaydou et al. 2011) by virtue of improved bias estimation.

2.3.1 Representing Angles

Depiction of orientation of a rigid body can be done in various forms: axis-angle, Euler angles, quaternions, etc. In this section we explore the problem of mathematically representing the orientation of a rigid body using inertial sensors.

EULER ANGLES

Euler angles are the most widely used representation technique which is both simple to use and intuitive to understand. The foundation of this technique is the premise that any orientation can be dissected and represented as a combination of three rotations about the orthogonal body reference frame of the object. These three rotations though have to vector added in a particular order for universal order as angular rotations are not commutative.

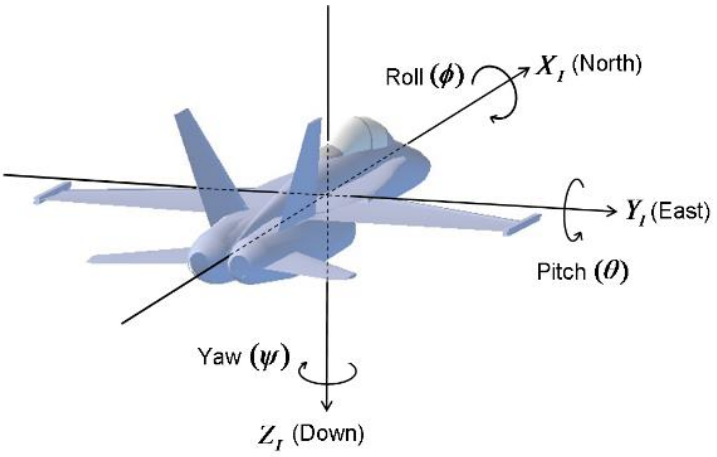

Figure 2.15: Euler angle representation (CH_Robotics)

There are two problems with using Euler angle representation:

1. Computationally expensive: Calculation of trigonometric functions in embedded processors takes a longer amount time than simple floating point math.
2. Gimbal Lock: This is the phenomena when the orientation of a body cannot be unique determined using a particular sequence of Euler Angles. This happens usually when the pitch appears 90^0 as can be seen when we substitute $\boldsymbol{\Theta}$ in equation 2. with 90^0.

MEASURING ATITTUDE USING ACCELEROMETERS

The measured specific force of accelerometer **a** can be represented in vector form as follows:

$$\overline{\boldsymbol{a^b}} = \overline{\boldsymbol{\Omega^b}}\, \boldsymbol{X}\, \overline{\boldsymbol{V^b}} - \overline{\boldsymbol{g^b}} = \overline{\boldsymbol{\Omega^b}}\, \boldsymbol{X}\, \overline{\boldsymbol{V^b}} - \boldsymbol{g} \begin{bmatrix} -\boldsymbol{sin}\Theta \\ \boldsymbol{sin\varphi\ cos}\Theta \\ \boldsymbol{cos\varphi\ sin}\Theta \end{bmatrix} \qquad \textbf{(2.11)}$$

where **φ** and **Θ** represent roll and pitch respectively; **b** superscript represents the body frame; **V** represents translational acceleration; $\boldsymbol{\Omega}$ **X V** represents angular acceleration; and **g** is gravity. If the body is at rest V=0 and if rotational acceleration is neglected, we have:

$$\overline{\boldsymbol{a^b}} = -\boldsymbol{g}\begin{bmatrix} -\boldsymbol{sin}\Theta \\ \boldsymbol{sin\varphi\ cos}\Theta \\ \boldsymbol{cos\varphi\ sin}\Theta \end{bmatrix} \quad \textbf{(2.12)}$$

On further calculations (Pedley 2013) we arrive at:

$$\boldsymbol{tan\varphi} = \boldsymbol{atan2}(\boldsymbol{a_y^b}, \boldsymbol{a_z^b}) \quad \textbf{(2.13)}$$

$$\boldsymbol{tan}\Theta = \boldsymbol{atan2}(-\boldsymbol{a_x^b}, \sqrt{\boldsymbol{a_y^2} + \boldsymbol{a_z^2}}) \quad \textbf{(2.14)}$$

From equation 2.13 we get the roll and equation 2.14 we get the yaw.

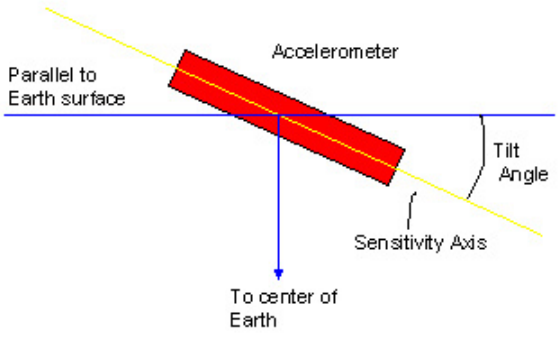

Figure 2.16: Measuring tilt using accelerometers (Innoventions)

MEASURING ATTITUDE USING GYROSCOPES

The measured angular rate $\boldsymbol{\Omega}$ in vector form can be represented as:

$$\boldsymbol{\Omega} = \begin{bmatrix} \boldsymbol{p} \\ \boldsymbol{q} \\ \boldsymbol{r} \end{bmatrix} \quad \textbf{(2.15)}$$

By using rotation matrices, the Euler angles can then be calculated using the following formula:

$$\begin{pmatrix} \dot{\varphi} \\ \dot{\Theta} \\ \dot{\Psi} \end{pmatrix} = \begin{pmatrix} p + qsin(\varphi)\tan(\Theta) + rcos(\varphi)\tan(\Theta) \\ qcos(\varphi) - rsin(\varphi) \\ \frac{qsin(\varphi)}{\cos(\Theta)} + rcos(\varphi)/\cos(\Theta) \end{pmatrix} \quad \textbf{(2.16)}$$

Where, **p** is the x axis gyro output, **q** is the y axis gyro output and **r** is the z axis gyro output; in body frame of reference; **φ** is roll, **Θ** is pitch and **Ψ** is yaw.

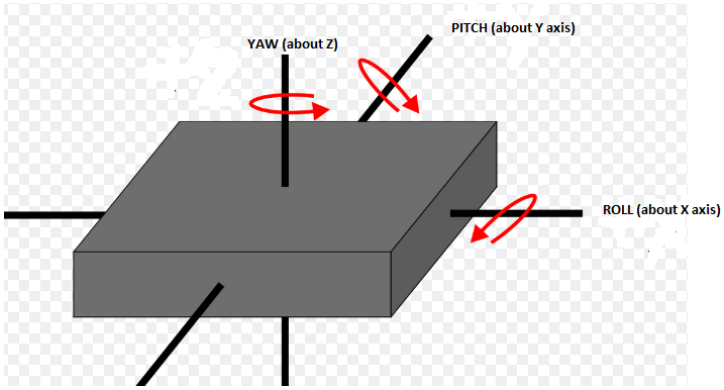

Figure 2.17: Measuring angles using gyroscopes

QUATERNIONS

As we have seen, Euler angles have a couple of drawbacks. In order to overcome them quaternions are used. This representation uses four parameters and is not as intuitive as Euler angles:

$$\bar{q} = q_0 + iq_1 + jq_2 + kq_3 \quad \textbf{(2.)}$$

where the parameters should satisfy the following normalization condition:

$$norm(\bar{q}) = \sqrt{q_0^2 + q_1^2 + q_2^2 + q_3^2} = 1 \quad \textbf{(2.17)}$$

The representation is for the axis about which rotation takes place and the angle by which it is rotated. The conversion between Euler angle representation and quaternions can be written as:

$$\boldsymbol{q_0 = cos\frac{\theta}{2}}$$

$$\boldsymbol{q_1 = -r_x sin\frac{\theta}{2}}$$

$$\boldsymbol{q_0 = -r_y sin\frac{\theta}{2}}$$

$$\boldsymbol{q_0 = -r_z sin\frac{\theta}{2}}$$

where $\boldsymbol{r_x}$, $\boldsymbol{r_x}$ *and* $\boldsymbol{r_x}$ are the components of the unit vector $\bar{\boldsymbol{r}}$ in the frame of rotation.

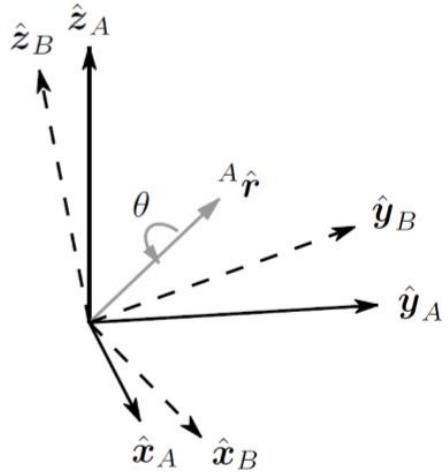

Figure 2.18: Euler to quaternion conversion

The most important operation on quaternions is calculating the product:

$$\overline{\boldsymbol{q_C^A}} = \overline{\boldsymbol{q_C^B}} \otimes \overline{\boldsymbol{q_B^A}} \qquad \textbf{(2.18)}$$

where $\boldsymbol{q_C^A}$ is the rotation to C with respect to A; $\boldsymbol{q_B^A}$ is the rotation to B with respect to A; and $\boldsymbol{q_C^B}$ is the rotation to C with respect to B. Hence we have the following resultant matrix that uniquely represents the manipulation:

$$\overline{\boldsymbol{q_C^A}} = \begin{bmatrix} \boldsymbol{a_0\, b_0 - a_1\, b_1 - a_2\, b_2 - a_3\, b_3} \\ \boldsymbol{a_0\, b_1 + a_1\, b_0 + a_2\, b_3 - a_3\, b_2} \\ \boldsymbol{a_0\, b_2 - a_1\, b_3 + a_2\, b_0 + a_3\, b_1} \\ \boldsymbol{a_0\, b_3 + a_1\, b_2 - a_2\, b_1 + a_3\, b_0} \end{bmatrix} \quad \textbf{(2.19)}$$

where $\overline{\boldsymbol{q_C^B}} = [\boldsymbol{a_0\ a_1\ \ a_2\ \ a_3}\ ]$ and $\overline{\boldsymbol{q_C^A}} = [\boldsymbol{b_0\ b_1\ \ b_2\ \ b_3}\ ]$ are the respective quaternions.

2.3.2 Complementary Filter

There are many sensor fusion algorithms that give good attitude estimation. Extended Kalman Filter is most commonly used stochastic estimator. But to give accurate estimated the modelling of measurement and update matrices is very important. This leads to increased complexity which might not be required for some applications. Notwithstanding this, EKF is still the standard algorithm used for inertial navigation purposes (Quoc, Sun et al. 2015). Hence the use of complementary filters makes more sense in such situations.

Complementary filters can be used with a group of sensors having complementary signal characteristics. Accelerometers are susceptible to high frequency noise and gyroscopes are susceptible to low frequency noise, hence complementary filter can be used to appropriately blend both the sensor attitude (figure 2.19) updates to arrive at a superior reading without the use of a stochastic estimator algorithm like Kalman filter.

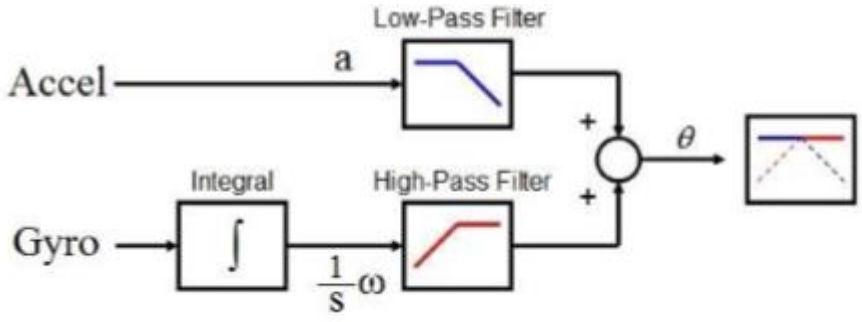

Figure 2.19: Complementary filter structure

This figure demonstrates a 1D complementary filter. Mathematically, this can be represented by the following transfer function:

$$\theta = \frac{1}{1+Ts}\boldsymbol{a} + \frac{Ts}{1+Ts}\frac{1}{s}\boldsymbol{g} = \frac{a+Tg}{1+Ts} \quad \textbf{(2.20)}$$

where θ is the final fused angle, **a** is the angle calculated by accelerometer, **g** is the angular rate calculated by the gyroscope, and **T** is the "time-constant". This leads to fusing low-frequency estimate from the accelerometer and high frequency estimate from the gyroscope. The final recursive equation can hence be written as:

$$\theta_i = \boldsymbol{\alpha}\theta_{i-1} + (1-\boldsymbol{\alpha})\boldsymbol{a_i} + \boldsymbol{\alpha} g_i dt \quad \textbf{(2.21)}$$

where **i** is the present time-step, **dt** is the sampling time, **α** is the cutoff parameter such that $\boldsymbol{\alpha} = \frac{T}{T+dt}$ more frequently calculated by trial and error.

2.3.3 Sensor Fusion Scheme

The sensor fusion uses complementary filter explained above. But before that the following steps are taken to ensure accurate data. The filter parameters need to be tweaked according

to the sensor under consideration as there is wide variation in performance in low-cost sensors.

Calibration

In order to have good data calibrating the sensors is very important. In section 2.2, the methodology and the error model has been explained in detail. It entails, removing the bias offset first as it is the leading cause of huge errors. It is pretty easy to remove by averaging when the senor is still.

Centralized data fusion

The raw data from the dual IMU system is fused together to take advantage of the common mode effect as described previously. The following equations explains the process:

$$\boldsymbol{G = \frac{G_1 - G_2}{2}} \quad \textbf{(2.22)}$$

where $\boldsymbol{G_1}$ and $\boldsymbol{G_2}$ are the values of inertial quantities of sensor 1 and 2 respectively;

$$\boldsymbol{G_i = g_i + b_i + n_i} \quad \textbf{(2.23)}$$

Where **i=1,2** are for the sensors; **g** is the actual inertial quantity; **b** is the bias; and **n** is the noise.

On combining data, this is what we get:

$$\boldsymbol{G = \frac{1}{2}(g_1 + b_1 + n_1) - \frac{1}{2}(-g_2 - b_2 + n_2)} \quad \textbf{(2.24)}$$

where we note that the inertial quantity measured by the second sensor is negative of the first sensor i.e. $\boldsymbol{g_1 = g_2 = g}$. The trend in bias is opposite though not the same and the

noise part is random in nature, though as we have seen in section 2.2 there is averaging effect due to this configuration- i.e. the combined noise of the system is $\frac{n_1+n_2}{2}$.

Therefore, finally we have:

$$\boldsymbol{G = g + kb + pn} \quad \textbf{(2.25)}$$

where **k** and **p** depend on the values of changing bias and noise but less than 1.

Filtering

The gyro data was band pass filtered to remove high frequency disturbances and the accelerometer data was low pass filtered to remove high frequency noise.

Gravity Effect

The accelerometer is sensitive to the effect of gravity which makes it difficult to get actual sensor accelerations along the axis aligned with gravity. In order to take care of it we need to remove the gravity effect by turning the sensor frame to global frame. This need not be performed if the application does not allow the sensor to be flipped.

The following equations gives an idea of the process:

$$\boldsymbol{a^G = A^G - \begin{bmatrix} 0 \\ 0 \\ 9.81 \end{bmatrix}} \quad \textbf{(2.26)}$$

where $\boldsymbol{a^G}$ is the final acceleration in global frame; $\boldsymbol{A^G}$ is the transformed acceleration; and assuming gravity is constant at 9.81m/s^2.

$\boldsymbol{A^G}$ is given by the following equation:

$$\boldsymbol{A^G = R_S^G * A^s} \quad \textbf{(2.27)}$$

where $\boldsymbol{A^s}$ is the measured acceleration in sensor frame and $\boldsymbol{R_s^G}$ is the rotation matrix from sensor to global frame.

Thresholding

Now that the sensor noise has been reduced a lot, we apply a threshold filter to remove any residual noise from the filtered data. This has the effect of removing any time varying bias/ noise from the readings. This though leads to reduction in the bandwidth of the sensor giving rise to problem of not detecting very slow motions like 0.5 deg/s. But for most applications this could be neglected.

2.4 Hardware Design

The overarching goal of the hardware design is to have a compact low-cost IMU that can efficiently run the smart- algorithm. The yIMU consists of two MPU6050 IMUs with in-built temperature sensor. The design was minimalist keeping in mind that this is not a production version. The design went through many prototyping cycles. The hardware characteristics of final prototype is described in Table 2.1. This has a stacked shield layout, which was used in the development of the calibration procedure and tracking algorithm. The boards were fabricated in-house at ASU polytechnic electronics lab.

Physical Characteristics	
Dimensions	62x65x42 mm
Weight	107 g with case
Sensor Specifications	MPU 6050
Accelerometer	
Range	±2g
Resolution	3.9mg/LSB
0g Bias Level	±40 mg (X,Y); ±80 mg (Z)
Noise Performance	<3.9 mg RMS
Gyroscope	
Range	±250 dps
Resolution	0.0696 dps/LSB
0g Bias Level	±40 dps
Noise Performance	0.38 dps RMS
Temperature	
Sensor operation range	-40^0 C to 80^0 C
Temp compensation range	5^0C to 55 ^{0}C
Microcontroller Specifications	
	Arduino pro mini
	ATmega 328p

	16 MHz clock frequency	
Connectivity		
Bluetooth	HC-06 class II with 10 m range	
USB	FTDI	
Power Specifications		
	Li-ion battery	
	800mAh	
	3.7 V	

Table 2.1: Hardware specification of yIMU v1.4

2.4.1 System Design

yIMU v1.4 is the testing version which has two boards stacked on top of each other. The base board houses the charging circuit and the Arduino pro-mini microcontroller board along with a power switch. The charging is done via a micro-USB whereas the programming is done via an FTDI cable. The board is also connected to a Li-ion battery that powers the entire setup.

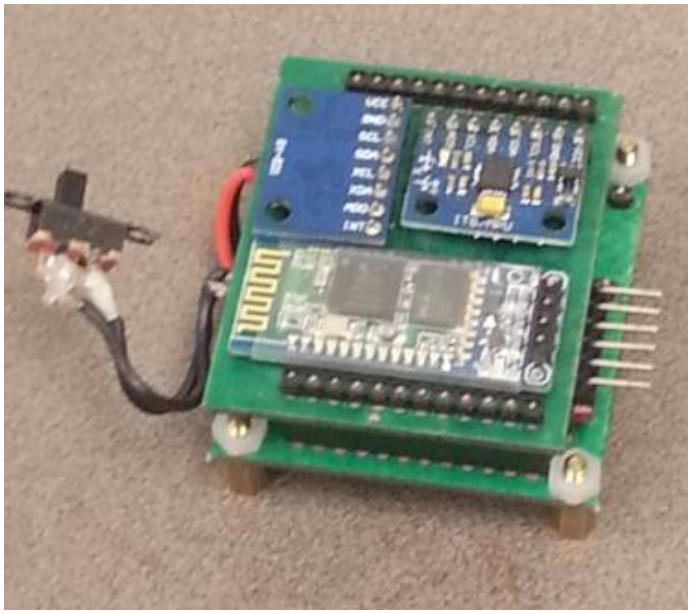

Figure 2.20: The stacked boards in yIMU v1.4

The top board houses two MPU6050 IMUs with their sense axes in opposing directions. The x and y axes have been flipped in the algorithm (Figure) to account for the impossibility to physically place the corresponding axes opposing each other. As those axes were manufactured in-plane during fabrication there should be no loss in accuracy. An HC-06 Bluetooth module is packed aside the sensors as shown for wireless connectivity.

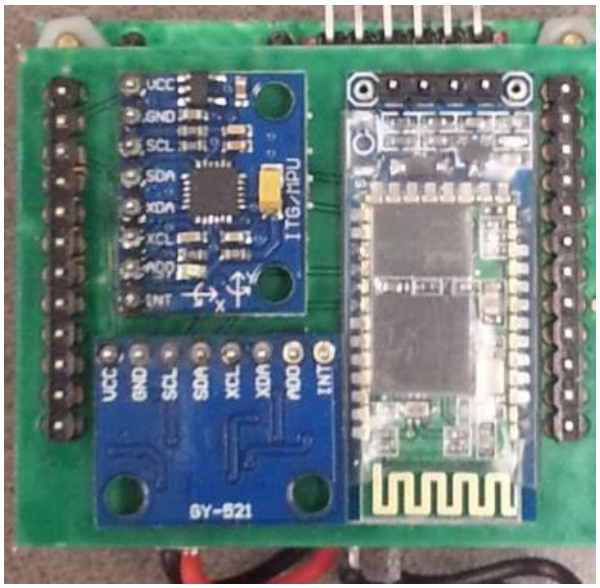

Figure 2.21: Sense axes of the dual IMU system

It is to be noted that the size of the board can be reduced further by increasing the layers in the board. This is beyond the capabilities of our in-house fabrication facility and also would increase the cost of the prototype, hence it has not been physically realized though there is definitely scope for further improvements in the design. We used I2C mode of serial communication between the sensors and the microcontroller which allows sensor registers to be read upto a maximum of 400kHz. Though this is much slower than SPI (which could in theory allow upto 20MHz in communication speed), we would not have to deal with high frequency signal errors arising from its use and to accommodate for it in our circuit design.

2.4.2 Enclosure Design

The enclosure was 3D printed using FDM (Fused Deposition Modelling) method in lab. The major concern with enclosure design was to be able to house all the required circuitry

with proper alignment within the housing. Adequate care was taken during the design of the enclosure to address this issue. Another problem was to ensure that the IMU enclosure to remains fixed firmly to the body to prevent unnecessary movements. To solve this a simple Velcro strap with padding was used.

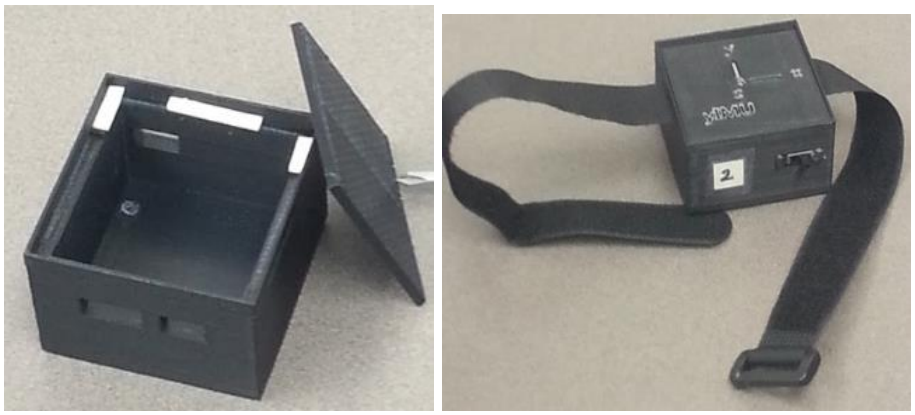

Figure 2.22: Enclosure for yIMU v1.4 with straps

2.5 Performance Evaluation

In this section we test to check for improvements in sensor parameters due to yIMU configuration. We also discuss the experimental results of the implementation of the algorithm.

2.5.1 Testing Viability of Common Mode Effect

As discussed in section 2.2.1 environmental effects are felt more severely in low cost IMUs than navigation grade IMUs by virtue of their inherent working principle and nature of manufacturing process. In this section we note the effect of temperature and vibration on yIMU systems. It is to be noted that these effects are dependent on the product model of sensor tested (MPU6050) and do not hold true for all IMUs. The exact values of the effect changes from sensor to sensor but these results point towards the prevalent trends in the environmental effects on yIMU.

TEMPERATURE EFFECT

Procedure: The yIMU system is kept flat and stationary, and data is logged for 5 minutes at room temperature. Then it is heated using a heat gun for 5 mins till around 50^0 C. Then it is allowed to cool to room temperature. Raw accelerometer and gyroscope data is collected for further analysis.

Figure 2.23: Heraeus UT12p Thermal Chamber

Results: Figure 2.24 shows the temperature profile followed for the experiment. This representative temperature is from the sensor at IMU1. Then a linear fit for the scatter plot data from IMU1, IMU2 and the yIMU system is calculated using MATLAB as depicted in Figure 2.25. The data for each of the axes is documented in Table 2.2. Compare the temperature drift trend and extent of effect for each of the axes.

Figure 2.26 compares the angular rate output temporal trend. The pattern is similar for all the axes.

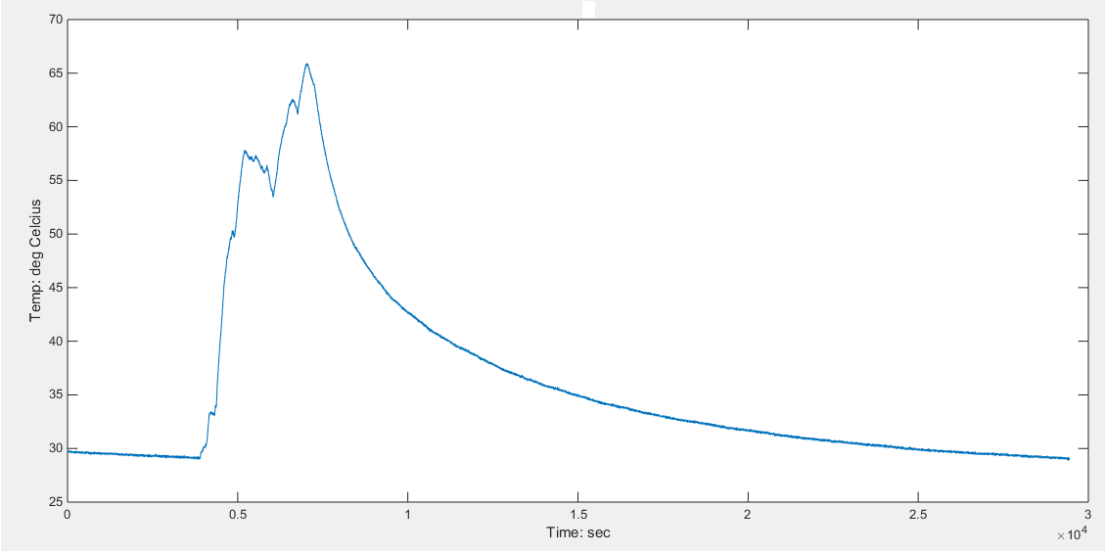

Figure 2.24: Temperature profile of the experiment

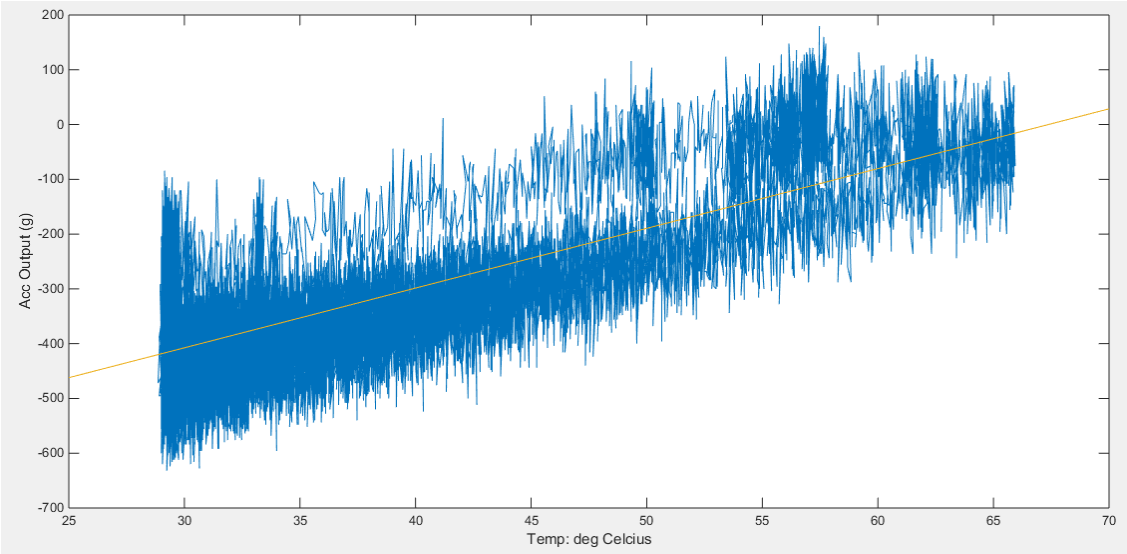

Figure 2.25: Sample scatter plot of acc axis X for IMU1: the yellow line is the linear fit for the data

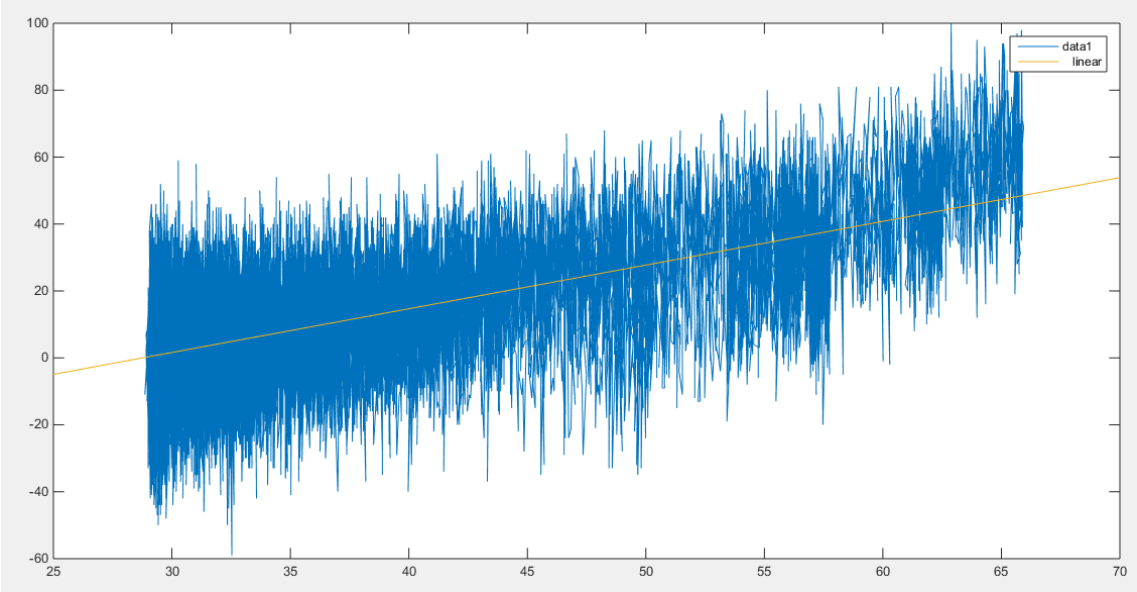

Figure 2.26: Sample scatter plot of gyro axis X for IMU2: the yellow line is the linear fit for the data

NAME	Acc- SLOPE (LSB/^{0}C)	Acc-INTERCEPT (LSB)	Gyro-SLOPE (LSB/^{0}C)	Gyro-INTERCPT (LSB)
IMU1-X	10.906	-734.75	-5.0286	162.08
IMU1-Y	-9.1273	696.33	10.55	-360.99
IMU1-Z	-7.2778	16847	2.3697	-85.397
IMU2-X	-9.2803	-504.68	1.3062	-37.572
IMU2-Y	1.0003	-252.34	-1.4636	+56.49
IMU2-Z	2.8734	16283	-0.44031	+16.915

Table 2.2: The results of linear best fit between sensor output and temperature for MPU6050 in opposing configuration

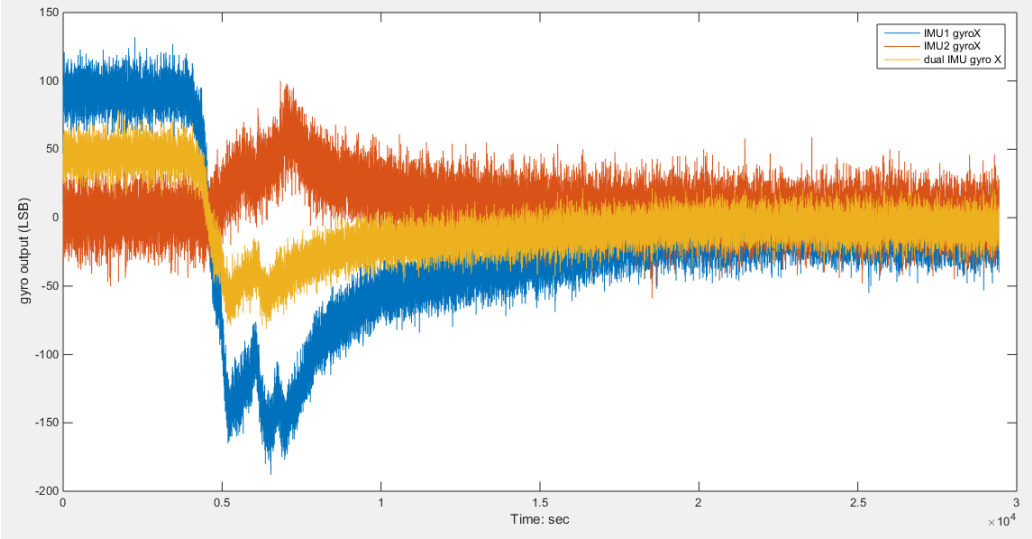

Figure 2.27: Comparison of temperature effect trends for gyro X of IMU1, IMU2 and combined output

VIBRATION EFFECT

Procedure: IMU is placed flat z axis up on a surface at rest for a minute, followed by vibration for 20 s. The setup was vibrated at 60 Hz using a shaker. The raw accelerometer and gyroscope outputs are recorded after correcting for offset bias. The temperature of the setup was checked to be constant.

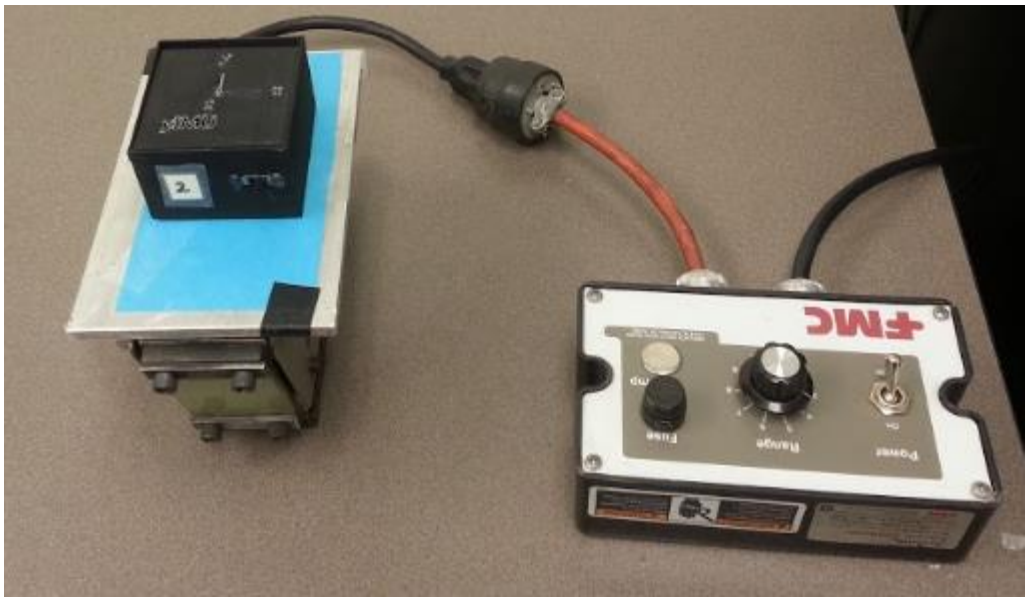

Figure 2.28: The FMC shaker used for vibration testing

Results: The following are the results for testing done on yIMUs. A moving average filter was used to filter the raw data in MATLAB. Some questions to ponder over:

1. What is the effect of vibration on accelerometer and gyroscope?
2. What are the trends for the opposing axes?

We can see the trend from the figure 2.29 which says that opposing sense axes do reduce the vibration effect. They obviously do not cancel each other out, but the characteristics are good enough. For yIMU data point to the fact that for MPU6050 this arrangement does reduce effect of vibration. But dynamic vibration tests need to be done to ascertain its applicability in highly agile field situations.

Answers:

1. Firstly, looking at the effect on accelerometers of IMU1 we can see in figure 2.29 that there is no significant effect on bias drift after vibration (at 60 Hz). Also there

is no pronounced vibration along Z axis. In the case of gyroscopes however, we can see that the axes perpendicular to the vibration axis show pronounced disturbance compared to the Z axis gyro. This is to be expected as the proof mass of gyroscope is designed to measure the angular rate not displacement. The effects are similar for IMU2

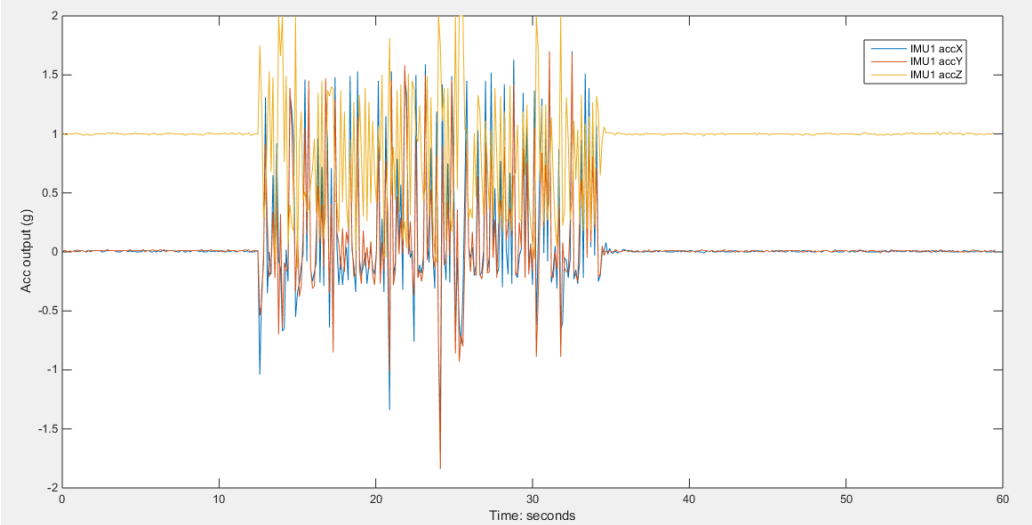

Figure 2.29: Effect of vibration on IMU1 accelerometers

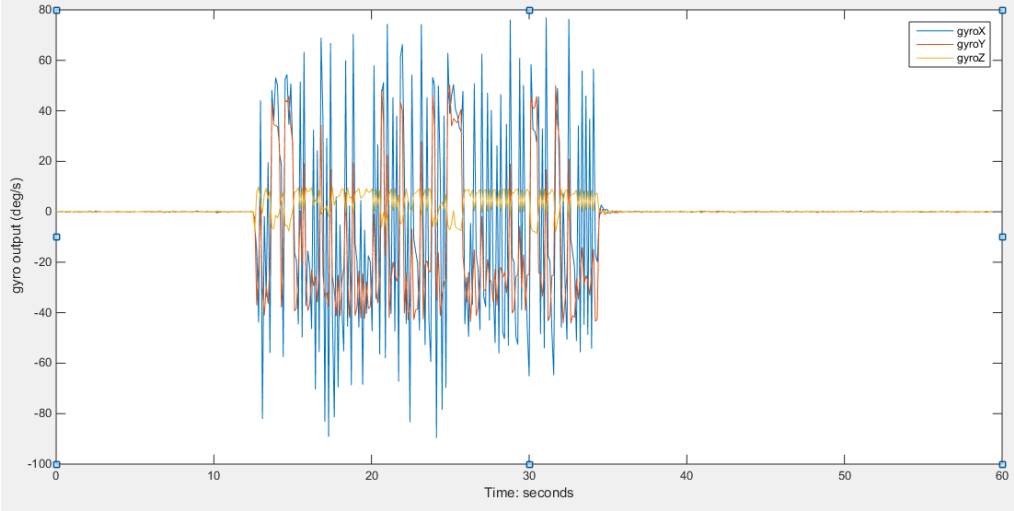

Figure 2.30: Effect of vibration on IMU1 gyroscopes

2. We can see from the figures below that for the vibrating axes, opposing axis obviously have approximately opposing trends during the vibration phase. Hence, combining their outputs leads to partial vibration cancellation. For the cross axes though the cancellation is not significant as seen in figure 2.31.

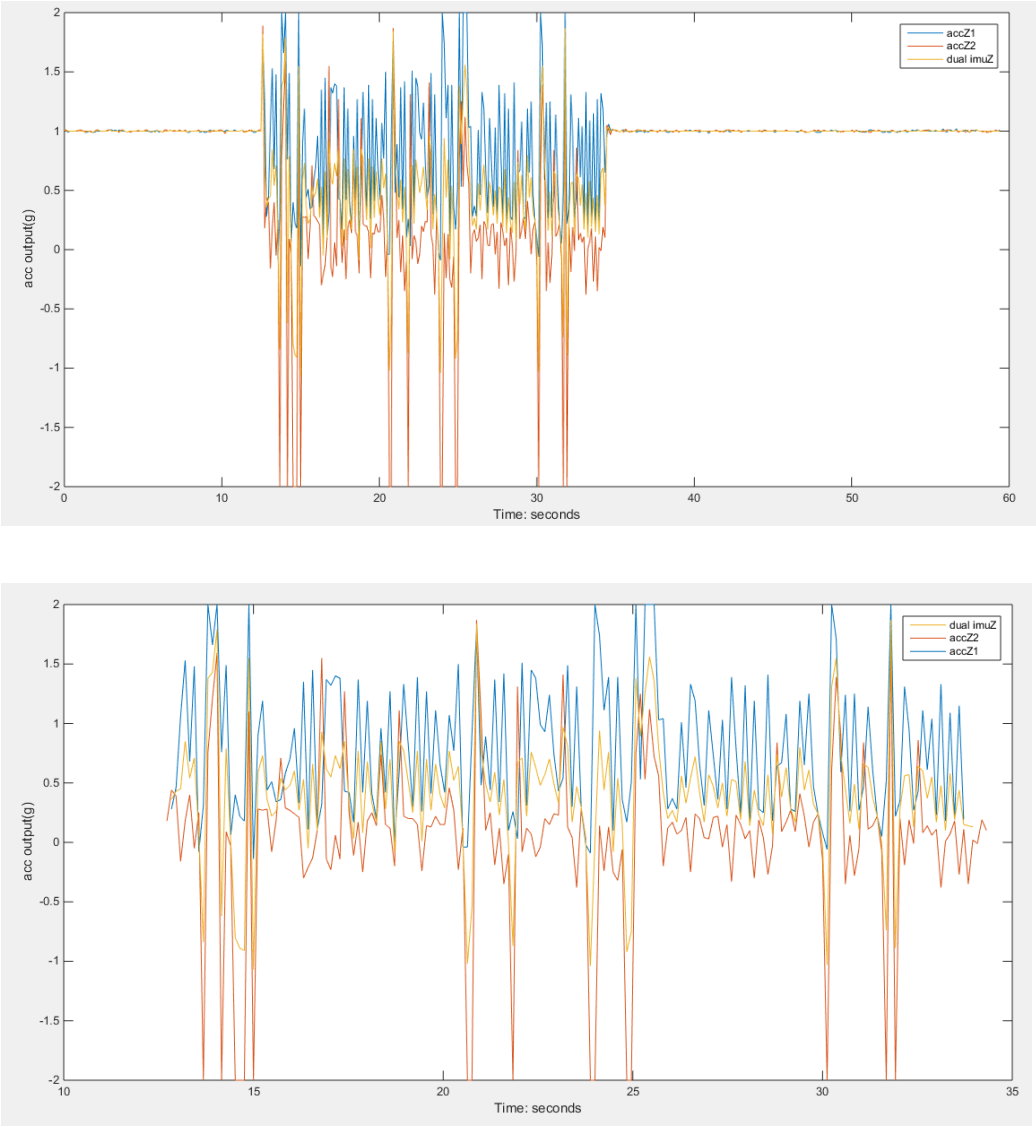

Figure 2.31: Effect of vibration on vibration axis (Z axis): (above) The whole duration; (below) For the duration of vibration

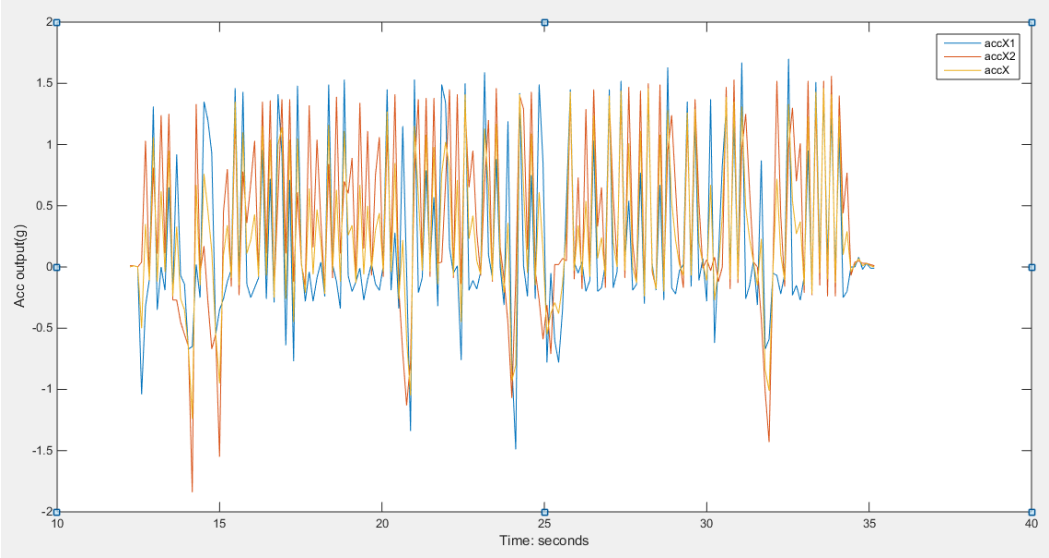

Figure 2.32: Effect of vibration on cross axis (X axis): For the duration of vibration

BIAS ERROR

Bias error refers to deterministic error due to static bias offset here. If this is unaccounted for it could be the largest source of integration error in inertial navigation. Hence we compare the bias error of a single IMU to the yIMU to get an idea of improvement in bias performance. For details of random bias component see section 2.5.5.

Procedure: Mean of around 5 minutes of static data was collected for each of the axes of IMY-1 and yIMU.

Result: There is noticeable reduction in the bias error in yIMU compared to IMU-1.

	IMU-1 Accelerometer (mg)	**yIMU- Accelerometer (mg)**
X	0.2110	0.0998
Y	-1.1895	-0.2325
Z	101.4821	1.6910

Table 2.3: Accelerometer bias error

	IMU-1 Gyroscope (deg/s)	yIMU- Gyroscope (deg/s)
X	0.0264	0.0196
Y	-0.1488	-0.0666
Z	12.6922	6.3358

Table 2.4: Gyro bias error

2.5.2 AV Results

Procedure: The static bias and misalignment errors can be removed by averaging the data and subtracting the offset. Hence we can see that the remainder of the errors in the readings have measurement noise and drifting bias as their source. This data can now be analyzed using Allan variance analysis. We have used MATLAB to generate Allan deviation plots.

Results:

In order to analyze the AV plots we need look at the following four points on the graph:

1. *Point A*: This is the starting point of the graph that represents standard deviation of noise for any one single measurement point. This gives us an idea of how noisy a single measurement can be, it is to be noted that this mentions the probability of noisy measurements not the certainty of it. For example, if point A measures 0.07 g (for figure 2.34) then 1 standard deviation of the measurements have error of 0.07g in the measurement and rest will have errors greater than that.
2. *Slope A*: This is the slope for the first part of the AV graph before the dip. This part is used to analyze the measurement noise, that depends on the influence of high frequency errors. For example case, in figure 2.34, slope A is -0.483754 that means it is close to the white noise slope of -0.5, hence we can say that the measurement errors are predominantly white in color.

3. *Point B*: Represents the bias stability of the sensor. It gives you the lowest possible value of bias error generated in a sensor. The lower the value, the better sensor it is. In figure 2.34, the bias stability of accelerometer X axis this particular MPU6050 is 0.0057 g.
4. *Slope B*: This is the slope for the second part of the AV graph, after the dip. This part is used to analyze the random walk errors, that depends on the influence of low frequency errors. We see that the slope B for figure 2.34 is 0.313607, meaning it is close to random walk slope of +0.5.

ACCELEROMETER PERFORMANCE

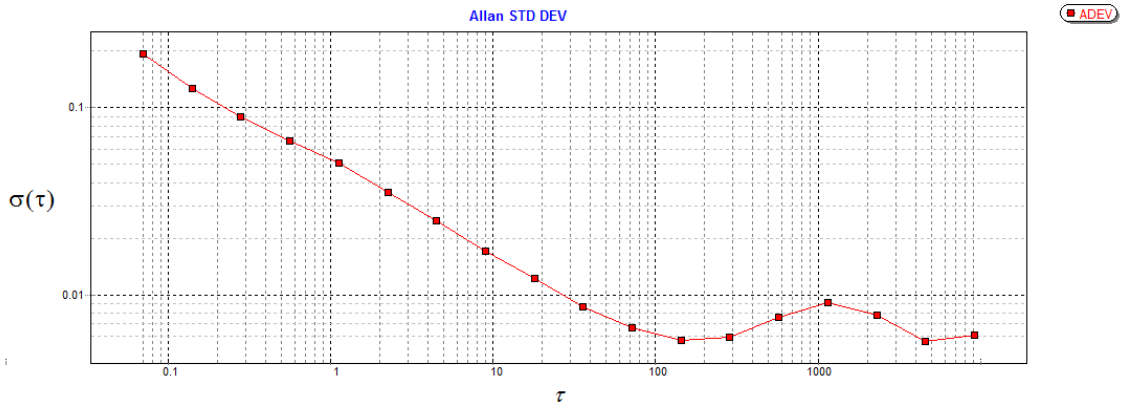

Figure 2.34: Allan Deviation plot for IMU-1 accelerometer X

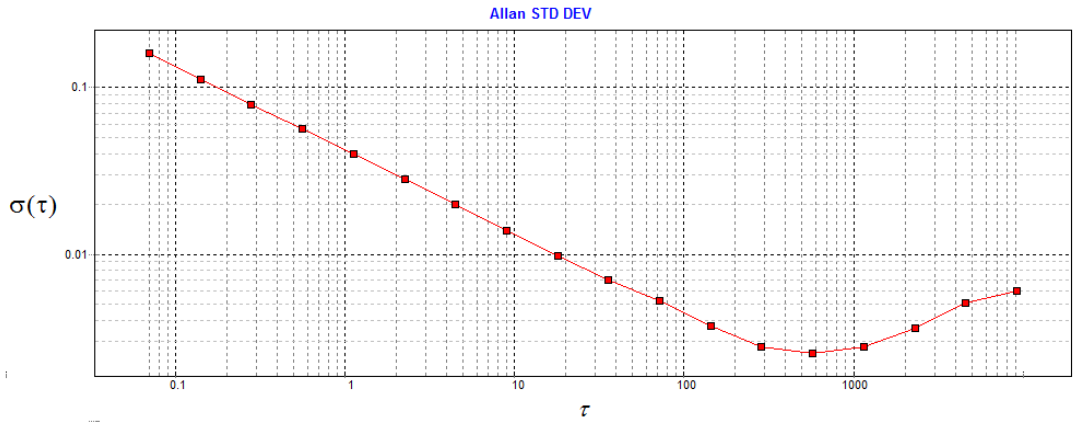

Figure 2.35: Allan Deviation plot for yIMU accelerometer X

	POINT A (g)	SLOPE A	POINT B (g)	SLOPE B
IMU-1 X	0.07	-0.483754	0.0057	0.313607
IMU-1 Y	0.07	-0.519263	0.0035	0.149470
IMU-1 Z	0.07	-0.464424	0.00480	0.280849
yIMU X	0.07	-0.490277	0.0026	0.383257
yIMU Y	0.07	-0.495157	0.0018	0.421459
yIMU Z	0.07	-0.485253	0.0025	0.564556

Table 2.5: Comparing the results of AV analysis between IMU-1 and yIMU accelerometers

GYROSCOPE PERFORMANCE

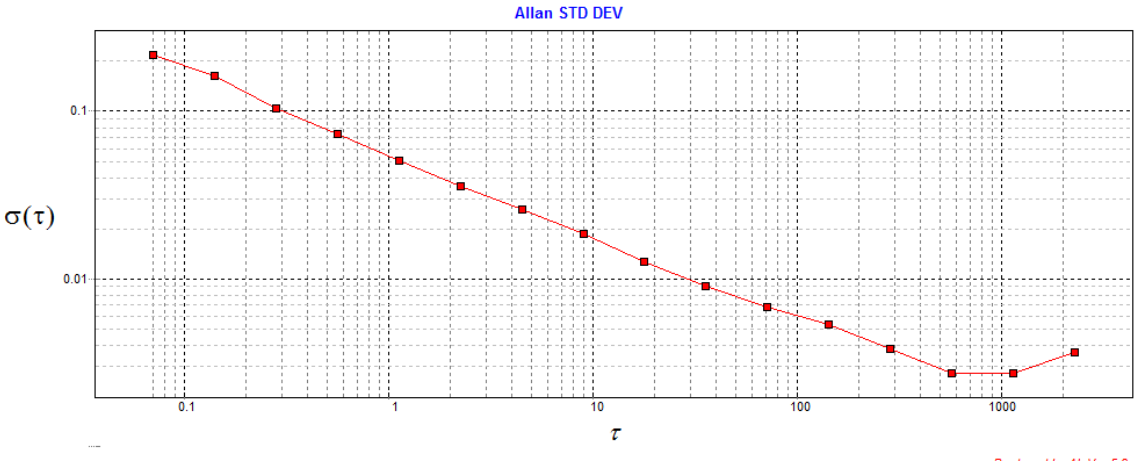

Figure 2.36: Allan Deviation plot for IMU-1 gyroscope X

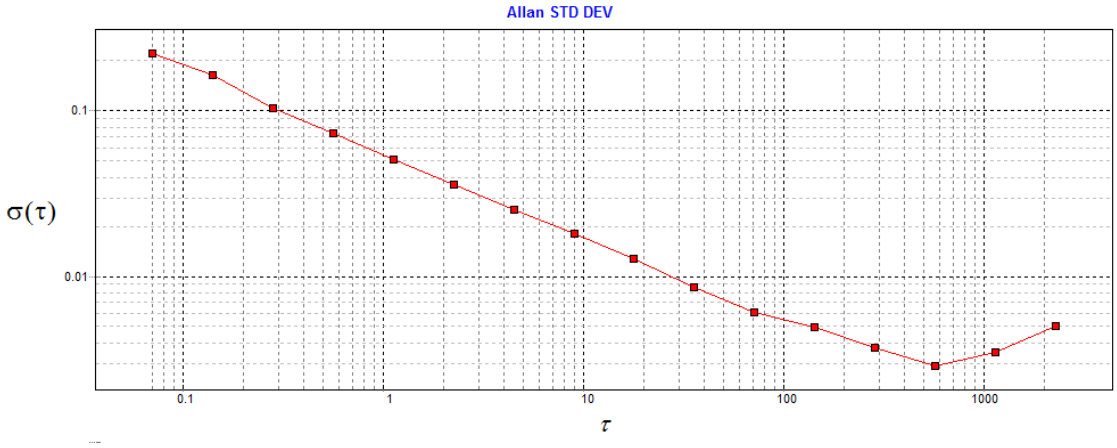

Figure 2.37: Allan Deviation plot for yIMU gyroscope X

	POINT A (deg/s)	**SLOPE A**	**POINT B** (deg/s)	**SLOPE B**
IMU-1 X	0.07	-0.51176	0.0053	-0.40475
IMU-1 Y	0.07	-0.522333	0.0042	-0.40306
IMU-1 Z	0.07	-0.527713	0.0026	0.28838
yIMU X	0.07	-0.519355	0.0029	0.484973
yIMU Y	0.07	-0.505054	0.0025	-
yIMU Z	0.07	-0.514046	0.0023	0.476239

Table 2.6: Comparing the results of AV analysis between IMU-1 and yIMU gyroscopes

The following are the results from the AV plots shown above:

1. The remainder of the AV plots are in appendix B. we note that point A is the same for both IMU-1 and yIMU. This should be expected as this point negates the effect of combining data from two IMUs. This shows the noise content of a single measurement sample; hence the effect of averaging is negated.
2. Comparing the slopes, we see that the measurement noise for yIMU is more close to -0.5 slope than IMU-1, this means that the white noise modelling of measurement noise approximates the behavior of yIMU better.

3. Point B is the bias stability of the system. Obviously we see big improvement in the bias stability values of accelerometer as seen.
4. Slope B is the nature of low frequency errors. We see that the slope is close to errors that are random in nature.

CONCLUSION

The initial part of the plots, display effect of measurement noise and the later part the effect of drifting bias. By visual inspection we can see that the slope of the initial part is close to $-\frac{1}{2}$ and the later part the slope is close to $+\frac{1}{2}$, meaning that measurement noise can be said to be predominantly white in color and drifting bias is random in nature (Brownian motion). In order to confirm this, we can see that in tables 2.5 and 2.6 we have the slopes of the functions. It confirms our prediction about the nature of measurement noise. In addition, we can see the improvements in the data.

2.5.3 PSD Results

Procedure: The static raw data from yIMU is collected and the static bias is removed via subtracting the mean from each reading for all axis. Using Alavar 5.2 PSD is calculated for the data. The slope of the curve is analyzed to draw conclusions.

Result:

Figures 2.38 and 2.39 detail the PSDs for IMU-1 and yIMU. It is to be noted that the effect of measurement noise is felt high at higher frequencies and the effect of drifting bias predominates at the lower frequencies. Hence if the PSDs are flat at higher frequencies we can say that the measurement noise is white in color.

From the figures we can say that for frequencies above 1Hz the PSD is pretty flat, as also confirmed by calculating the slopes. For figure 2.38 the slope was S(f)=f^(-0.35).

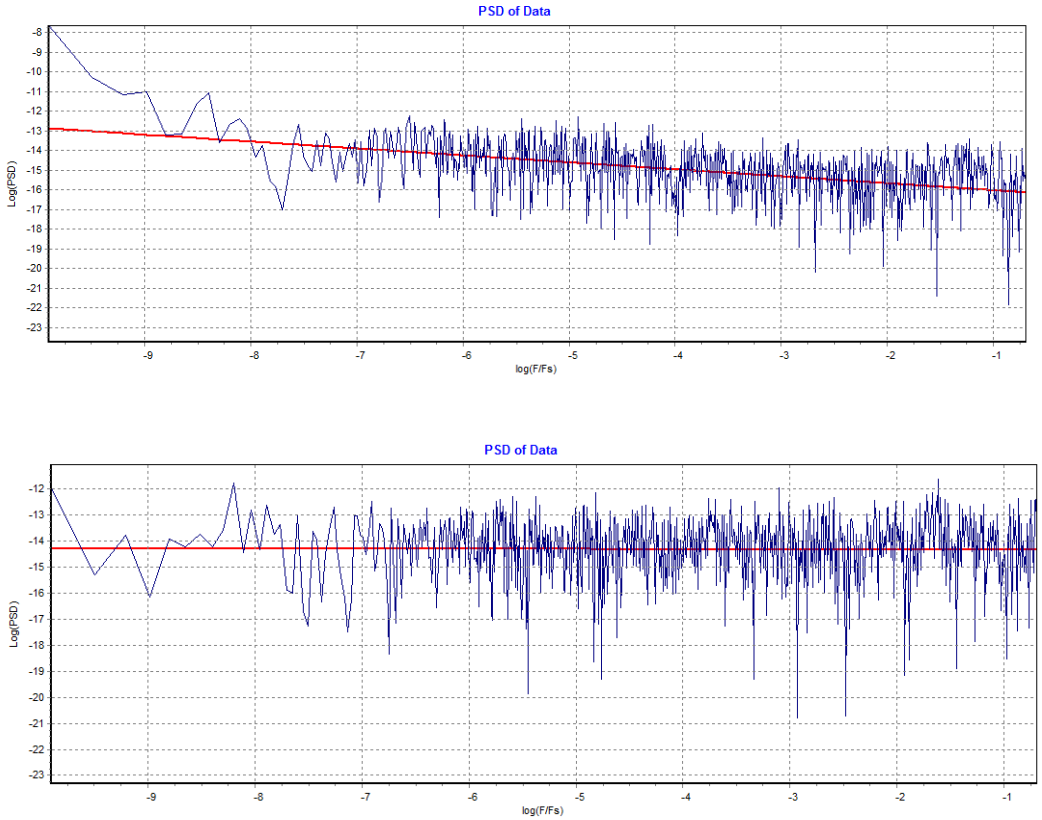

Figure 2.38: PSDs for IMU-1: (above) accelerometer (below) gyroscope for X axis

NAME	PSD SLOPE
accX	-0.35
accY	-0.052
accZ	-0.33
gyroX	-0.018
gyroY	-0.03
gyroZ	0.032

Table 2.7: PSD slope values for IMU-1

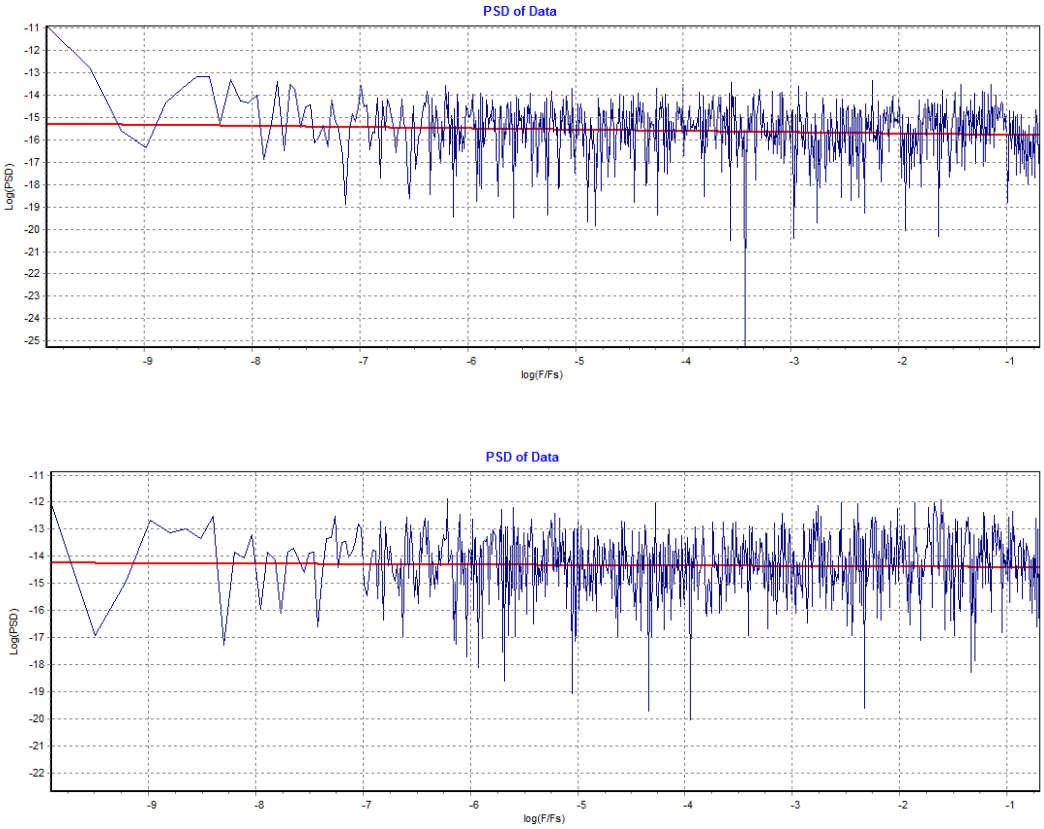

Figure 2.39: PSDs for yIMU: (above) accelerometer (below) gyroscope for X axis

NAME	PSD SLOPE
accX	-0.058
accY	-0.038
accZ	-0.062
gyroX	0.007
gyroY	0.0018
gyroZ	-0.012

Table 2.8: PSD slope values for yIMU

2.5.4 PDF Results

Procedure: The static raw data from yIMU is collected and the static bias is removed via subtracting the mean from each reading for all axis. Using MATLAB the noise data is

plotted as histogram to show the number of occurrences per value. Then a normal distribution over the sample time is also plotted over the same histogram to see the fit.

Result: The confirmation of Gaussian distribution is done visually by noticing the match between the histograms and the Gaussian curve. From figure 2.40 we can conclude that we can indeed use Gaussian distribution to model measurement noise of MPU6050. Table 2.9 shows the sample variances of the IMU-1.

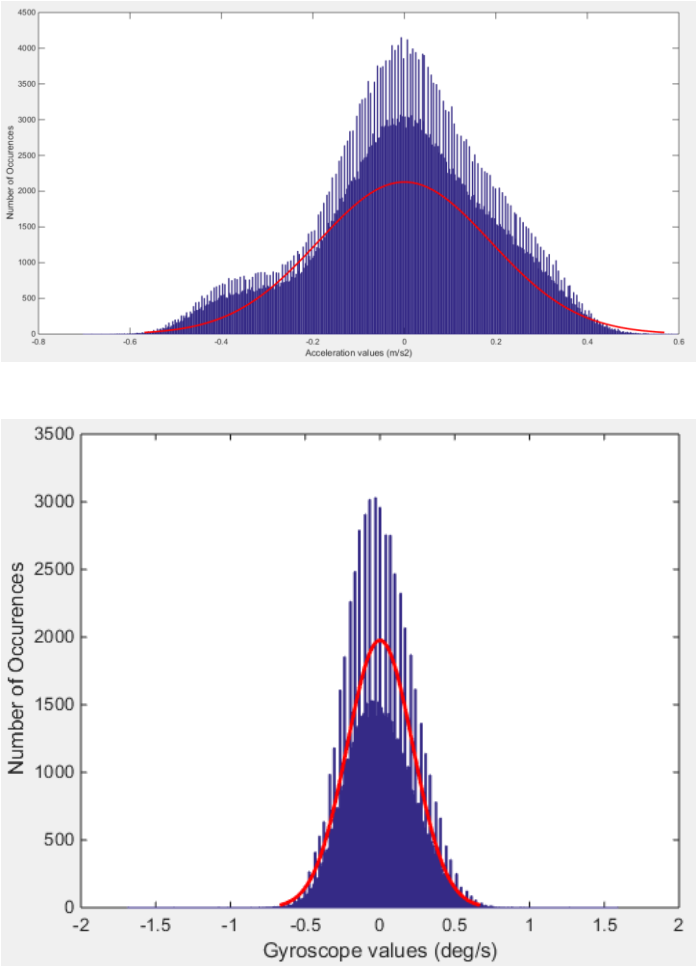

Figure 2.40: IMU-1 measurement noise histogram with Gaussian PDF plotted over it (above) accelerometer X (below) gyroscope X

NAME	VARIANCE
accX	0.0357
accY	0.0361
accZ	0.0177
gyroX	0.0500
gyroY	0.0625
gyroZ	0.0261

Table 2.9: IMU-1 measurement noise variances

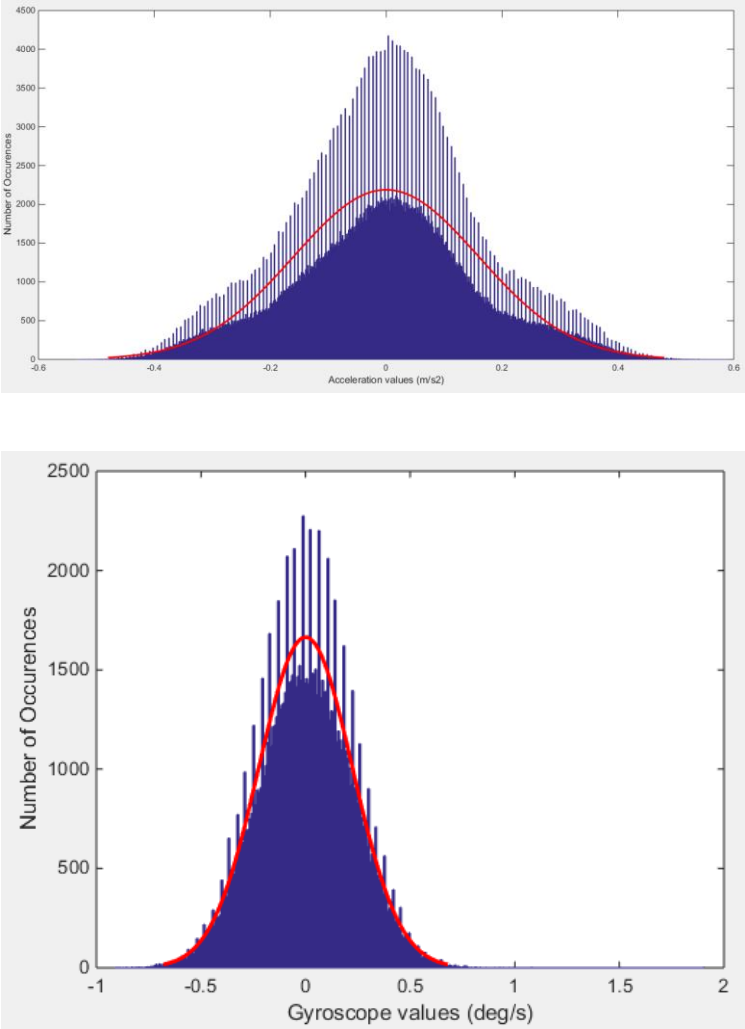

Figure 2.41: yIMU measurement noise histogram with Gaussian PDF plotted over it (above) accelerometer X (below) gyroscope X

NAME	VARIANCE
accX	0.0255
accY	0.0136
accZ	0.0118
gyroX	0.0482
gyroY	0.0463
gyroZ	0.0179

Table 2.10: yIMU measurement noise variances

In figure 2.41 we see the histograms for yIMU, we notice that the fit is not affected in any way hence the assumption of using Gaussian PDFs is validated. We notice a better fit in yIMU than in IMU-1.

2.5.5 Drifting Bias Analysis Results

Procedure: Once the static bias has been accounted for we perform a simple moving average on the resulting raw data to nullify the effect of measurement error on the raw data. The remaining effects are solely due to random walk error. We then calculate the ACF for this time series to find out Markov parameters as discussed in section 2.2.7.

Results:

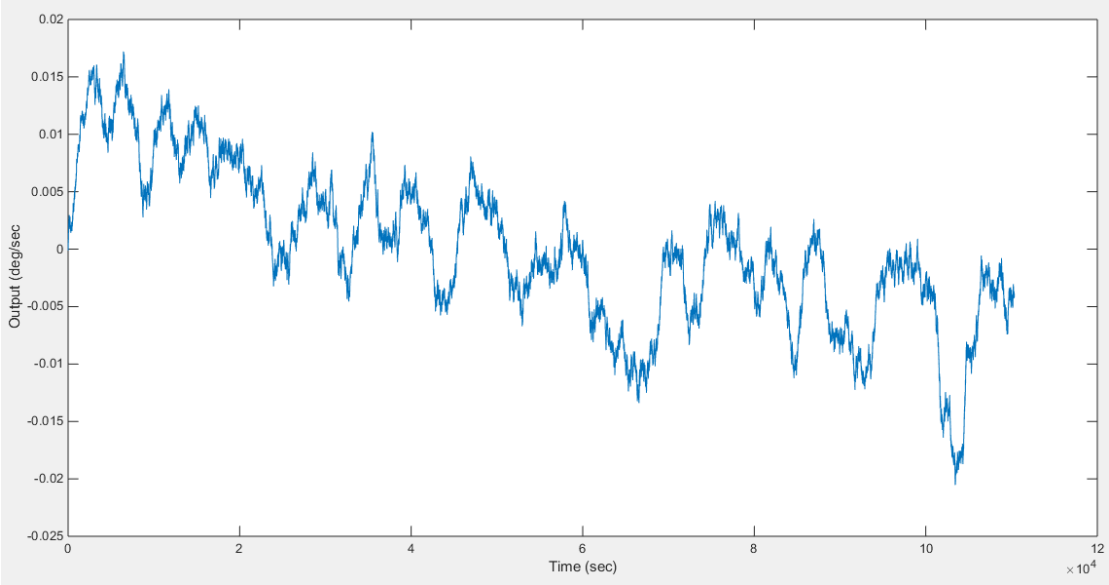

Figure 2.42: Random walk in IMU-1 gyroX

NAME	φ	σ^2_{bd}
accX	0.9987	$7.8813 * 10^{-7}$
accY	0.9976	$7.9789 * 10^{-7}$
accZ	0.9998	$3.7878 * 10^{-7}$
gyroX	0.9970	$1.0629 * 10^{-6}$
gyroY	0.9980	$1.3810 * 10^{-6}$
gyroZ	0.9965	$5.8003 * 10^{-7}$

Table 2.11: Markov parameters for single IMU-1

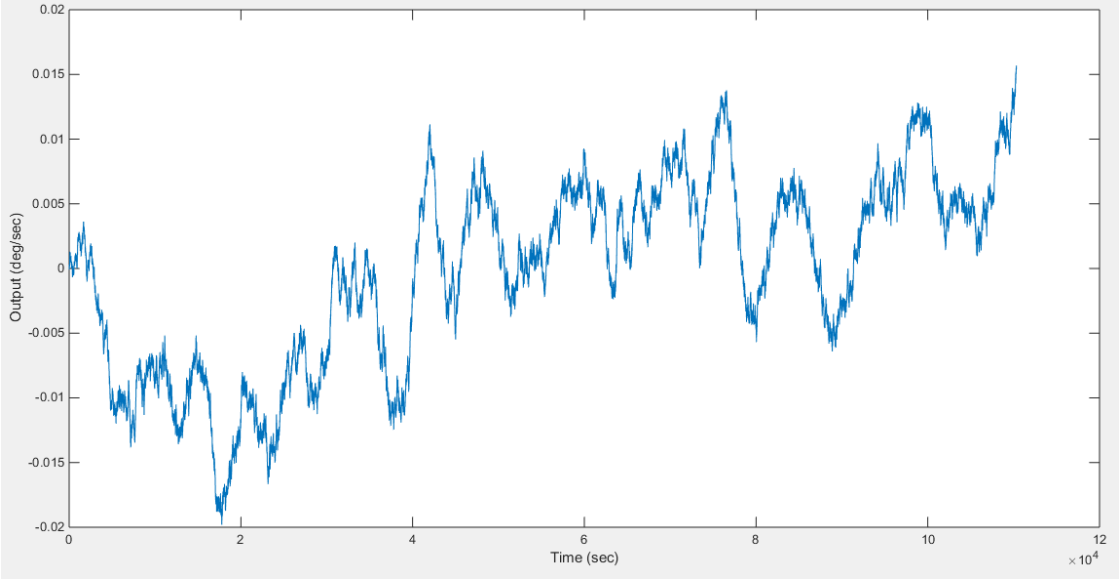

Figure 2.43: Random walk in yIMU gyroX

NAME	φ	σ^2_{bd}
accX	0.9997	$2.0470 * 10^{-7}$
accY	0.9980	$4.6136 * 10^{-7}$
accZ	0.9997	$1.6711 * 10^{-7}$
gyroX	0.9969	$1.1195 * 10^{-6}$
gyroY	0.9965	$1.0286 * 10^{-6}$
gyroZ	0.9967	$3.9966 * 10^{-7}$

Table 2.12: Markov parameters for yIMU and comparison to yIMU

From table 2.11 we notice that the effect of drifting bias on gyroscopes is more pronounced than in accelerometers. In table 2.12 we notice the significant reduction drifting bias in yIMU due to coupling opposing sense axes. But we note that the effect of drifting bias in itself is very small in static state (**φ** is around 1 and σ^2_{bd} is very small), but the effect is definitely more in dynamic state, which needs to be evaluated using techniques outside the scope of this thesis.

From figures 2.42 and 2.43, we notice the reduction in the random walk due to yIMU by magnitude. To see the remainder of the plots, see appendix B.

2.5.6 Orientation Tracking Performance

Procedure: A manual rotating protractor was used for test 1 to check for pose accuracy. For tests 2 and 3 a single axis rate table was used.

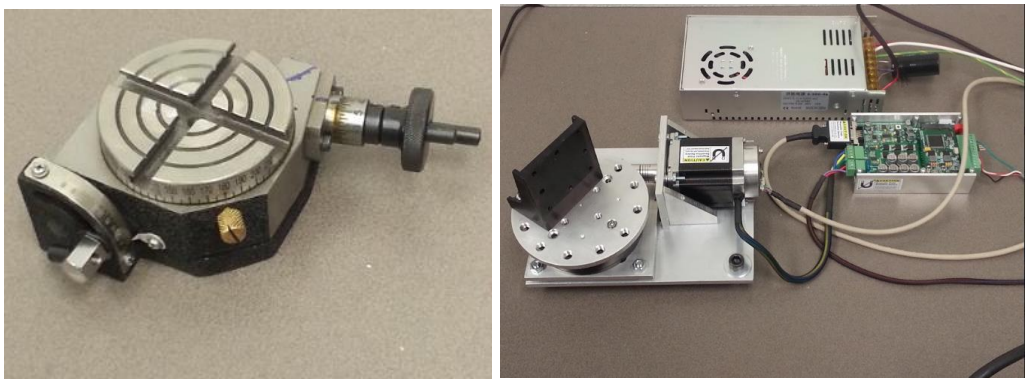

Figure 2.44: Tracking testing apparatus: (left) manual protractor; (right) single axis rate table

Test1: Rotate yIMU about z axis: 45^0 clockwise → 60^0 anticlockwise → 60^0 anticlockwise

Test 2: Around z axis: 30^0 clockwise, stop for 5 s → 30^0 anticlockwise, stop for 5 s→ 90^0 anticlockwise, stop for 5 s→ 90^0 clockwise; bringing yIMU to initial position. All rotation at constant 15 deg/sec.

Test 3: Around z axis: rotate clockwise 180^0 at 25 deg/sec → rotate anticlockwise 225^0 at 30 deg/sec → rotate clockwise 25^0 at 20 deg/sec; bringing yIMU to initial position. Here the rotation rates are varying to show dynamic performance.

Results:

As can be seen in figures 2.44 there is excellent yaw performance of yIMU without any external aiding. The algorithm is perfect for normal movements to be tracked on human body. In order to extend the performance of yIMU for higher dynamics more research needs to be done (see section 4.2). More rigorous testing could be done on a multi-axis gimbal which requires higher quality instrumentation currently unavailable in the lab.

NOTE: As the protractor is rotated by hand in figure 2.45 we see uneven movement of yIMU. For figure 2.46 at each change of speed vibration in the motor is picked up by accelerometer.

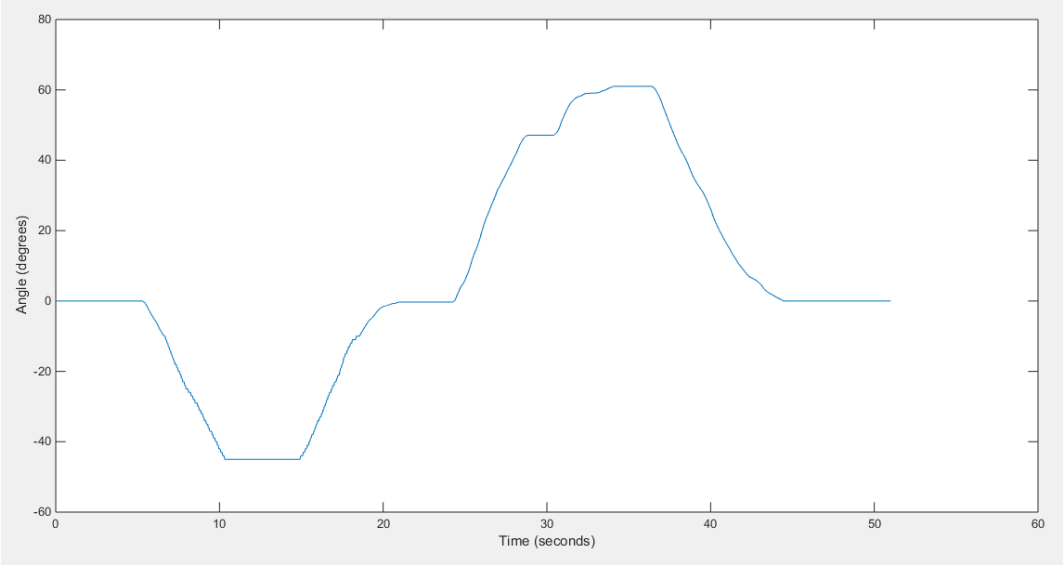

Figure 2.45: yaw vs time

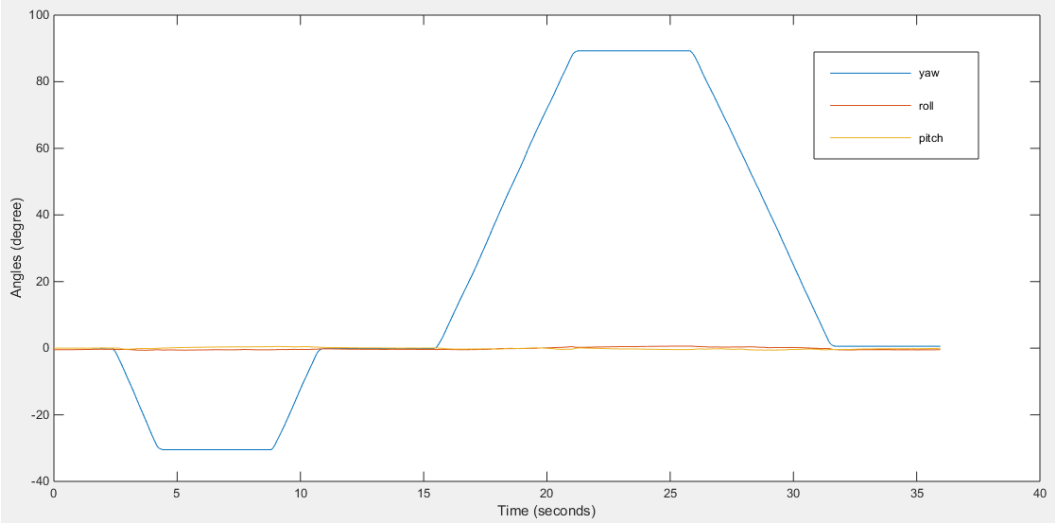

Figure 2.46: Rate table experiment about yaw axis- constant speed

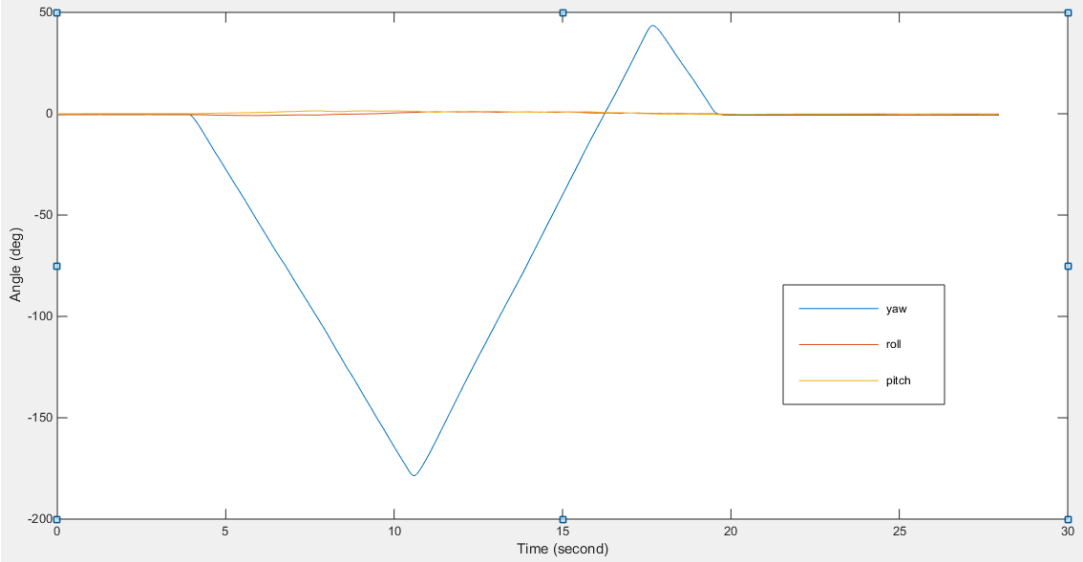

Figure 2.47: Rate table experiment about yaw axis- varying speed

UNAIDED YAW STABILITY

Stability of yaw in unaided inertial sensors is of concern. yIMU was tested against DMP algorithm. DMP is a proprietary algorithm from Invensense (InvenSense_Inc. 2013) that is inbuilt into MPU6050. As can be seen static stability of yIMU-gyroscopes is much

superior to DMP with only 0.5^0 yaw drift in more than an hour compared to around -8.12^0 drift for DMP in just 20 mins. It should be noted though the roll and pitch of DMP is quite stable due to aiding by accelerometer. As a comparison we have the drifts for MPU6050 gyroscope raw readings for 20 minutes. This clearly needs a lot of processing. As a comparison Navigation grade IMUs have a static bias stability of 0.35^0 /hr.

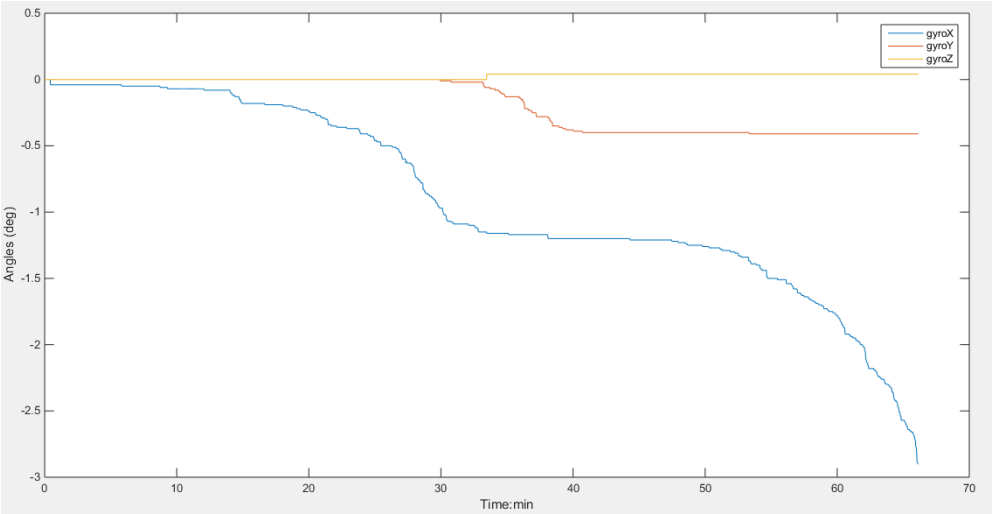

Figure 2.48: Static stability of yIMU- gyroscopes tested for 1 hour

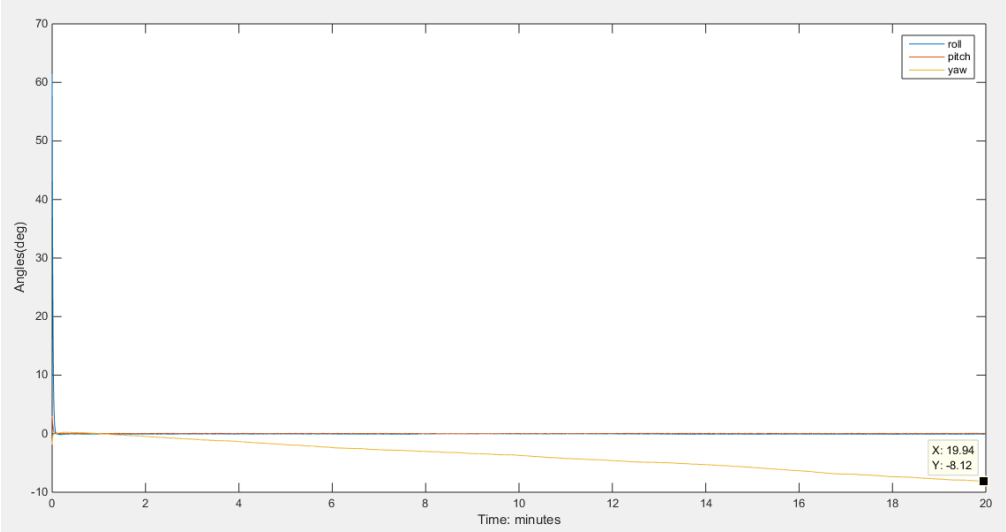

Figure 2.49: Static stability of MPU6050 with DMP algorithm tested for 20 mins

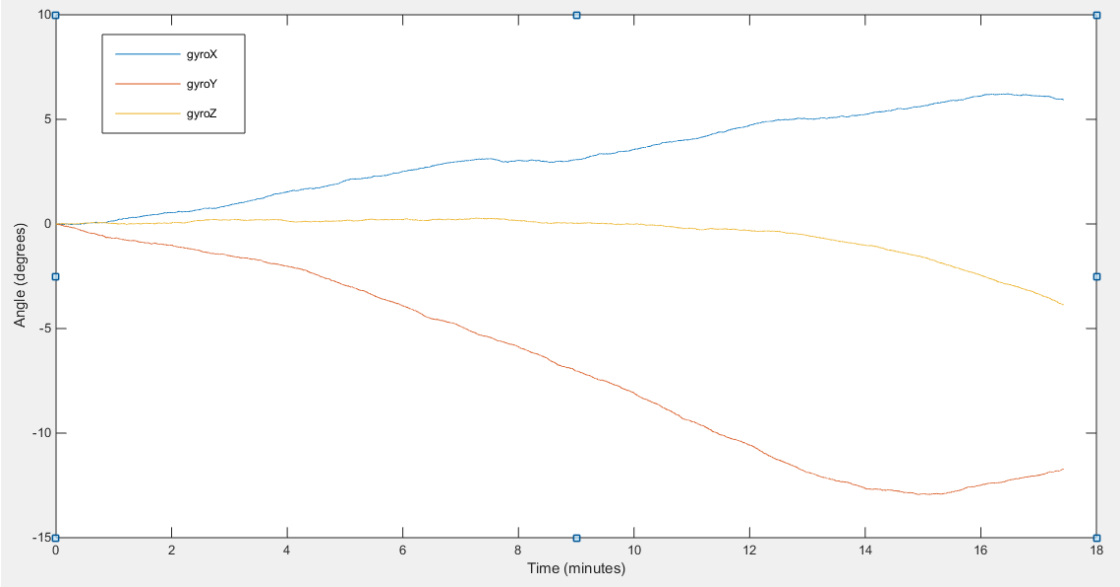

Figure 2.50: Raw gyro output from MPU6050 for 20 minutes: The bias offset has been compensated.

CHAPTER 3

JOINT ANGLE TRACKING USING INERTIAL SENSORS

In this chapter we discuss the development of a motion tracking system. In order to accurately track human motion precise tracking of joint angles is important. We use the custom built yIMU as the sensor nodes to track joint segment orientation. Human limb segment is then modelled as a kinematic chain and joint angle calculations are made. Though this implementation is for human upper body, it can be further extended to involve full body motion tracking in future. An experiment to conduct the viability of human motion tracking was done using MATLAB animation.

3.1 Joint Angle Tracking

This is a simple algorithm to track human body joint angles. Here we had applied to track motion of human limb. Section 3.1.1 describes the theoretical foundations of the procedure of kinematical modelling. In section 3.1.2 deals with sensor-segment calibration, which highly important to align the sensors to body frame and convert sensor orientation readings from body frame to global frame.

3.1.1 Kinematic Model of Human Limbs

DESCRIBING JOINT MOVEMENT

Human body is a complex system of joints and muscles. In order to study the movement certain terminologies have been developed with respect to a joint:

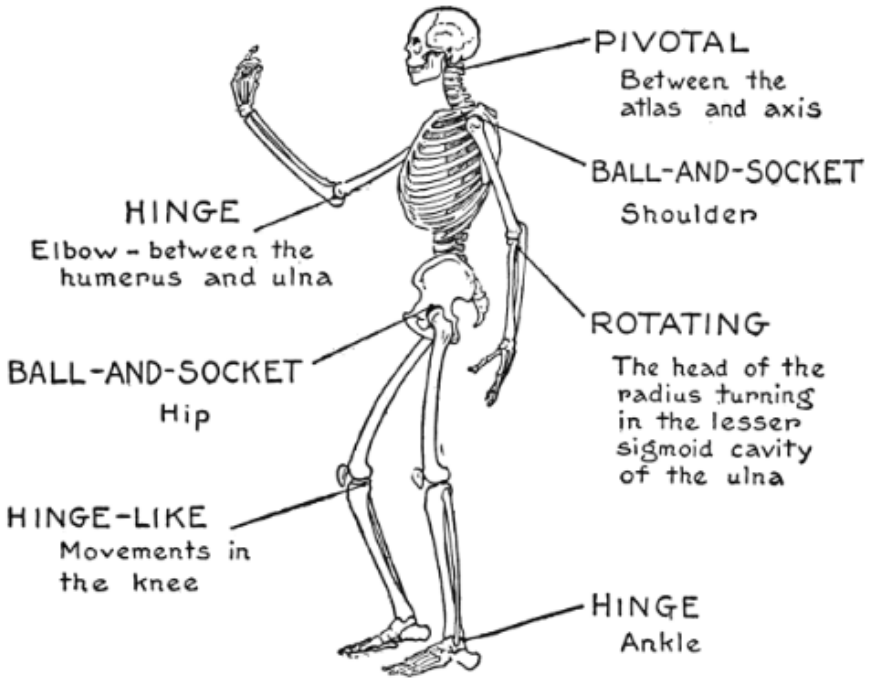

ARTICULATIONS OF THE SKELETON ILLUSTRATING VARIOUS KINDS OF MECHANICAL JOINTS AND MOVEMENTS.

Figure 3.1: Movements in human joints (Luitz 2013)

1. Flexion and extension- These movements occur in many joints in the body, including head, trunk, shoulder, elbow, hip and knee. Flexion is a bending movement that decreases the joint relative angle between two adjacent segments. Lifting the forearm up at the elbow is an example of elbow flexion. Extension is a straightening movement that increases the joint relative angle between two adjacent segments.
2. Abduction and adduction- These movements are not as common as flexion and extension. They occur in the scapula, shoulder, wrist, and hip joints. Abduction is a movement away from the midline of the body. Raising an arm out to the side of the body is an example of abduction. Adduction, on the other hand, is the return movement of the segment back toward the midline of the body.

3. Segment internal and external rotation- They occur in the head, trunk, shoulder, hip and knee joints. Internal rotation occurs when the segment rotates about the vertical axis toward the midline of the body. External rotation is the opposite movement away from the body midline.
4. Pronation and supination- They occur as the distal end of the radius rotates over and back at the radioulnar joint. While the elbow is flexed, supination occurs in the forearm when the palm rotates to face upward. Pronation is the opposite movement to bring the palm back to face downward

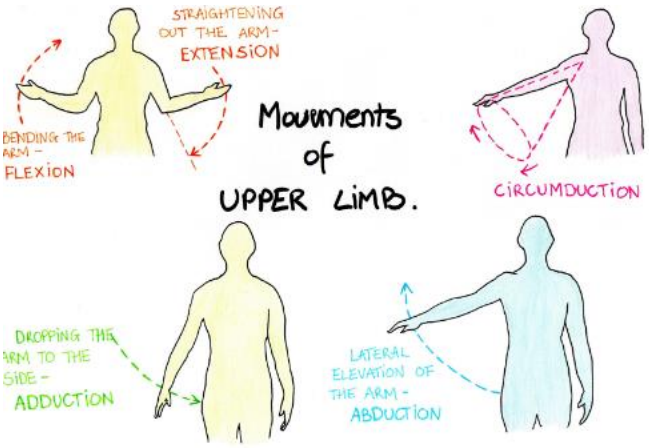

Figure 3.2: Categories of joint movements (Pau)

THE CONCEPT OF KINEMATIC CHAIN

Kinematic chain refers to an assembly of rigid bodies connected by joints that is the mathematical model for a mechanical system (Wikipedia). The degrees of freedom, or mobility, of a kinematic chain is the number of parameters that define the configuration of the chain. The DOF for a rigid body free to move in space is 6, hence for **n** distinct segments the DOF is **6n**. It can be shown that DOF for a kinematic chain formed from **n** moving links and **j** joints each with freedom $\mathbf{f_i}$, **i=1, ..., j** and **N** fixed links, is given by:

$$M = 6n - \sum_{i=1}^{j}(6 - fi) = 6(N - 1 - j) + \sum_{i=1}^{j} fi$$

(3.1)

Two or more rigid bodies in space are collectively called a rigid body system. We can hinder the motion of these independent rigid bodies with kinematic constraints. Kinematic constraints are constraints between rigid bodies that result in the decrease of the degrees of freedom of rigid body system. In order to describe the individual motion in series we use transformation matrices. This procedure is known as forward kinematics formulation. The transformation matrix **T** for an **n** segment kinematic chain with individual matrices described by $\mathbf{X_i}$, where **i=1, ….., n-1** and $\mathbf{Z_i}$, where **i= 1,…,n** is the link transformation matrix is given by the serial kinematic chain:

$$[T] = [Z_1][X_1][Z_2][X_2] \dots \dots [X_{n-1}][Z_n] \quad \textbf{(3.2)}$$

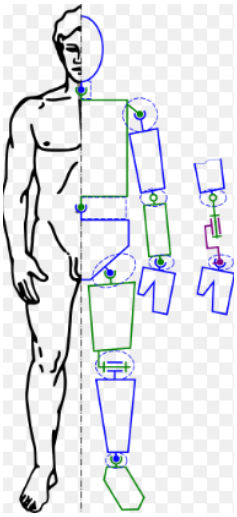

Figure 3.3: Visualizing human body as series of kinematic segments (Wikipedia)

Robotic arms have been developed to mimic human arm dexterity. Hence the system used in kinematic modelling of robotic arms can in turn be used to mathematically describe

human limb. The complex human body can be modeled as a multi-link system comprised of several body segments. Body segments are thereby treated as rigid bodies and are mutually connected by joints to form a tree-like structure. The specification of pose of the body requires that orientations and positions of every individual segment are determined. Type of formalism chosen to describe relationships between body segments in a model, determines whether the positions and orientations of the segments are described individually or are specified relative to one another.

DENAVIT HARTENBERG CONVENTION

In a kinematic model that represents articulated structures as a series of inter-connected links, the geometrical relationship between links may generally be described using either homogenous transformation matrices or quaternion/vector pairs. A homogenous transformation matrix is a 4x4 matrix which expresses both the rotation and translation of a joint's individual reference frame related to the reference frames of adjacent link.

In DH notation, four parameters are used to describe the relationship between adjacent frames: link length, link twist, link offset and the joint angle. Every joint with multiple degrees of freedom can be modeled as an assembly of multiple one-degree-of-freedom joints and for those joints only changes in joint angle occur. All other parameters are fixed:

- **d**: offset along previous axis of rotation, **z** to the normal
- **Θ**: angle about the previous z, from old **x** (part of right handed coordinate system) to new **x**
- **a:** length of the common normal
- **α:** angle about the common normal, from old **z** axis to new **z** axis

For in depth treatment of the DH convention see (Craig 2005).

KINEMATIC MODELLING OF UPPER LIMB

We create a 6 DOF upper limb model with following constraints:

1. Shoulder joint is assumed stationary with 3 DOF spherical joint: abduction/adduction, flexion/external, internal/external rotation.
2. Elbow joint is modelled as having 3 DOF spherical joint: abduction/adduction, flexion/external, internal/external rotation.

The DH table for this configuration is shown in Table 3.1.

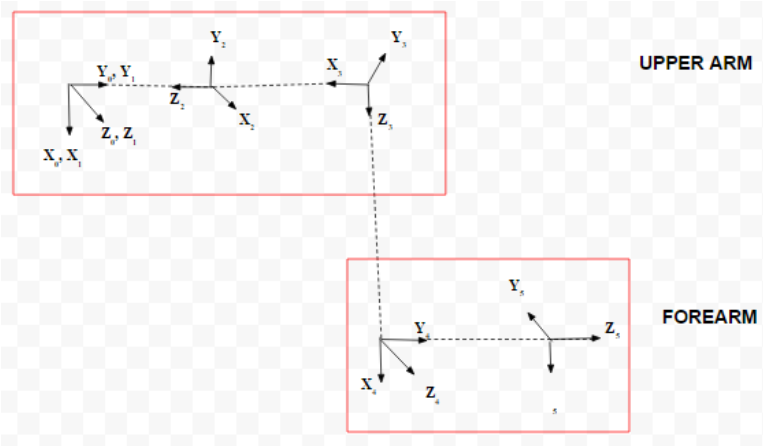

Figure 3.4: Kinematic modelling of human upper limb

Frame	$\alpha_{(i-1)}$	$a_{(i-1)}$	d_i	Θ_i
1	0	0	0	Θ_1
2	90^0	0	0	Θ_2+90^0
3	90^0	0	l_1	Θ_3+90^0
4	90^0	0	0	Θ_4+90^0
5	-90^0	0	l_2	Θ_5

Table 3.1: DH parameters for upper limb: here l_1 is the length of the upper arm; l_2 is the length of the forearm

FORWARD KINEMATICS

Once the sensor-segment calibration is done as discussed in section 3.1.2, we have to implement forward kinematic formulation to calculate the pose of the joints in 3D space. Now we have to deal with two frames of reference: global frame of reference and body frame of reference attach at each of the joint as shown in the figure 3.6.

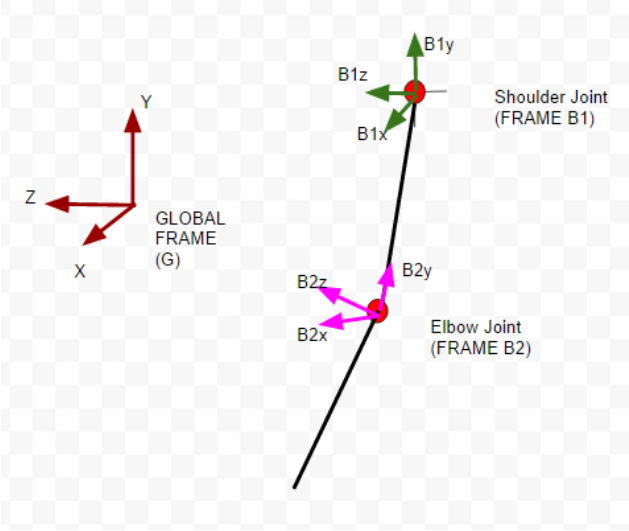

Figure 3.5: Forward kinematics- frames of reference

First we define the orientation calculated at each of the joint: $\boldsymbol{\varphi_1}$ is the roll calculated at shoulder (abduction/adduction), $\boldsymbol{\Theta_1}$ is the pitch calculated at the shoulder (rotation) and $\boldsymbol{\Psi_1}$ is the yaw calculated at the shoulder (flexion/extension). We have the similar nomenclature for elbow orientation: $\boldsymbol{\varphi_1}$, $\boldsymbol{\Theta_1}$ and $\boldsymbol{\Psi_1}$.

Now we calculate the pose of the point fixed at elbow with respect to global frame $\boldsymbol{r_e^G}$ using the following equation:

$$\boldsymbol{r_e^G = R_{B1}^G * r_e^{B1}} \quad \textbf{(3.3)}$$

where $\boldsymbol{R_{B1}^G}$ is the rotation matrix for shoulder frame, **B1** with respect to global frame, **G**; and $\boldsymbol{r_e^{B1}}$ is the position of elbow with respect to shoulder frame of reference. The rotation matrix $\boldsymbol{R_{B1}^G}$ is calculated by using Euler rotation transformation matrix following Z-Y-X convention.

$$\boldsymbol{R_{B1}^G} = \begin{bmatrix} \boldsymbol{cos}\Psi_1 & -\boldsymbol{sin}\Psi_1 & \mathbf{0} \\ \boldsymbol{sin}\Psi_1 & \boldsymbol{cos}\Psi_1 & \mathbf{0} \\ \mathbf{0} & \mathbf{0} & \mathbf{1} \end{bmatrix} * \begin{bmatrix} \boldsymbol{cos}\theta_1 & \mathbf{0} & \boldsymbol{sin}\theta_1 \\ \mathbf{0} & \mathbf{1} & \mathbf{0} \\ -\boldsymbol{sin}\theta_1 & \mathbf{0} & \boldsymbol{cos}\theta_1 \end{bmatrix} * \begin{bmatrix} \mathbf{1} & \mathbf{0} & \mathbf{0} \\ \mathbf{0} & \boldsymbol{cos}\boldsymbol{\varphi}_1 & -\boldsymbol{sin}\boldsymbol{\varphi}_1 \\ \mathbf{0} & \boldsymbol{sin}\boldsymbol{\varphi}_1 & \boldsymbol{cos}\boldsymbol{\varphi}_1 \end{bmatrix}$$

$$= \begin{bmatrix} \boldsymbol{cos}\theta_1 * \boldsymbol{cos}\Psi_1 & \boldsymbol{cos}\Psi_1 * \boldsymbol{sin}\theta_1 * \boldsymbol{sin}\boldsymbol{\varphi}_1 - \boldsymbol{cos}\theta_1 * \boldsymbol{sin}\Psi_1 & \boldsymbol{sin}\boldsymbol{\varphi}_1 * \boldsymbol{sin}\Psi_1 + \boldsymbol{cos}\boldsymbol{\varphi}_1 * \boldsymbol{cos}\Psi_1 \boldsymbol{sin}\theta_1 \\ \boldsymbol{cos}\theta_1 * \boldsymbol{sin}\Psi_1 & \boldsymbol{cos}\boldsymbol{\varphi}_1 * \boldsymbol{sin}\Psi_1 + \boldsymbol{sin}\theta_1 * \boldsymbol{sin}\boldsymbol{\varphi}_1 * \boldsymbol{sin}\Psi_1 & \boldsymbol{cos}\boldsymbol{\varphi}_1 * \boldsymbol{sin}\theta_1 * \boldsymbol{sin}\Psi_1 - \boldsymbol{cos}\Psi_1 * \boldsymbol{sin}\boldsymbol{\varphi}_1 \\ -\boldsymbol{sin}\theta_1 & \boldsymbol{cos}\theta_1 * \boldsymbol{sin}\Psi_1 & \boldsymbol{cos}\boldsymbol{\varphi}_1 * \boldsymbol{cos}\theta_1 \end{bmatrix}$$

(3.4)

Next we calculate the pose of the point fixed at the end of forearm (at the wrist) as follows:

$$\boldsymbol{r_W^G = r_E^G + r'^G_W} \quad \textbf{(3.5)}$$

where $\boldsymbol{r_W^G}$ is the pose of the wrist with respect to global frame; $\boldsymbol{r_E^G}$ is the pose of the elbow joint as calculated previously and $\boldsymbol{r'^G_W}$ is the pose of the wrist with respect to global frame without taking into account that it is attached to elbow.

$\boldsymbol{r'^{G}_{W}}$ is calculated based on the following equation:

$$\boldsymbol{r^{G}_{e} = R^{G}_{B1} * R^{B1}_{B2} * r^{B2}_{w}} \quad \textbf{(3.6)}$$

where $\boldsymbol{R^{G}_{B1}}$ is the rotation matrix for **B1** with respect to **G** (as calculated before); $\boldsymbol{R^{B1}_{B2}}$ is the rotation matrix for **B2** with respect to **B1**; and $\boldsymbol{r^{B2}_{w}}$ is the position of wrist with respect to frame **B2**.

3999

JOINT ANGLE CALCULATIONS

The shoulder joint angles can be readily calculated by the matrix $\boldsymbol{R^{G}_{B1}}$ as the shoulder joint is assumed fixed. The calculation of elbow joint angle in 3D reduces to finding the angle between vectors in 3D space. We use the cosine rule:

$$\boldsymbol{\bar{a}.\bar{b} = ab\cos}(\theta) \quad \textbf{(3.7)}$$

The pose of the upper arm is given by $\boldsymbol{r^{G}_{e}}$ and the pose of the forearm is given by $\boldsymbol{r^{G}_{W}}$. Hence first we normalize the vectors $\boldsymbol{r^{G}_{e}}$ and $\boldsymbol{r^{G}_{W}}$ and then use the equation:

$$\theta = \boldsymbol{\mathrm{acos}(r_1.r_2)} \quad \textbf{(3.8)}$$

where $\boldsymbol{r_1 = \frac{r^{G}_{e}}{|r^{G}_{e}|}}$ and $\boldsymbol{r_2 = \frac{r^{G}_{W}}{|r^{G}_{W}|}}$ and $\boldsymbol{\Theta}$ is the elbow joint angle.

3.1.2 Sensor-Segment Calibration

The attachment of sensor to segment may not be perfect. It is important to have them aligned if the system has to work. A simple way is to use a pre-determined pose to initialize the adjustment along with the fact that gravity always points down in the global frame.

We make the subject stand straight for a period of 30 s at the beginning of the experiment to do his alignment. In order to have better accuracy, the subject is instructed to be as still as possible. This is used to determine the rotation matrix **R** which is the rotation matrix of sensor to segment frame. The known gravity component **G** is aligned with the segment frame by making the subject stand hands down and straight. If **B** is the body frame in a particular pose, we then have:

G= R x B **(3.9)**

This matching of sensor frame to global frame is done using least square iteration (Hamdi, Mohammed I. Awad et al. 2014). Once we have determined **R** from the above equation we use it for transforming orientation measurements in sensor frame to segment frame as follows:

$[a_{sx}\ a_{sy}\ a_{sz}]' = R\ x\ [a_{bx}\ a_{by}\ a_{bz}]'$ for accelerometers **(3.10)**

$[g_{sx}\ g_{sy}\ g_{sz}]' = R\ x\ [g_{bx}\ g_{by}\ g_{bz}]'$ for gyroscopes **(3.11)**

Where $[a_{sx}\ a_{sy}\ a_{sz}\ g_{sx}\ g_{sy}\ g_{sz}]$ are sensor outputs in the segment frame; $[a_{bx}\ a_{by}\ a_{bz}\ g_{bx}\ g_{by}\ g_{bz}]$ are the sensor outputs in the sensor frame of reference; and **R** is the rotation matrix.

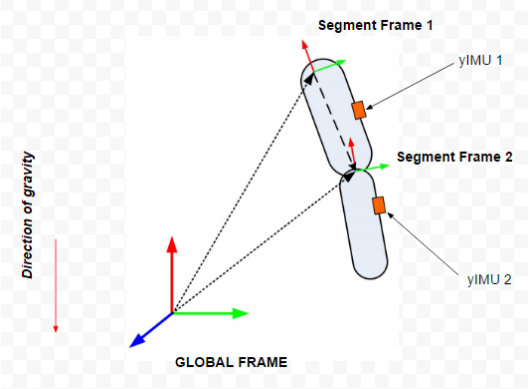

Figure 3.6: Sensor-segment calibration

3.1.3 System Design

The system consists of yIMU as sensor nodes that are firmly attached to human limb segments. The orientation data is sent to the main hub (computer) via Bluetooth. The range of Bluetooth is 10 m. The logged data is processed off line to calculate joint angles by applying the kinematic concepts developed earlier. This processing is done on MATLAB.

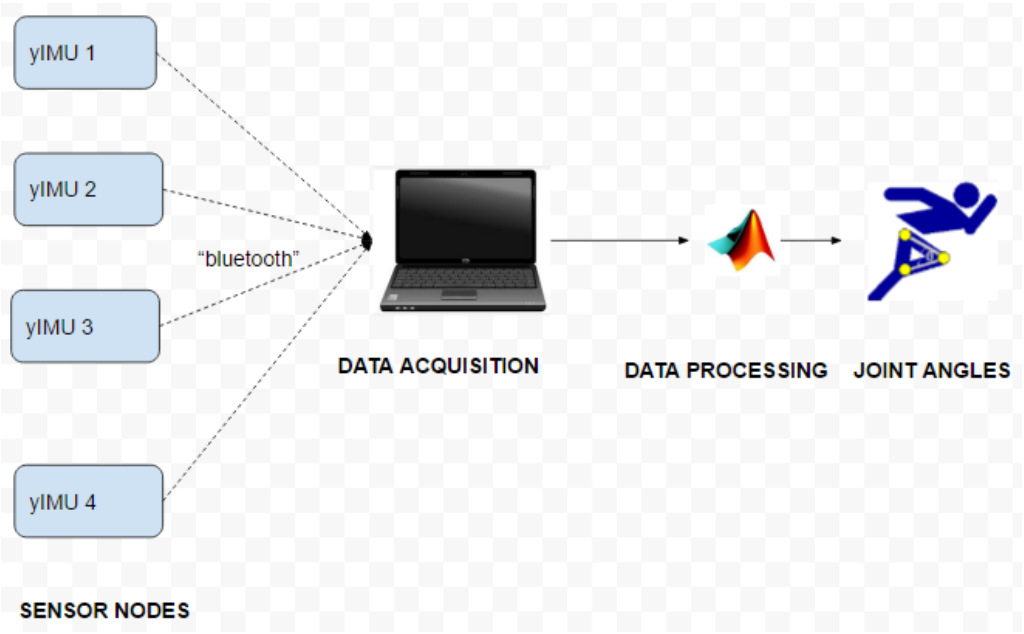

Figure 3.7: Tracking system design

3.2 Performance Evaluation

In this section we evaluate the performance of the inertial tracking algorithm as applied to yIMU. In 3.2.1 the experimental procedure to validate the system has been documented. In section 3.2.2 we discuss the conclusions drawn from the results and some improvements for further development of the joint angle tracking system.

3.2.1 Experiment

The system was setup with IMUs mounted on upper arm and lower arm as shown in figure 3.8. The initial few seconds the subject was asked to remain still for sensor-segment calibration, then the subject was directed to move arms in any pattern. While the data was being wirelessly logged via Bluetooth on computer, a camera simultaneously recorded the movements.

The forward kinematic technique previously discussed was implemented in MATLAB and used to calculate joint angles. The accuracy was tested using Noraxon IMUs. The best RMSE was found to be 2.7308 for shoulder adduction/abduction calculations, it varied to as high as 18.230 (for fast movements) for elbow flexion. The table 3.2 shows the result of these tests for each of the angles.

Figure 3.8: yIMU placement on subject body

Joint Angle	RMSE
Shoulder adduction/abduction	2.7308
Shoulder flexion/extension	3.1052
Shoulder rotation	6.8133
Elbow flexion/extension	3.1255
Knee flexion/extension	6.5806

Table 3.2: Joint angles RMSE with respect to Noraxon IMUs- normal movements

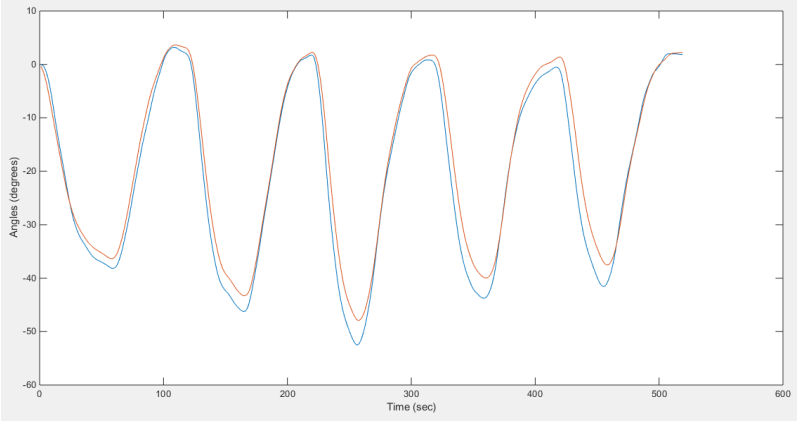

Figure 3.9: Graph comparing the shoulder adduction/abduction calculated using the Noraxon IMUs with yIMU: blue(Noraxon), red (yIMU)

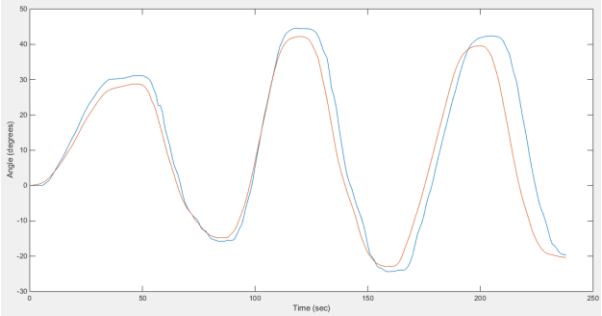

Figure 3.10: Graph comparing the shoulder rotation calculated using the Noraxon IMUs with yIMU

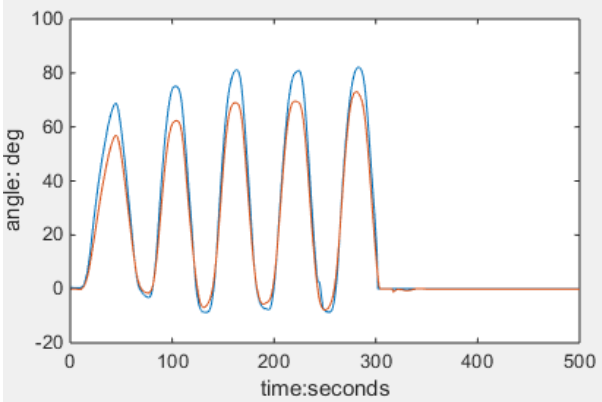

Figure 3.11: Graph comparing the elbow flexion angle calculated using the Noraxon IMUs with yIMU

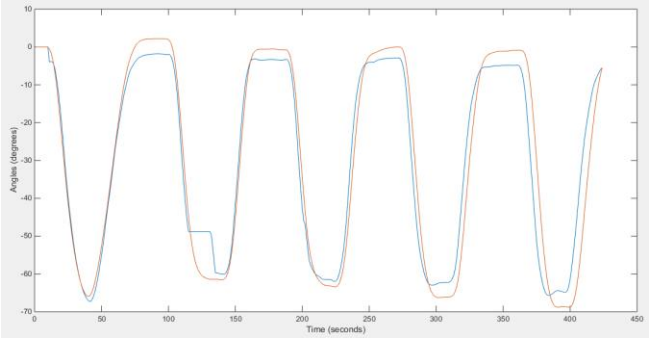

Figure 3.12: Graph comparing the knee flexion angle calculated using the Noraxon IMUs with yIMU

3.2.2 Results and Discussion

As a result of the above experiments we can conclude that yIMU can be adequately used for human motion tracking. It is to be noted that no external aiding sensors were used. The tracking was processed off-line. The tracking algorithm is stable over a long period of time and accurate for a wide range of motions even without magnetometer aiding typically used for yaw angle calculations. The orientation tracking performance evaluated in section 2.5.6 points to promising results from such an experiment. In addition, for better motion tracking performance it would be priority to reduce the form-factor of the IMU for easy and firm mounting on the body segments. This would definitely be implemented in future work. If allowances for misalignment errors due to the bulky nature of the prototype were to be made, it is highly possible to have average RMSE below 3 deg.

The commerciality of the device has hence been thoroughly established for human motion tracking application. This low-cost system costs less than $15 and has great potential for a wide range of applications.

Chapter 4

CONCLUSION

The initial motivation of the thesis was to develop an efficient joint angle tracking algorithm using rigid kinematic constraints. But while working on this, a sore need for increasing the raw performance of inertial sensors were noted. Hence the bulk of the work focusses of development of a new attitude reference system using inertial sensors. Experiments were carried out to prove the applicability of a dual IMU system to improve noise performance. Adequate processing of the raw inertial data was done to arrive at unprecedented stability in inertial sensor readings unaided by any external sensors. An efficient joint angle tracking algorithm was implemented to track human motion which can be further extended to development of a motion capture system.

Key areas of further improvements were identified and the work to take yIMU to the next level is already under process.

4.1 Contributions

The most important contribution of this research is to prove the applicability of low-cost inertial measurement unit to tracking human motion with precision. To the best of author's knowledge, no other custom built low-cost IMU unaided by magnetometer has been demonstrated to show such accuracy. This quest to not use magnetometer was inspired by the important problem of magnetic interference in indoor environments. In addition, yIMU outputs accurate quaternions/ Euler angles as against raw data which is done my most of the low cost systems in market. This simplifies the post-processing scheme.

The following is the summary of the results that form the core of the thesis:

1. Common Mode Effect is highly dependent on the type on sensor used. MPU6050 is a low-cost sensor with repeatable characteristics that can take advantage of this effect in a particular configuration.
2. Testing for viability of improvements in measurements just by using this configuration has been proven to be true. Tests were done to see improvements in noise performance and effect of environmental factors.
3. Exceptionally good unaided yaw performance was tested by virtue of significant improvements in gyro performance of yIMU.
4. The system was built on an open source platform with very low processing power pointing to the fact that much better units could be built with good commercial scalability.
5. Used for joint angle tracking with much better results than similar systems, hence the use of yIMU in motion capture systems is validated.

On the basis of yIMU, a human motion tracking system was built from scratch. A very streamlined algorithm was developed which underscores the possibility of smartly implementing simple techniques for much greater improvements in accuracy instead of relying on standard Kalman filtering techniques. This shows that sensor fusion only works best if the theory behind the processes is thoroughly understood and implemented instead of using a standard algorithm blindly. This understanding enabled the development of a computationally efficient system with great potential.

4.2 Future Work

This thesis presents an effective device to bring down the cost of inertial human motion tracking systems that are currently in market. Applications to joint angle tracking and pedestrian navigation was explored here but the scope of application is much huge, especially in the wearable medical devices market.

With enough funding and dedicated team of developers this system could be hugely improved:

1. Exhaustive characterization of low-cost IMUs need to be done to take into all the errors. This is very time-consuming.
2. Further development of dynamic stability of yIMU is needed. This would increase the scope of application to tracking highly dynamic sports like baseball and running. One idea would be to include addition sensors to create a larger sensor array. This would require sophisticated research into efficient geometric configurations to implement a skew-redundant system.
3. A more elaborate calibration routine would enable yIMU to come closer to the performance of tactical grade inertial sensors. This would require accurate compensation for scale factor error, misalignment error and development of an on-line bias estimation routine.
4. Hardware development of the IMU. Funding and adequate expertise in embedded systems has been a huge impediment in development of the device. Implementation of any stochastic algorithm or sophisticated bias estimation would require more

powerful hardware options. The commerciality of the concept though has been thoroughly established.

5. As far as the joint angle tacking algorithm is concerned, no velocity constraints were applied and the implementation was not done in state-space form. On testing, it was concluded that such implementations work best only by using Kalman filter. A preliminary EKF filter using velocity constraints was built (not included in the thesis), but the results were not encouraging. This implied the design needs more elaborate error modelling scheme than what was used in this thesis in addition to better processor speeds on the hardware side. The concept though is very useful and will be fruitfully pursued for future improvements.
6. Exhaustive testing for medical applications has not been done. Human rehabilitation studies needed to implement a more robust sensor to segment calibration routine. Using UKF for joint angle tracking could be a more lucrative choice. More research needs to be done in this area.
7. Building a real-time system heavily depends on the usage of better hardware and friendly UI development.
8. Building a new IMU with magnetometer and appropriate distortion correction algorithms would be very handy for many applications. yIMU can be integrated into any system that requires inertial tracking. This is a 6DOF system on chip with inbuilt smart sensor fusion that can give accurate orientation without magnetometer aiding for longer durations of time than any current low-cost sensor. This could prove to be useful when external aiding sensors cannot be trusted due to various factors that can be accordingly modelled into a robust fault detection scheme.

9. yIMU has wide ranging applications and can be easily integrated for DIY projects, the following list is of some major applications:
    a. Motion capture, activity and other human tracking applications.
    b. Gesture control, head tracking and other gaming applications.
    c. Pedestrian navigation.
    d. Orientation control in drones

    All these applications would require more complex algorithm with domain specific constraints which require extensive research.

REFERENCES

Aggarwal, P., et al. (2006). Cost-effective Testing and Calibration of Low Cost MEMS Sensors for Integrated Positioning, Navigation and Mapping Systems Shaping the Change XXIII FIG Congress. Munich, Germany.

Allan, D. W. (1966). Statistics of atomic frequency standards. Proceedings of the IEEE.

Alvarez, H. D. E. (2010). Geometrical Configuration of Redundant Inertial Measurement Unit. Department of Mechanical Engineering, University of Texas at Austin. Master of Science.

Analog_Devices. "ADIS16365 product overview ". from http://www.analog.com/en/products/sensors/inertial-measurement-units/adis16365.html#product-overview.

Bancroft, J. B. and G. Lachapelle (2011). "Data Fusion Algorithms for Multiple Inertial Measurement Units " Sensors.

Barrett, J., et al. (2012). "Analyzing and Modelling an IMU for Use in a Low-Cost Combined Vision and Inertial Navigation System." IEEE: 21-22.

Benoussaad, M., et al. (2016). "Robust Foot Clearance Estimation Based on the Integration of Foot-Mounted IMU Acceleration Dat." Sensors: 3-6.

CH_Robotics. "Understanding Euler Angles."

Craig, J. J. (2005). Introduction to robotics, Pearson Prentics Hall.

eLegs (2010). from http://bleex.me.berkeley.edu/research/exoskeleton/elegs%E2%84%A2/.

El-Gohary, M. and J. McNames (2015). "Human Joint Angle Estimation with Inertial Sensors and Validation with a Robot Arm." IEEE Transactions on Biomedical Engineering 62(7): 1759-1766.

Fourati, H., et al. (2013). "A Complementary Sliding Mode Observer Approach for Motions Human Body Segments Capturing by Means of Wearable Inertial and Magnetic MEMS Sensors Assembly." IEEE/ASME Transactions on Mechatronics.

Greenheck, D. R., et al. (2014). Design and Testing of a Low-Cost MEMS IMU Cluster for SmallSat Applications. 28th Annual AIAA/USU Conference on Small Satellites. Logan, Utah: 6-8.

Grewal, M. S., et al. (2001). global positioning systems inertial navigation and integration, Wiley-Ineterscience.

Groves, P. D. (2013). Principles of GNSS, Inertial, and Multisensor Integrated Navigation Systems, Arctech House.

Hamdi, M. M., et al. (2014). Lower Limb Motion Tracking Using IMU Sensor Network. Cairo International Biomedical Engineering Conference Cairo, Egypt.

Hol, J. (2011). Sensor Fusion and Calibration of Inertial Sensors, Vision, Ultra-Wideband and GPS. Department of Electrical Engineering, Linkoping University Doctor of Philosophy.

Hong, S. K. and S. Park (2008). "Minimal-Drift Heading Measurement using a MEMS Gyro for Indoor Mobile Robots." Sensors: 7295-7296.

Innoventions. "Accelerometers." from http://www.rotoview.com/accelerometer.htm.

InvenSense_Inc. (2013). MPU-6000 and MPU-6050 Product Specification Revision 3.4.

Kanjanapas, K., et al. (2013). "A Human Motion Capture System based on Inertial Sensing and a Complementary Filter." ASME: 3-6.

Kavanagh, J. J., et al. (2006). "Reliability of segmental accelerations measured using a new wireless gait analysis system." Journal of Biomechanics.

Kerestes, J. (2014). Robotic Augmentation Of Human Locomotion For High Speed Running. Department of Mechanical Engineering, Arizona State University. Master of Science.

Koldbæk, S. K. and L.-C. Totu (2011). Improving MEMS Gyroscope Performance using Homogeneous Sensor Fusion. Department of Electronic Systems, Aalborg University. Master of Science: 61-64.

Kong, K. and M. Tomizuk (2009). "A Gait Monitoring System Based on Air Pressure Sensors Embedded in a Shoe." IEEE/ASME Transactions on Mechatronics 4(3).

KVH_Industries (2014). Guide to Comparing Gyro and IMU Technologies- MEMS and FOGs, .

Kwakkel, S. P. (2008). Human Lower Limb Kinematics Using GPS/INS. Department of Geomatics Engineering, Schulich School of Engineering. Master of Science.

Looney, M. "The Basics of MEMS IMU/Gyroscope Alignment." from http://www.analog.com/library/analogdialogue/archives/49-06/IMU_Gyroscope.html.

lubopitko-bg. "Joint Articulations." from http://encyclopedia.lubopitko-bg.com/Joints_Articulations.html.

Luitz, E. G. (2013). "Practical Anatomy." from http://www.drawingbooks.org/lutz1/source/index.html.

Martin, H. and P. Groves (2016). "The Limits of In-Run Calibration of MEMS Inertial Sensors and Sensor Array." Journal of The Institute of Navigation.

Martin, H., et al. (2013). A new approach to better low-cost MEMS IMU performance using sensor arrays. I. o. N. GNSS. Nashville,TN,USA: 3-7.

Masters, M., et al. (2015). "Real-Time Arm Tracking for HMI Applications." IEEE.

Nilsson, J. O. and I. Skog (2016). Inertial sensor arrays – A literature reviewin Proceedings of European Navigation Conference. Helsinki, Finland.

NXP. "NXP Sensor Fusion." from http://www.nxp.com/products/sensors/nxp-sensor-fusion:XTRSICSNSTLBOX.

Paina, G. P., et al. (2011). Experimental comparison of Kalman and complementary filter for attitude estimation. Argentine Symposium on Technology. Cordoba, Argentina.

Pau. "Pau's Medical Biology Notes." from https://pausmedicalbiologynotes.wordpress.com/tag/anatomy/.

Pedley, M. (2013). Tilt Sensing Using a Three-Axis Accelerometer, Freescale Semiconductors.

PerceptionNeuron. "What is Motion Capture." from https://neuronmocap.com/content/mocap-101.

Quoc, D. D., et al. (2015). "Attitude Estimation Algorithms Using Low-Cost IMU." International Journal of Control and Automation: 117-119.

Roetenberg, D., et al. (2013). Xsens MVN: Full 6DOF Human Motion Tracking Using Miniature Inertial Sensors, Xsens Technologies.

Roetenberg, D., et al. (2005). "Compensation of Magnetic Disturbances Improves Inertial and Magnetic Sensing of Human Body Segment Orientation." IEEE Transactions on Neural Systems and Rehabilitation Engineering.

Scapello, S., et al. (2005). "In-use calibration of body-mounted gyroscopes for applications in gait analysis." Sensors and Actuators.

Shiau, J.-K., et al. (2012). "Noise Characteristics of MEMS Gyro's Null Drift and Temperature Compensation." Journal of Applied Science and Engineering.

Skog, I., et al. (2016). "Inertial Sensor Arrays, Maximum Likelihood, and Cram´er-Rao Bound." IEEE.

Slifka, L. D. (2004). An Accelerometer Based Approach to Measuring Displacement of a Vehicle Body. Department of Electrical and Computer Engineering, University of Michigan: 19-23.

Taunyazov, T., et al. (2016). A Novel Low-Cost 4-DOF Wireless Human Arm Motion Tracker. 6th IEEE RAS/EMBS International Conference on Biomedical Robotics and Biomechatronics (BioRob). UTown, Singapore.

Tedaldi, D., et al. (2013). "A Robust and Easy to Implement Method for IMU Calibration without External Equipments."

Titterton, D. and J. Weston (2004). Strapdown Inertial Technology. The Institution of Engineering and Technology.

Unsal, D. and K. Demirbas (2012). "Estimation of Deterministic ans Stochastic IMU Error Parameters." IEEE.

VectorNav. "Inertial Measurement Units." from http://www.vectornav.com/support/library/imu-and-ins.

Wikipedia. "Kinematic Chain." from https://en.wikipedia.org/wiki/Kinematic_chain.

Woodman, O. J. (2007). An introduction to inertial navigation, University of Cambridge.

Yuksel, Y. (2011). Design and Analysis of Inertial Navigation Systems with Skew Redundant Inertial Sensors, Schulich School of Engineering. Doctor of Philosophy.

Yuksel, Y., et al. (2010). "Error Modelling and Characterization of Environmental Effects for Low Cost Inertial MEMS Units
" IEEE: 605-611.

Zhang, W., et al. (2014). A Wireless Human Motio Monitoring System Based on Joint Angle Sensors and Smart Shoes. ASME Dynamic Systems and Control Conference

Zhao, Y. (2011). GPS/IMU Integrated System for Land Vehicle Navigation based on MEMS. Division of Geodesy and Geoinformatics, Royal Institute of Technology (KTH). Master of Science.

Zhi, R. (2016). A Drift Eliminated Attitude and Position Estimation Algorithm in 3D. Electrical Engineering, University of Vermont. Master of Science: 31-35.

APPENDIX A

MATHEMATICAL RESULTS

The following are some more discussion of the mathematics relevant to the thesis:

A1. Allan Variance

A2. Markov Process Model

A3. ACF calculation

A4. Normal Distribution

A1. Allan Variance

This method was developed to analyze the signal in time-series to characterize all the errors in a single graph. The following equation describes the process:

$$\sigma^2(nT) = \frac{1}{2(N-1)} \sum_{i=1}^{N-1} (y_{i+1} - y_i)^2$$

where r is the sampling time; x_i are the samples collected over a large time span; n is the size of the bin such that N is the total number of bins and y_i is the average of bin i. The curves are known as Allan deviation curves which is square root of Allan variance.

The idea is to glean sensor performance characteristics from data by averaging over a range of time spans. This averaging leads to removal of noise systematically from the sample data revealing effects of different noise sources on the sensor measurements. It gives us an idea of how well noise correction could be achieved under ideal conditions i.e. when there is no temperature variations or any external disturbances. In particular, it gives a measure of frequency stability of how good the noise correction could be. To make the interpretation

of the graphs easier, usually the Allan deviation curves are plotted as they are in the same units as the data collected making it easy for comparison.

A more detailed deconstruction of Allan deviation plot is:

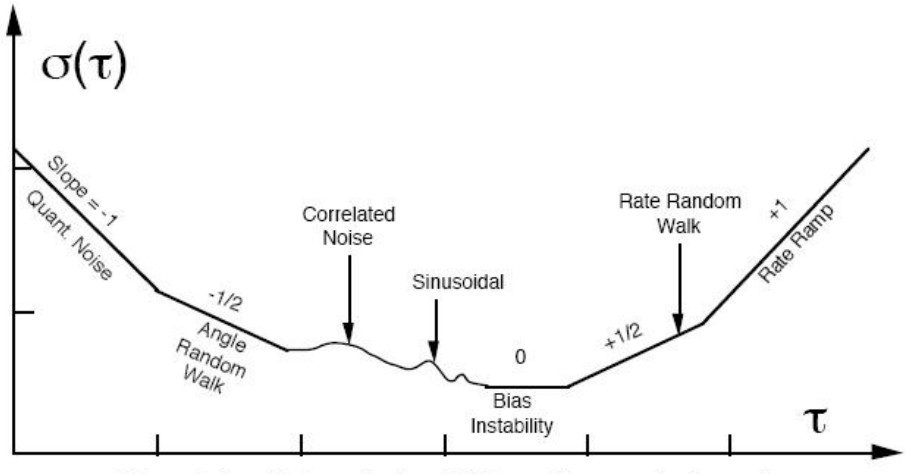

But for our analysis we have used only four points in the graph:

1. Point A: This is the starting point of the graph that represents standard deviation of noise for any one single measurement point. This gives us an idea of how noisy a single measurement could be; it is to be noted that this mentions the probability of noisy measurements not the certainty of it. The value tells you that 68% of the measurements will have the noise as stated in the y axis and the remainder will have noise greater than that. This is useful to compare if the noise will be a significant part of the measurements.
2. Slope A: This is the slope for the first part of the AV graph before the dip. This part is used to analyze the measurement noise, that depends on the influence of high frequency errors. This is as the averaging span in this region is still lot smaller, hence high frequency errors will dominate the calculations. These errors involve

quantization error and measurement errors. For the purpose of this thesis we have focused only on the measurement errors.

3. Point B: Represents the bias stability of the sensor. It gives you the lowest possible value of bias error generated in a sensor. This minimum point is go when theoretically the effect of high frequency errors and low frequency errors balance out to give the best possible value possible by the sensor. The lower the value, the better sensor it is. This is usually the main performance characteristic of a sensor, especially the gyroscopes.
4. Slope B: This is the slope for the second part of the AV graph, after the dip. This part is used to analyze the random walk errors, that depends on the influence of low frequency errors. This usually consists of the rate random walk and the rate ramp effect. For this thesis we only confirm the random nature of these noise sources.

In addition, to this these plots can be used to compare the effect of temperature on readings, which has not been explored here. We used the plot to identify the nature of the noise i.e. is the measurement noise is white or not. This is important so that the bias term in the error equation used is modelled as Gaussian White Noise. It has been further confirmed by the PSD and PDF analysis done further in the thesis.

A2. Markov Process Model

A random process is a time sequence representing the evolution of some system represented by a variable whose change is subject to a random variation. For discrete time, a stochastic process is a sequence of random variables, which is usually the case with digital

signals; with the only requirement that these random variables be part of the same space. A way to describe such a process is Markov Model. A stochastic process is called Markov if for every random variable n in a time series, we have:

$$P(x(t_n) \leq x_n = |x(t)\ for\ all\ t \leq t_n - 1$$

$$= P(x(t_n) \leq x_n | x(t_{n-1}))$$

This model is widely used for modelling sensor errors, not only because it is able to represent a large number of physical processes, but also because it has comparatively a straightforward mathematical equation. The continuous model for this process is depicted as follows:

$$\dot{x} = \frac{1}{T}x + w$$

where x is the random process with zero mean, T and noise w.

From this we can have the discrete form equation:

$$x_i = (1 - \mathcal{E}dt)x_{i-1} + w_i$$

where dt is the sampling time and w_i is the white noise with noise covariance given by:

$$\sigma_{w_i}^2 = \sigma_{x_i}^2(1 - e^{\frac{-2dt}{T}})$$

the value for T and $\sigma_{x_i}^2$ could be found from Allan variance plot. Then the parameters can be implemented in the Kalman filter.

A3. ACF calculation

Autocorrelation is the relationship of a signal in time series domain, i.e. it is the similarity between the observations as a function of the time lag between them. Autocorrelation function (ACF) tells us the time interval over which the correlation in the noise exists. Hence, they can be useful to determine the link between noise components of a signal.

ACF can be mathematically described as:

$$R(\tau) = \lim_{N \to inf} \frac{1}{N} \sum_{t=1}^{N} x(t)x(t+\tau)$$

where N is the total sample value and x(t) is digital signal. As this could be done over the full time series we can use ACF to look for patterns in the data.

ACF is an integral part of spectral analysis because it is related by the following equation:

$$S(f) = \int_{-inf}^{+inf} R(\tau) e^{-i2\Pi f \tau} d\tau$$

Where f is the spectral frequency, R(τ) is the autocorrelation function, and τ is the sampling time; LHS is the Fourier transform of the ACF. For a 1st order Markov process we have a known autocorrelation form given by:

$$R(T) = \sigma^2 e^{\frac{-T}{\tau}}$$

where σ is the variance of the markov process and τ time constant (sampling time). This highly simplifies the process of modelling the random noise inherent in sensors.

A4. Normal Distribution

Normal distribution also known as the Gaussian Distribution, is a kind of probability distribution used to describe a sample of real-valued variables. It is represented by the following equation:

$$f(x) = \frac{1}{\sqrt{2\Pi\sigma^2}} e^{\frac{-(x-\mu)^2}{2\sigma^2}}$$

where μ is the mean and σ^2 is variance of distribution x. The figure below depicts the graphical form of the distribution which distinctly appears as a 'bell'.

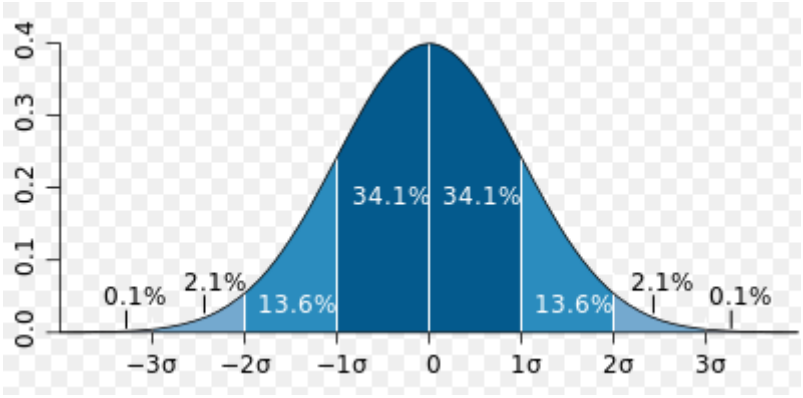

The distribution is designed such that the bulk of the sample are present in the region surrounding the mean within 1 standard deviation (68% of the area) and the total area of the curve is equal to 1. 95% of the area falls into 2 standard deviations and 99.7% fall within 3 standard deviations. The term standard deviation is a measure that is used to quantify the amount of variation of sample set.

Standard deviation can be approximately described with the following equation:

$$\sigma = \frac{1}{N}\sqrt{\sum_{i=1}^{N}(x_i - \mu)^2}$$

where σ is the standard deviation, N is the total number of samples; x_i is the ith sample and μ is the mean. Another useful term is variance, defined as the square of standard deviation:

$$var = \sigma^2$$

It is especially useful in mathematical manipulations as it is a positive number unlike the standard deviation (which is a square root). This term is the measure of dispersion of data with respect to mean of the sample. The unit of variance is square of standard deviation, hence for comparison purposes usually standard deviation is used.

The usefulness of normal distribution is due to the central limit theorem, which states that averages of random variables independently drawn from independent distributions converge in distribution to the normal, that is, become normally distributed when the number of random variables is sufficiently large. Hence it can easily describe a variety of physical phenomena accurately.

APPENDIX B

STATIC TEST PLOTS

The following are the results of the static test data:

B1. Allan Deviation

B2. Power Spectral Density

B3. Probability Density Function

B4. Drifting Bias

Static test was done for a period of 12 hours on yIMU in a thermal chamber. Care was taken so that the test unit was left untouched and no external impulses were given to it.

B1. Allan Deviation

The following section has the AV plots and the corresponding points of interest in the tables. The plots were generated in AlaVar 5.2. X axis unit: sec; Y axis unit (deg/sec) for gyroscopes and m/s_2 for accelerometers.

IMU-1 accelerometer X

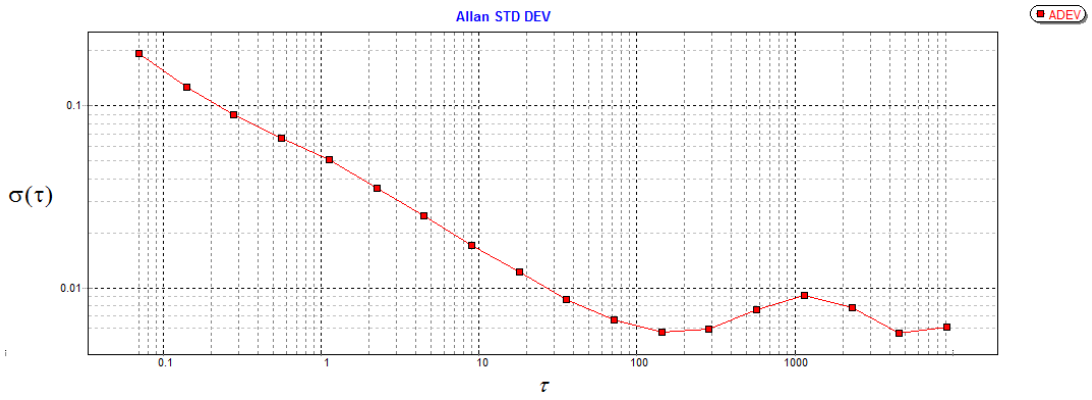

IMU-1 accelerometer Y

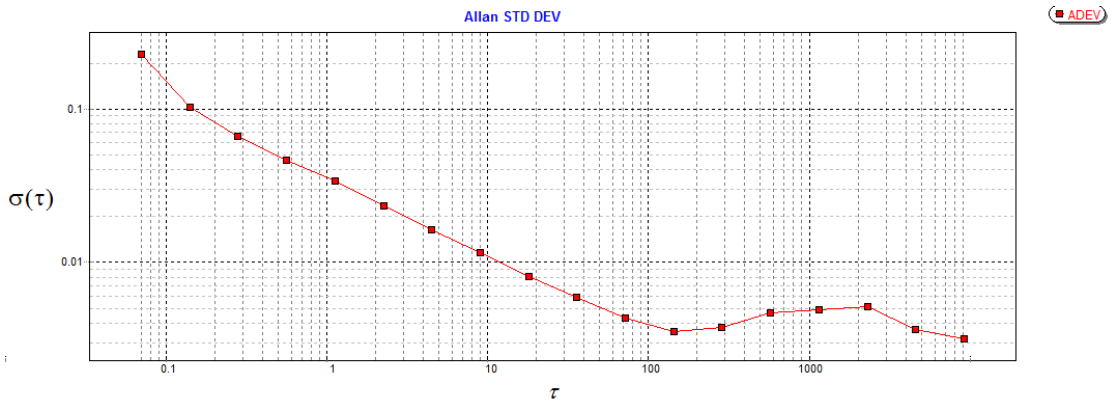

IMU-1 accelerometer Z

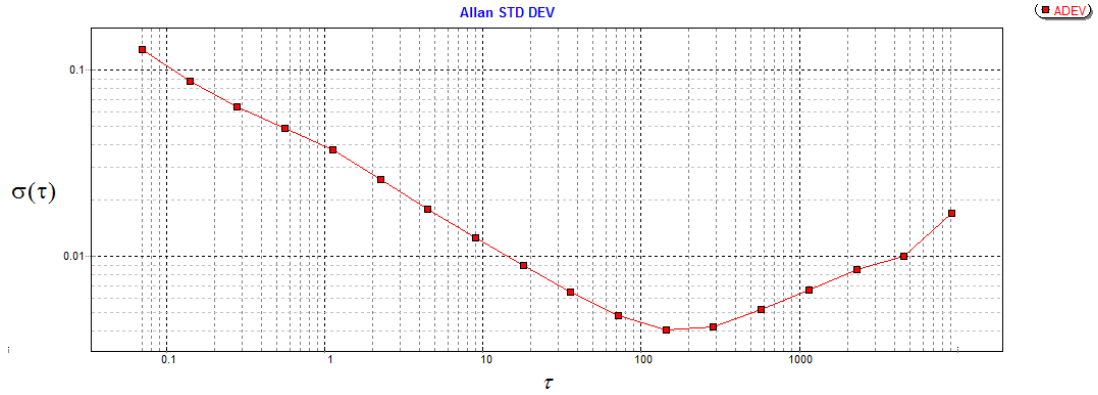

	POINT A (g)	SLOPE A	POINT B (g)	SLOPE B
IMU-1 X	0.07	-0.483754	0.0057	0.313607
IMU-1 Y	0.07	-0.519263	0.0035	0.149470
IMU-1 Z	0.07	-0.464424	0.00480	0.280849

IMU-1 gyroscope X

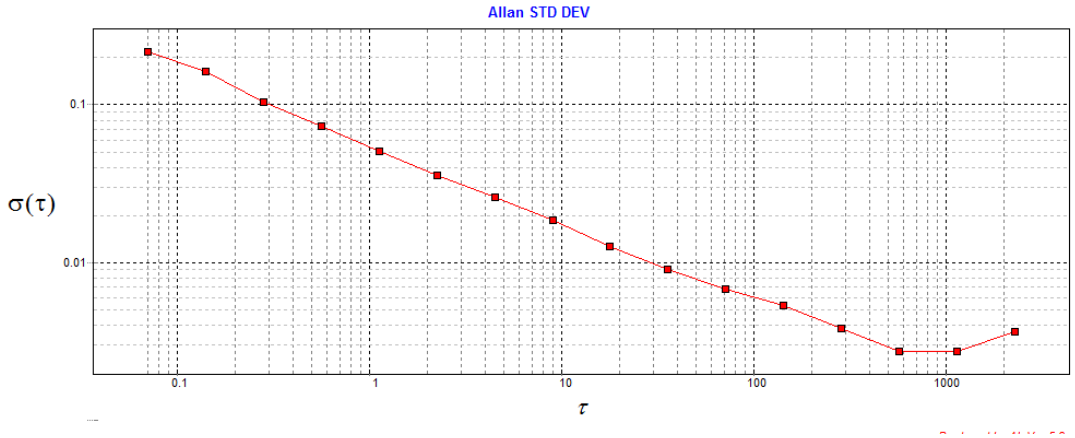

IMU-1 gyroscope Y

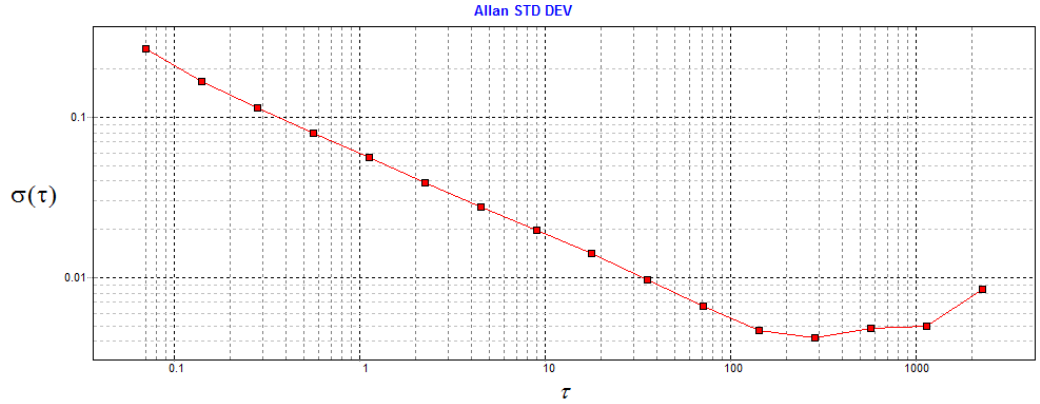

IMU-1 gyroscope Z

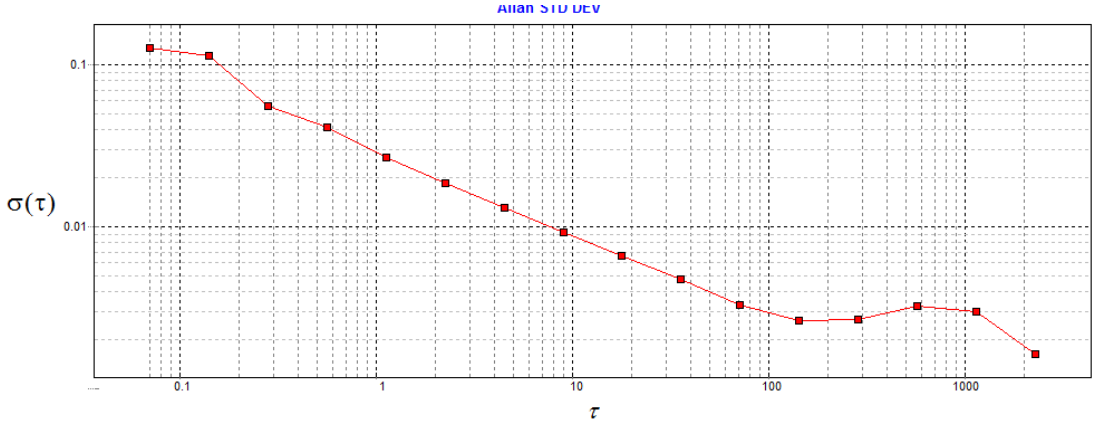

	POINT A (deg/s)	SLOPE A	POINT B (deg/s)	SLOPE B
IMU-1 X	0.07	-0.51176	0.0053	-0.40475
IMU-1 Y	0.07	-0.522333	0.0042	-0.40306
IMU-1 Z	0.07	-0.527713	0.0026	0.28838

yIMU accelerometer X

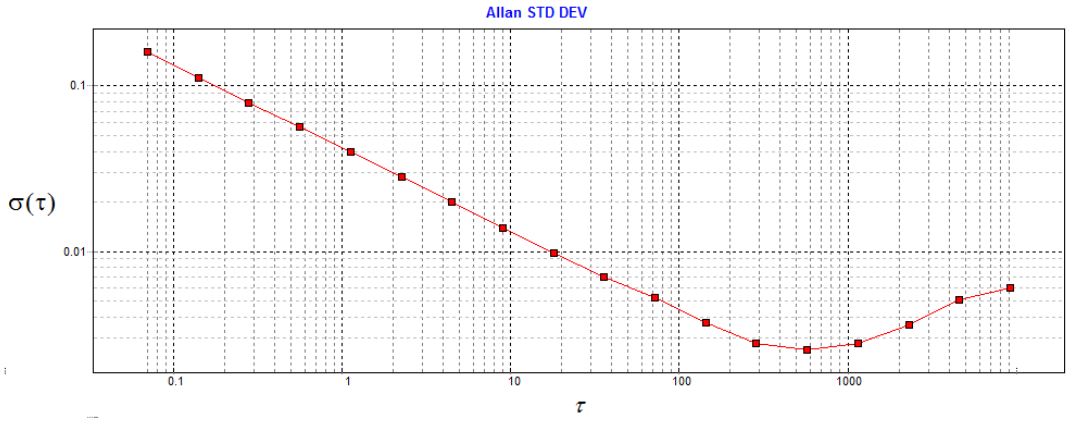

yIMU accelerometer Y

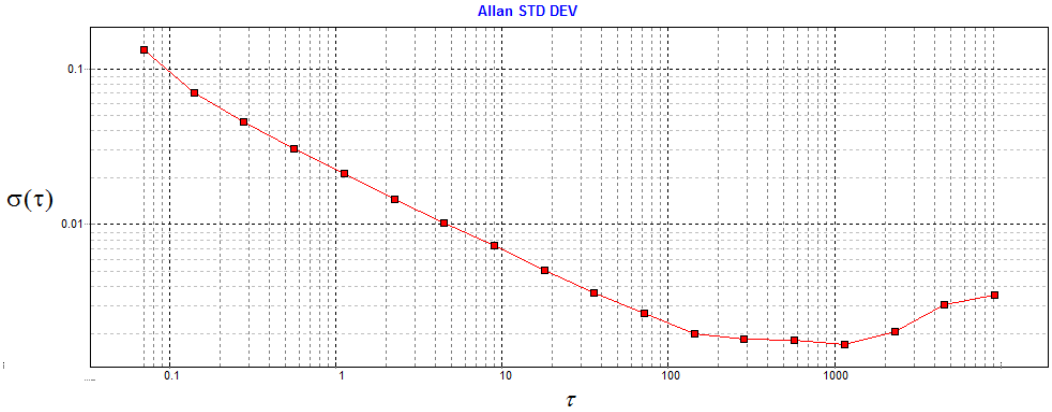

yIMU accelerometer Z

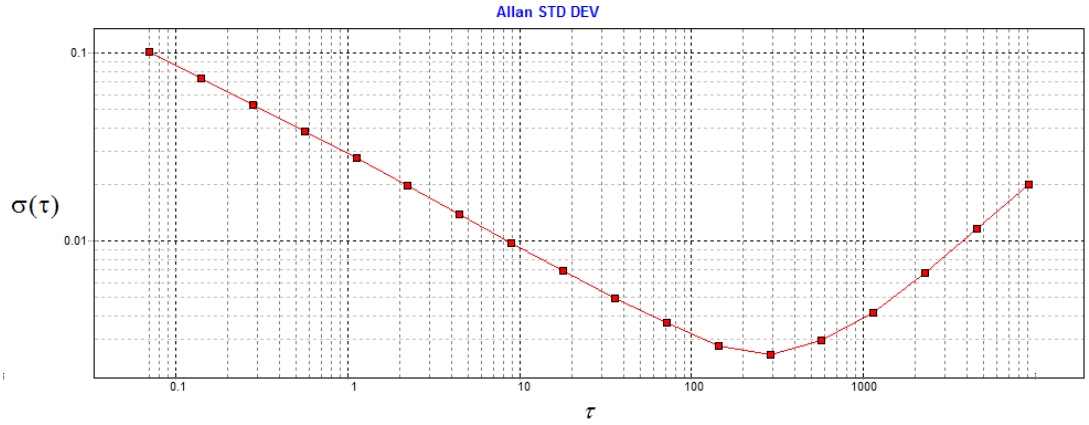

yIMU X	0.07	-0.490277	0.0026	0.383257
yIMU Y	0.07	-0.495157	0.0018	0.421459
yIMU Z	0.07	-0.485253	0.0025	0.564556

yIMU gyroscope X

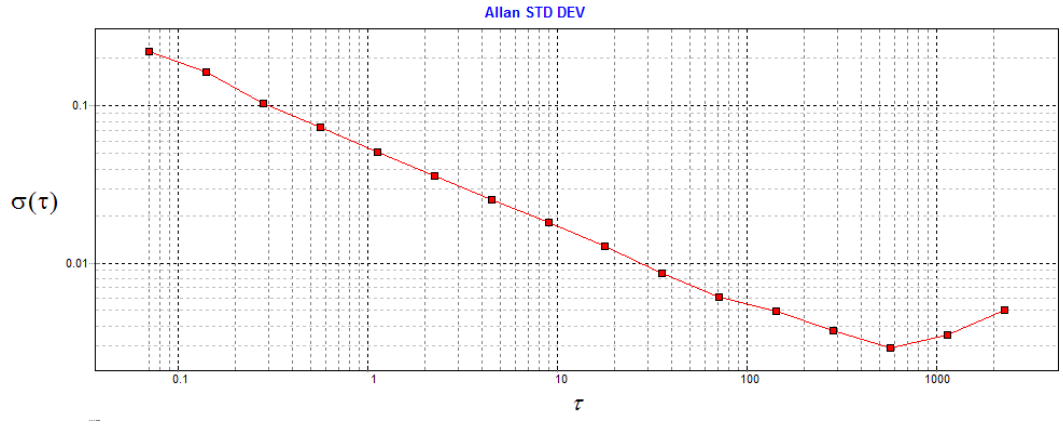

yIMU gyroscope Y

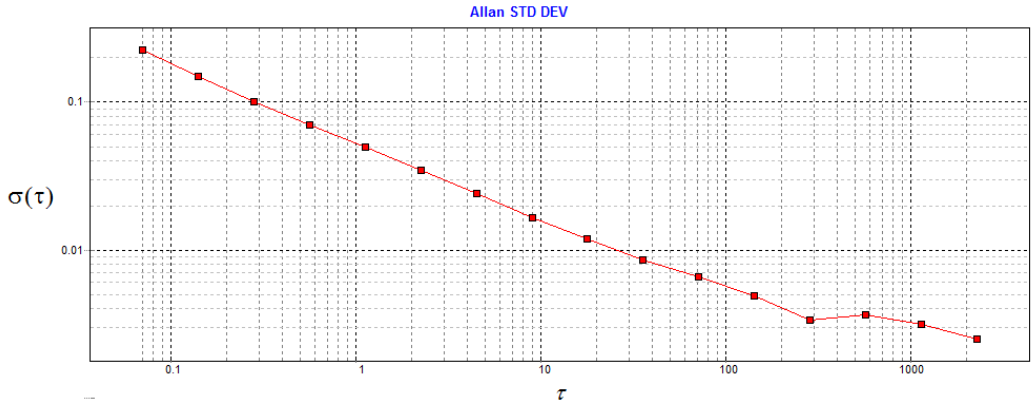

yIMU gyroscope Z

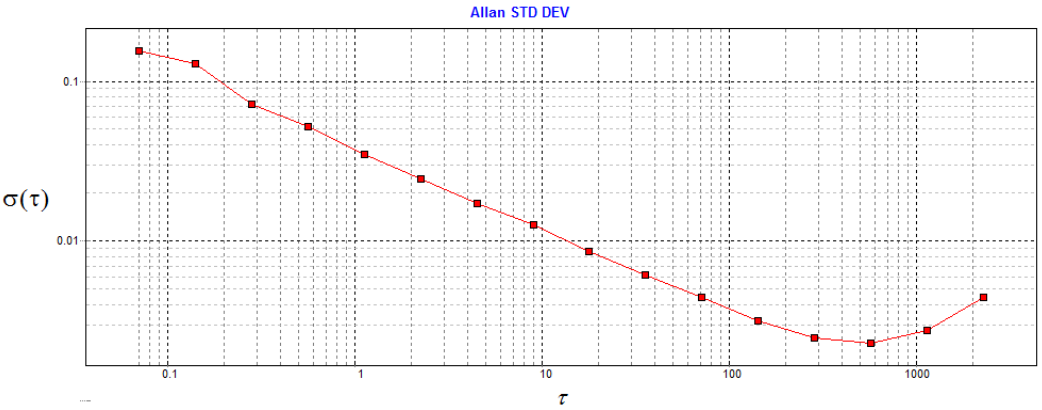

yIMU X	0.07	-0.519355	0.0029	0.484973
yIMU Y	0.07	-0.505054	0.0025	-
yIMU Z	0.07	-0.514046	0.0023	0.476239

B2. Power Spectral Density

The following are the PSD graphs generated in AlaVar 5.2. Unit of Y axis: $(m/s2)^2/Hz^2$ (accelerometers) and $(deg/sec)^2/Hz^2$.

IMU-1 accelerometer X

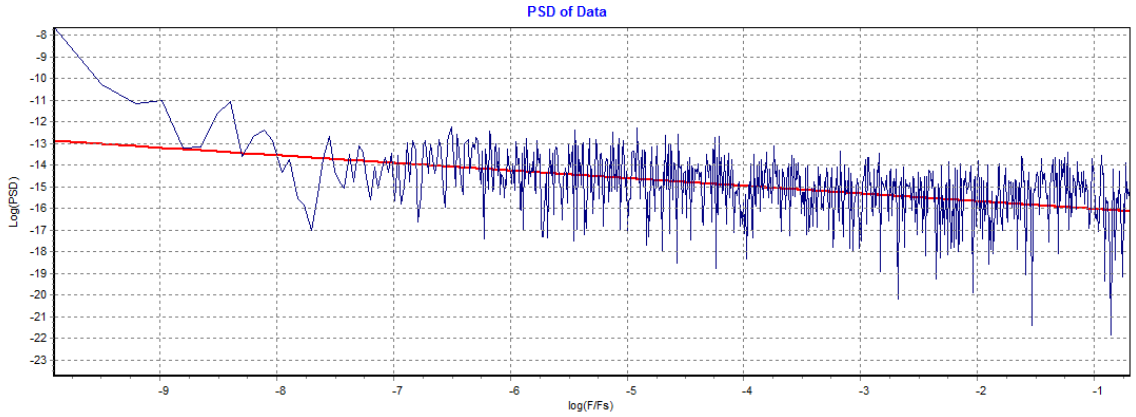

IMU-1 accelerometer Y

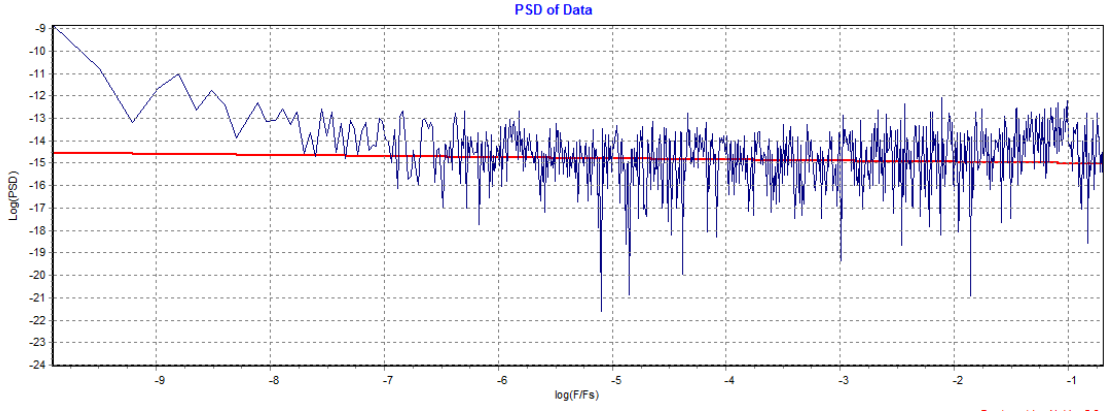

IMU-1 accelerometer Z

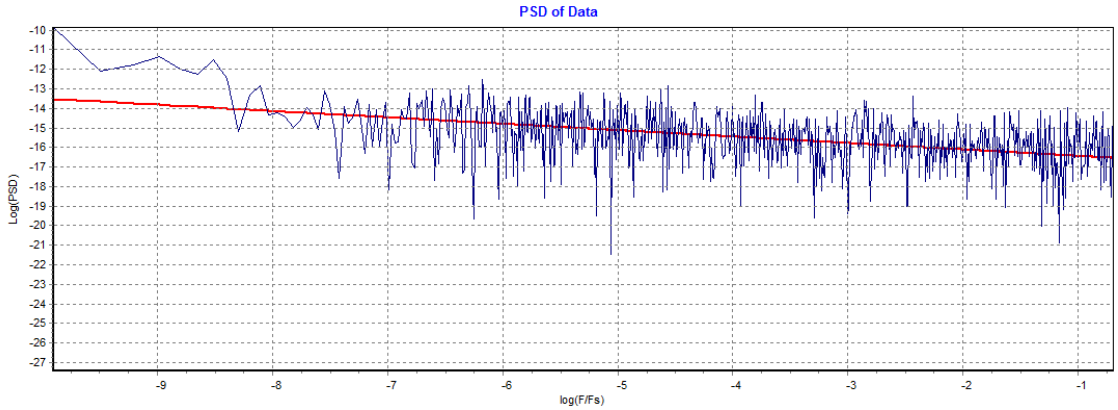

IMU-1 gyroscope X

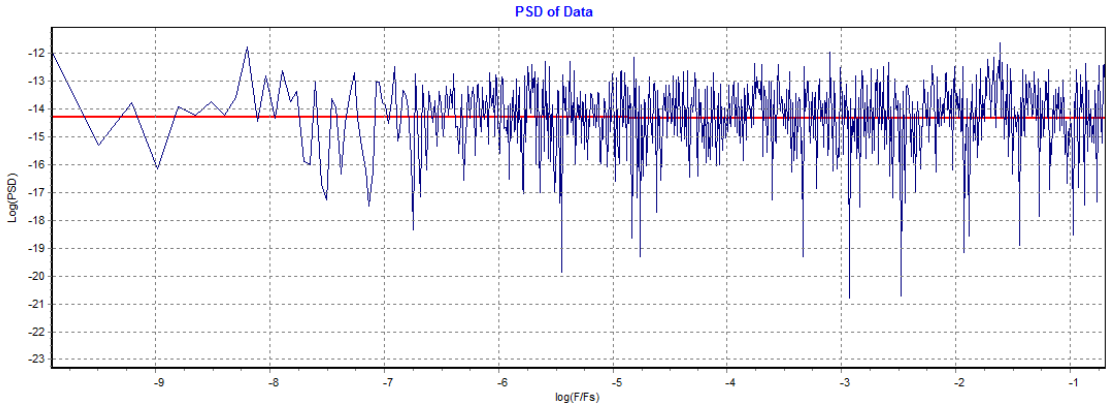

IMU-1 gyroscope Y

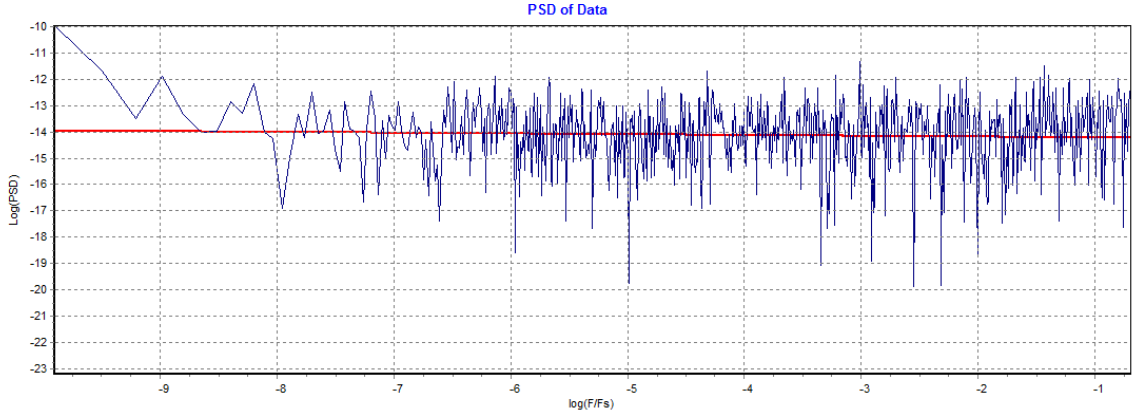

IMU-1 gyroscope Z

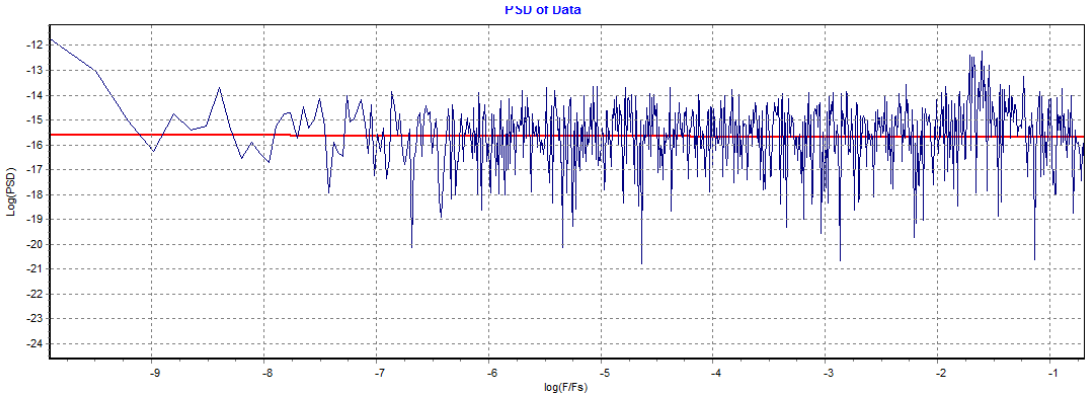

yIMU accelerometer X

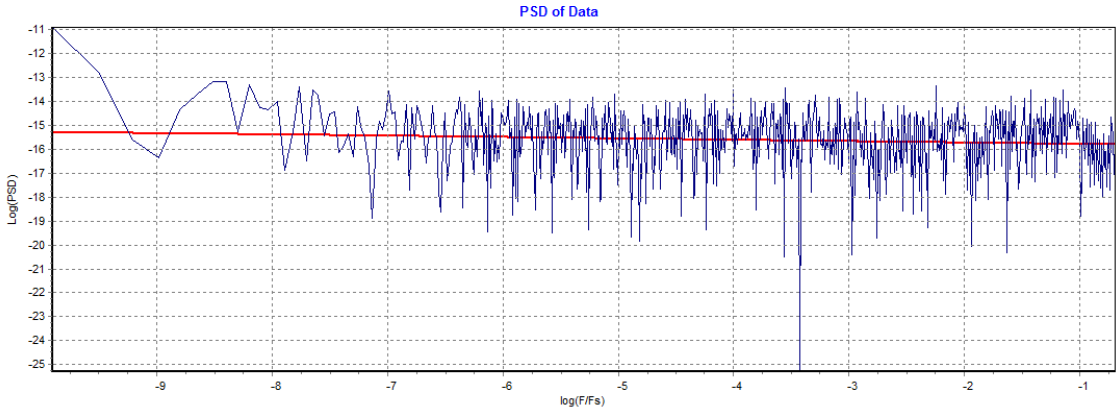

yIMU accelerometer Y

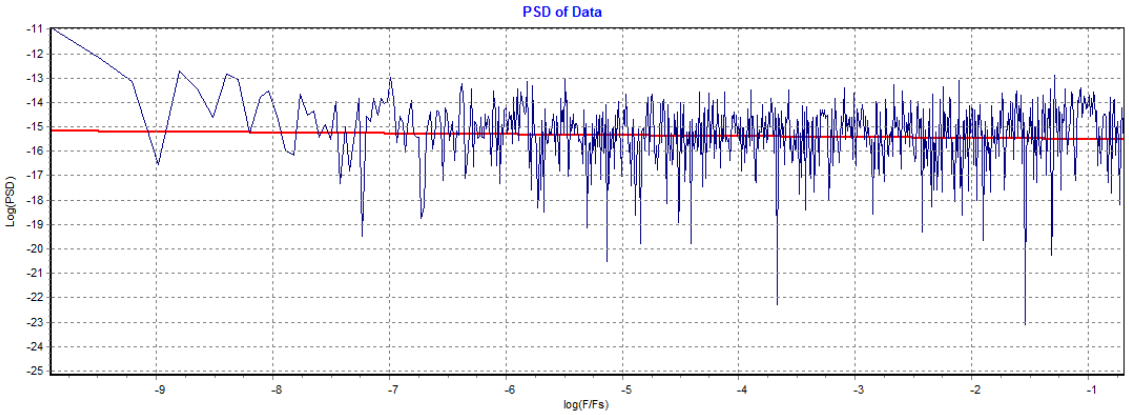

yIMU accelerometer Z

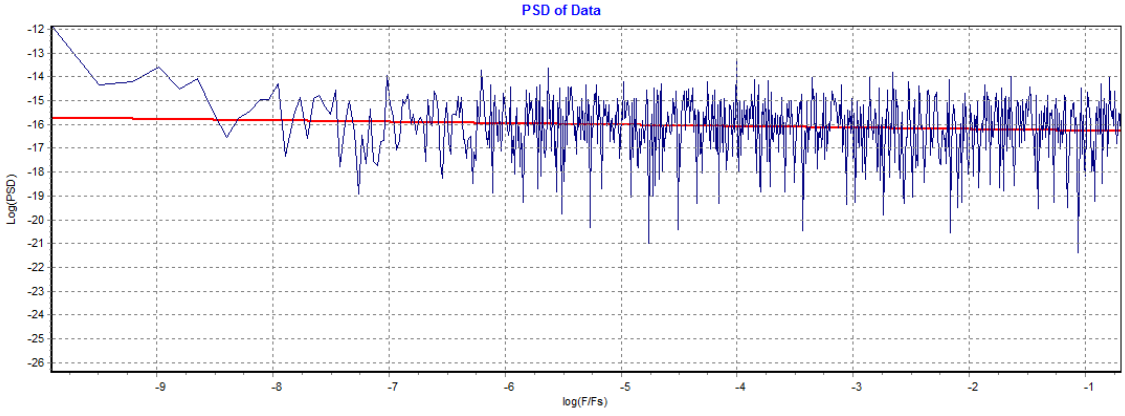

yIMU gyroscope X

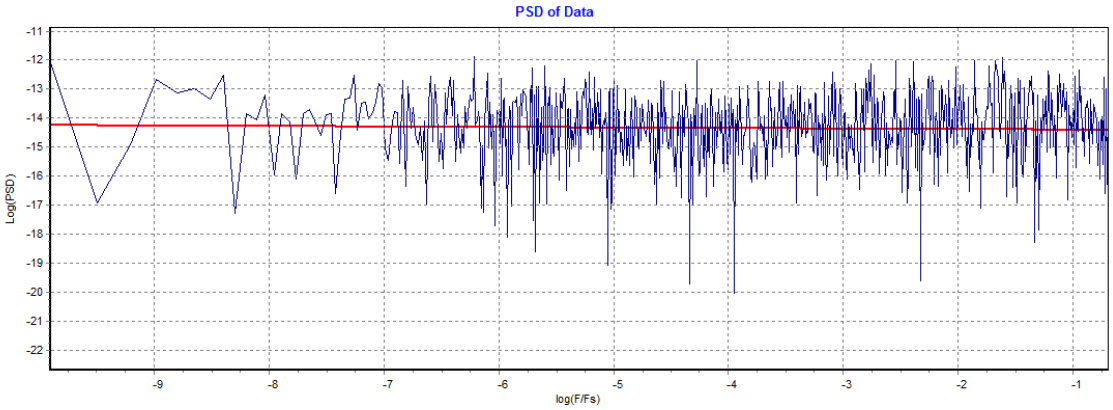

yIMU gyroscope Y

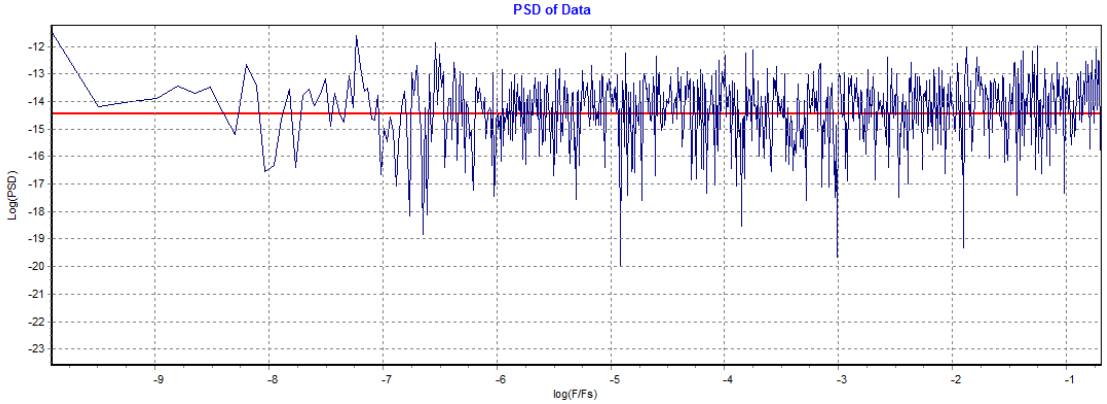

yIMU gyroscope Z

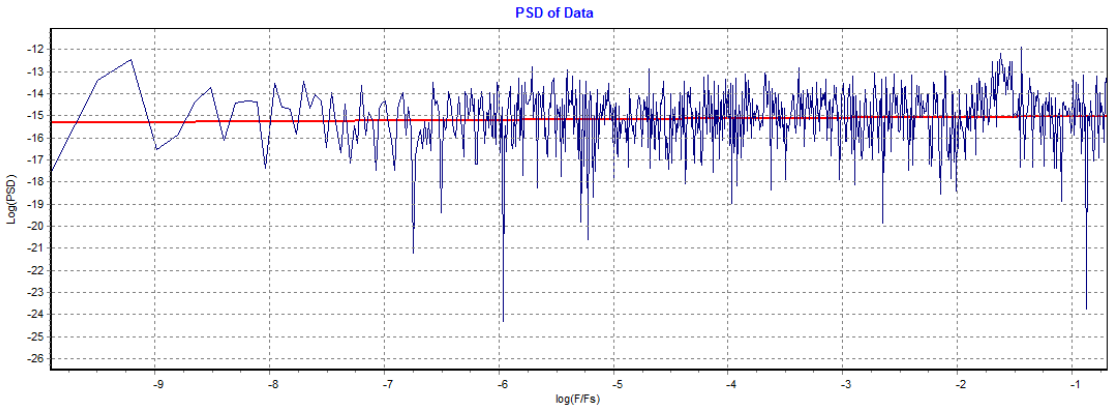

B3. Probability Density Function

The following graphs were generated in MATLAB.

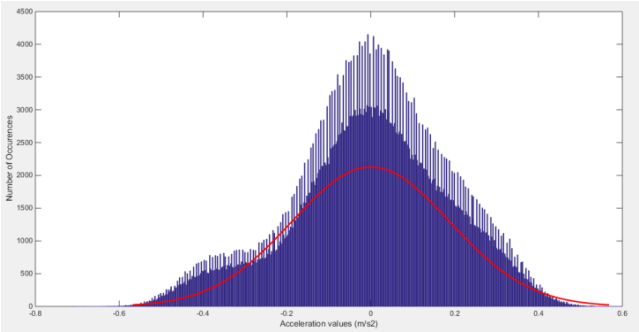

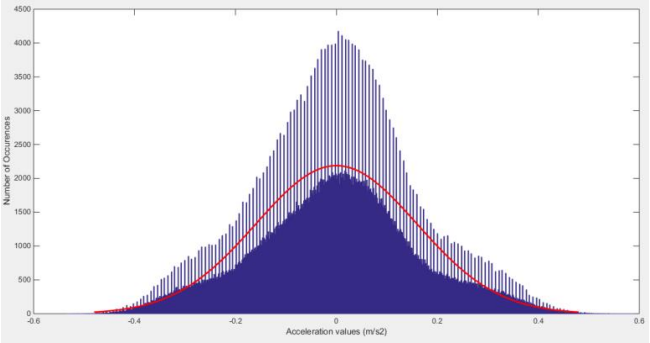

IMU-1 accelerometer X (above); yIMU accelerometer X (below)

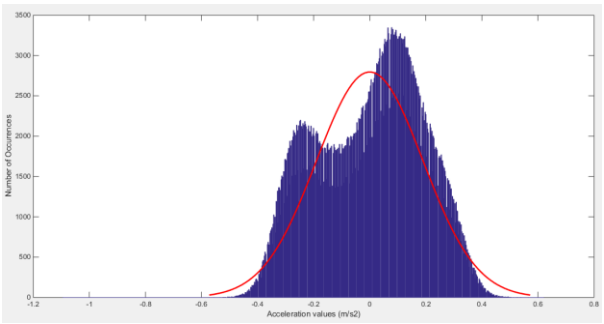

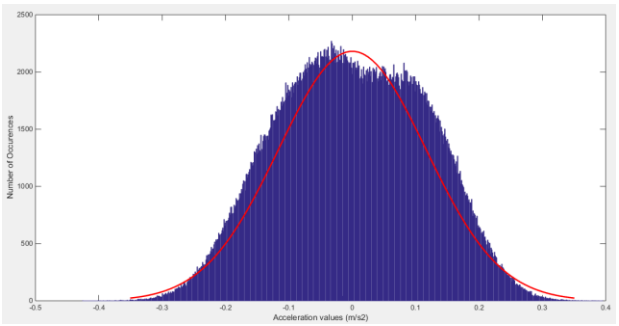

IMU-1 accelerometer Y (above); yIMU accelerometer Y (below)

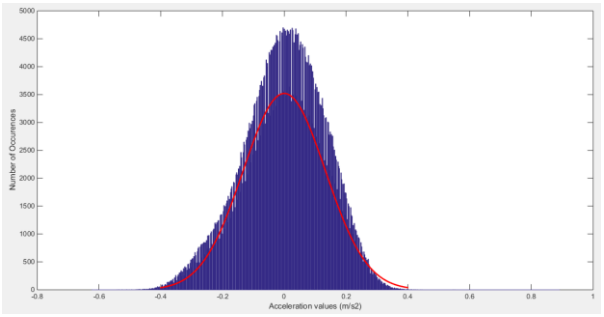

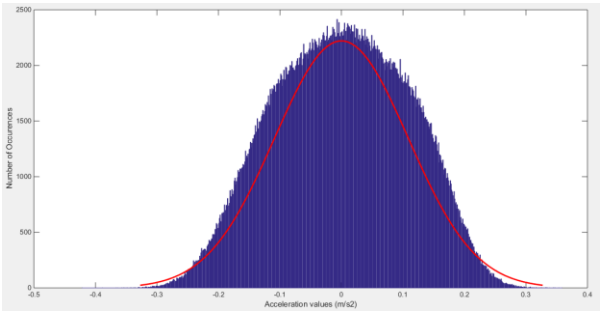

IMU-1 accelerometer Z (above); yIMU accelerometer Z (below)

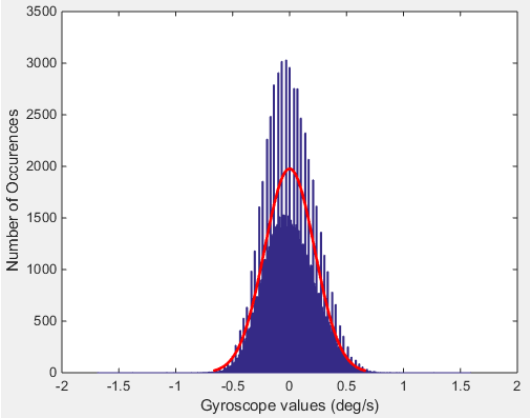

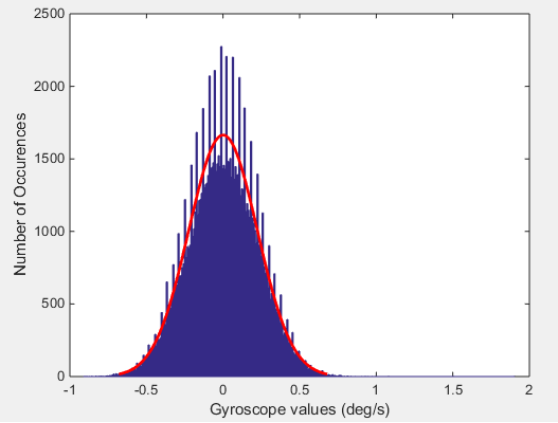

IMU-1 gyroscope Y

yIMU gyroscope Y

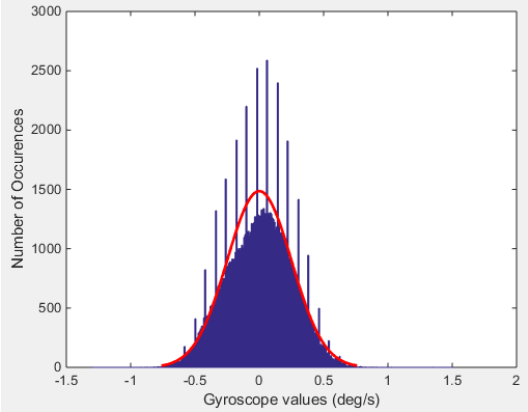

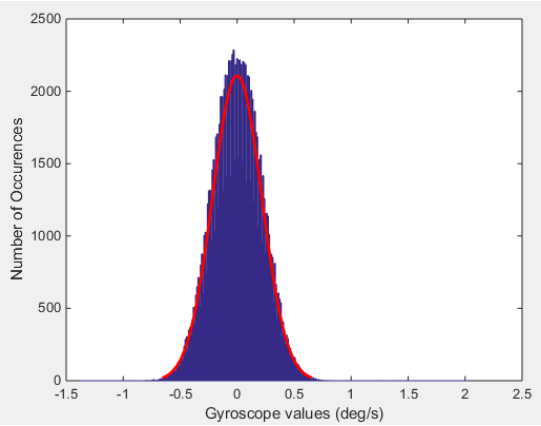

IMU-1 gyroscope Z

yIMU gyroscope Z

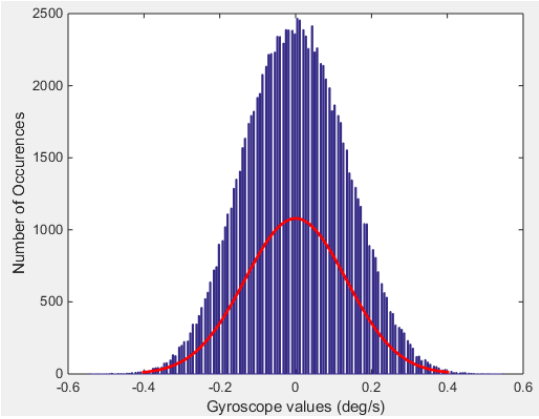

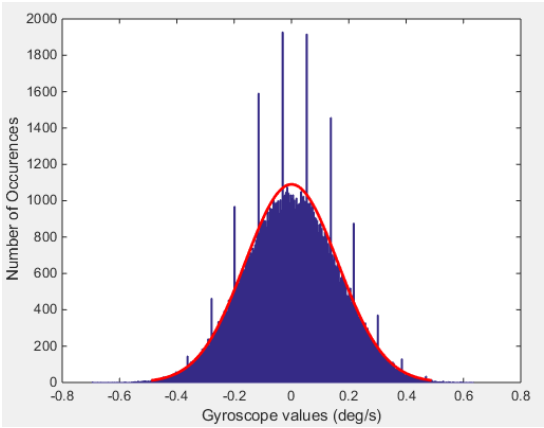

B4. Drifting Bias

The graphs show the impact of random walk on data. These were constructed by taking a moving average on the 12 hr static test.

IMU-1 accelerometer X

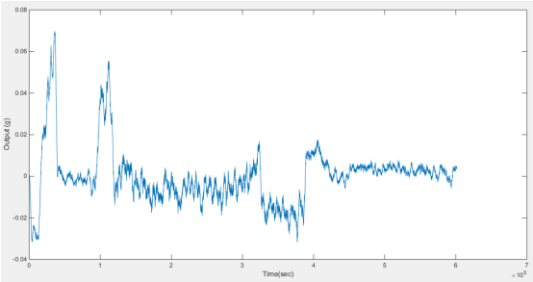

yIMU accelerometer X

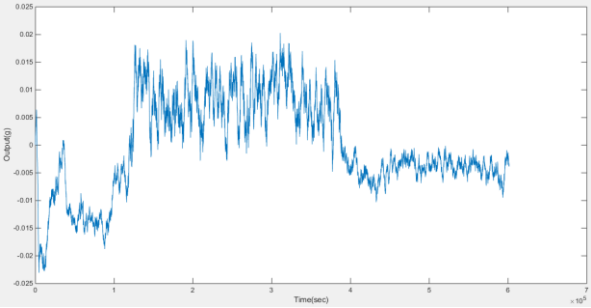

IMU-1 accelerometer Y

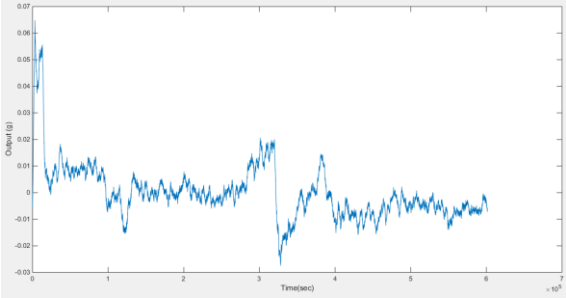

yIMU accelerometer Y

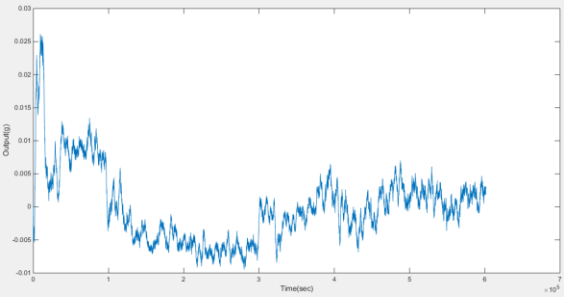

IMU-1 accelerometer Z

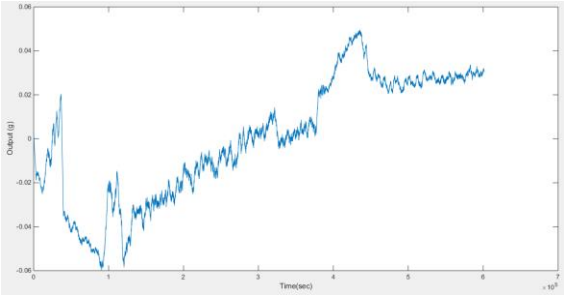

yIMU accelerometer Z